

University of Alberta

**Fabrication and testing of surface-enhanced Raman
spectroscopy substrates for the detection of biomolecules**

by

Robert Fraser Peters

A thesis submitted to the Faculty of Graduate Studies and Research
in partial fulfillment of the requirements for the degree of

Master of Science

in

Microsystems and Nanodevices

Department of Electrical and Computer Engineering

©Robert Fraser Peters

Spring 2014

Edmonton, Alberta

Permission is hereby granted to the University of Alberta Libraries to reproduce single copies of this thesis and to lend or sell such copies for private, scholarly or scientific research purposes only. Where the thesis is converted to, or otherwise made available in digital form, the University of Alberta will advise potential users of the thesis of these terms.

The author reserves all other publication and other rights in association with the copyright in the thesis and, except as herein before provided, neither the thesis nor any substantial portion thereof may be printed or otherwise reproduced in any material form whatsoever without the author's prior written permission.

To: Erica

Thank you for all your love, encouragement, and support.

Abstract

Biosensing involves the detection of analytes using biological elements as receptor agents for the specific binding of molecules to a surface. Surface-enhanced Raman spectroscopy (SERS), a surface-sensitive vibrational spectroscopy technique used to amplify Raman signals, provides unique advantages for biosensing. Unique Raman fingerprint spectra of targeted molecules allows for accurate identification of unknown samples. Inconsistencies in Raman signal enhancements, however, due to the irregularities of metallic features at the nanoscale, is a significant challenge with SERS. Nanofabrication technologies, including electron beam lithography (EBL) and nanoimprint lithography (NIL), provide resolution capabilities at the nanoscale.

In this work, nanofabrication methods were used to fabricate SERS substrates for the detection of analytes using various immobilization strategies. Control over signal intensity and detection of biological bonding, with analytes in aqueous solutions was demonstrated. Investigations and testing of various aspects in the fabrication processes allowed for significant control over features at nanoscale dimensions.

Acknowledgements

I would like to thank my supervisors, Dr. Maria Stepanova and Dr. Steven Dew, for their exceptional guidance and encouragement throughout this work. They helped instill in me an added excitement and love for learning in the unique fields of nanofabrication and biosensing. It has been a very rewarding and challenging experience, and I am grateful for the opportunity and support they have given me.

I would also like to thank the many people in my research group with whom I was able to work, including many individuals whose expertise gave a basis for this work to build on. In particular, I would like to thank Taras Fito, Luis Gutierrez-Rivera, Marium Japanwala, Mustafa Muhammad, and Mohammad Ali Mohammad, who all participated in this work directly in some way.

I am appreciative for the involvement I had with many people at the University of Alberta and at the National Institute of Nanotechnology (National Research Council Canada) involved with the metabolomics sensing work including Prasanna Bhomkar, Albert Cao, Lars Laurentius, Feng Wang and David Wishart, for their interactions and involvement with this unique program.

I would like to express my gratitude to the many staff in the different laboratories, for their training, support, and ideas, including all the nanoFab staff at the University of Alberta, Mike Xia from the NINT Organic/Inorganic Analytical Lab, Paul Concepcion and Kai Cui from the Electron Microscopy Labs at NINT, and Rob Indoe, Mike O'Toole and Tim Patrie from the NINT cleanroom.

Lastly, I would like to thank my parents and family for their love, support, and prayers. Their encouragement has been a wonderful motivation for me.

List of Figures

| | |
|---|----|
| Figure 2.1 – Model of a common sensor system incorporating aspects of specific targeting of analytes using biological elements as receptor components, transducer elements, signal amplification and electronics, and readout display of signal for interpretation from the end user..... | 4 |
| Figure 2.2 - Jablonski diagram showing the change in energies depending on the scattering type. (a, c) Stokes and anti-Stokes shifted Raman scattering, (b) Rayleigh scattering and (d) fluorescent emitted light [48]...... | 7 |
| Figure 2.3 - Offset Raman spectra of dopamine powder from own work with 532 nm (black) and 780 nm (red) excitation laser. The shorter wavelengths show increased details but with a trade-off of increased fluorescence for some samples, such as DNA and some proteins. All detected spectra throughout this thesis display the Stokes-shifted spectra. | 8 |
| Figure. 2.4 - Some common SERS platforms for signal enhancement. (a) Roughened silver surface, (b) metallic spheres in solution [85], (c) nanosphere particle arrays [86], and (d) EBL fabricated periodic metal dot array. Images (b, c) published with permission. Images (a, c) obtained from experimental work..... | 13 |
| Figure 2.5 - Illustration of a laser beam focused on nano-patterned metallic dots with immobilized protein. The green arrows represent the scattered Raman light..... | 13 |
| Figure 2.6 - EBL Process for positive (left) and negative (right) toned resists involving: (a) spin coating of resists; (b) electron beam exposure of patterned regions; and (c) development of resist to remove soluble regions..... | 16 |
| Figure 2.7 - CAD illustration of a 100 nm pitch dose grating with scale numbers and colors corresponding to different dose values (dose factors) of individual dots composing the array. Experimental results showed that the dot size of patterned features increased with higher dose factors, which varied depending on the fabrication process. | 17 |
| Figure 2.8 - Cross-section illustration of positive tone electron-beam resist during development. Gel formation occurs from interaction between the solvent and resist. Cooler temperatures during development prevent the gel region, which contains partially exposed polymer from being dissolved quickly, allowing increased resolution for electron-beam lithography. (Reproduced from [97]). | 17 |
| Figure 2.9 - 50 nm pitch gold dots fabricated on a fused silica substrates using a PMMA lift-off process and an anti-charging layer of aquaSAVE conductive polymer. Image obtained with permission from [74]...... | 18 |
| Figure 2.10 - Schematic of EBL fabricated substrates including simulation stage where the EBL Simulator was used to compare with experimental results for silicon and fused silica substrates investigating the effects of the conductive layers for different doses of 100 nm pitch holes in PMMA. Lift-off processing was done on fused silica substrates with aquaSAVE conductive polymer to obtain dot pitches ranging from 40 nm to 200 nm with varying gap sizes [74]...... | 19 |

| | |
|---|----|
| Figure 2.11 - Image of a fused silica sample used as a substrate material for fabricating SERS devices. Fabrication on fused silica substrates was done with both EBL and NIL as fused silica had excellent optical and electrical properties helpful for SERS. | 20 |
| Figure 2.12 - Process steps for the three basic nanoimprint lithography (NIL) techniques: (a) thermal nanoimprint lithography, (b) soft lithography (microcontact printing), and (c) ultraviolet (UV) (step and flash) nanoimprint lithography (S-FIL) (Reproduced with permission [104]) | 21 |
| Figure 3.1 - Thermo Scientific Nicolet Almega XR Micro and Macro Raman Analysis System used for Raman spectroscopy of signals from SERS substrates and other spectra. The system has both 532 and 780 nm excitation sources with CCD cooling to -100 °C for low noise detection of Raman signals (www.thermoscientific.com). | 24 |
| Figure 3.2 - Samples were kept in a buffer solution during Raman imaging, as many biological analytes require specific conditions to prevent degradation. The samples were sealed in the buffer solution with a transparent microscope cover. | 25 |
| Figure 3.3 – Image of the column and detector components of the Raith 150 ^{TWO} electron beam lithography system which is used at the University of Alberta (www.raith.com). | 25 |
| Figure 3.4 - Top view (left) and 3D (right) visualization of the yield of scission for PMMA 950K using the NINT Electron Beam Lithography Simulator. The software is able to predict both exposure and development patterns in PMMA and ZEP resists. The units displayed are in Angstroms. | 26 |
| Figure 3.5 - Nanonex NX-2500 Nanoimprint system used for nanoimprinting. The tool allows for both thermal and UV imprinting (www.nanonex.com). | 27 |
| Figure 3.6 - Oxford Instruments PlasmaLab System used for etching of NIL molds and NIL substrates (www.oxford-instruments.com) | 28 |
| Figure 3.7- Cee 200X spinner (left) and hotplate (right) from Brewer Science used to spin and bake substrates for EBL and NIL (www.brewerscience.com). | 28 |
| Figure 3.8 - Filmetrics measurement system used for measuring thin film thicknesses on various substrates. Thickness measurements were obtained with resolution and accuracy less than one nanometer for many resists thicknesses measured. | 29 |
| Figure 3.9 - An example of the measurement display interface of the filmetrics thin film measurement system. Accuracy of the measurements was within a few nanometers. ... | 30 |
| Figure 3.10 - Kurt J. Lesker water-cooled, bell jar, electron-beam evaporation system with cryo-pumped chamber and four-pocket crucible holder. | 31 |
| Figure 3.11 - Avogadro: an open-source molecular builder and visualization tool was used to build and visualize different molecules and proteins. This image contains a simple wireframe and cartoon view of the recombinant B domain of staphylococcal protein A obtained from the RCSB Protein Data Bank (1BDD) [127]. Modified protein A was used for benchmark testing for SERS bio-detection. | 33 |

Figure 4.1 - Arrays of 100 nm pitch dots in PMMA on fused silica substrates developed using an IPA:H₂O (7:3) development process. One-hundred nm pitch dots or pits in developed resist over a large area can be seen in: (a) an optical image of a substrate developed at 12 °C; and (b) a SEM image of a sample developed at room temperature at higher magnification showing collapse at high dose factors close to 50 in the central regions due to a higher effective dose. Values on scale bar correspond to a dose factor with a base dose of 0.6 fC/dot, which gradually increase to the right. Experimental results found an approximate 5 nm average dot size variation for every 10 µm distance for cold development. 38

Figure 4.2 - SEM images of PMMA honeycombs as observed (left) and predicted (right) on a silicon substrate with (a) 30 nm PMMA structure widths using a 150 µC/cm² area dose and (b) 22 nm structure widths using a 170 µC/cm² area dose with 90 nm thick PMMA resist and developed using a cool, +12 °C IPA:H₂O (7:3) developer for 60 s... 40

Figure 4.3 - 100 nm pitch developed holes in PMMA resist on a silicon substrate using a co-solvent IPA:H₂O (7:3) developer for 20 s at room temperature with a 12 fC/dot dose with a 30 keV accelerating voltage [74, 101]. 42

Figure 4.4 – (a) Simulated three dimensional and (b) cross-section development profiles of 100 nm pitch dots in PMMA on a fused silica substrate with aquaSAVE conductive polymer and a 12 fC/dot dose using a 30 keV accelerating voltage with 20 s development in IPA:H₂O (7:3) at room temperature. Measurement of the minimum gap width of features was done using the simulated cross sections. Here, the remaining resist is in red and regions with clearance are shown in blue. The anti-charging layer and substrate are not shown in the simulation. Distances are (a) 3000 Angstroms total width in the X and Y axis and 1000 Angstrom for the Z-axis and (b) 400 Angstrom arrow width. 43

Figure 4.5 - SEM images of 100 nm pitch dots in PMMA with different anti-charging schemes with fused silica samples on the left and silicon samples shown on the right. The left column (a-c) shows fused silica substrates with (a) 70 nm of aquaSAVE conductive polymer, (b) 10 nm of evaporated aluminum conductive layer, and (c) 30 nm of evaporated aluminum conductive layer (stigmation of dots was during imaging and not part of the original pattern). The right column (d-f) shows silicon substrates with (d) 70 nm of aquaSAVE conductive polymer, (e) 10 nm of evaporated aluminum conductive layer, and (f) no conductive layer. All samples were exposed at 30 keV with a 7.5 fC/dot exposure dose and developed for 20 s in IPA:H₂O (7:3) at room temperature with 90-100 nm thick PMMA. 44

Figure 4.6 – SEM image of 100 nm pitch dots in ~100 nm thick PMMA using a 7.5 fC/dot exposure dose on a silicon substrate with 30 nm of aluminum used for measurement of the effects of using the thick layer. Resist roughness and poor adhesion were seen for all silicon samples exposed to the aluminum etchant for longer than 3 min, with and without aluminum. 45

Figure 4.7 - Comparison between simulation and experimental 100 nm pitch dots in PMMA on fused silica and silicon samples with aquaSAVE conductive polymer and silicon with no conductive layers using a 30 keV accelerating voltage with 20 s development in IPA:H₂O (7:3) at room temperature. Standard deviation was within 3 nm for each sample. 46

| | |
|--|----|
| Figure 4.8 - Comparison of dot sizes for 100 nm pitch dot arrays in 100 nm thick PMMA for a range of exposure doses on fused silica, using a 30 keV accelerating voltage and 20 s development in IPA:H ₂ O (7:3). Lines correspond to simulated results and symbols correspond to experimental data. Standard deviation was within 3 nm for each sample..... | 47 |
| Figure 4.9 - SEM image 100 nm pitch dots in PMMA resist on a fused silica substrate using a 10 nm evaporated aluminum film as a conductive layer exposed at 30 keV with a 6 fC/dot dose and developed for 20 s in IPA:H ₂ O (7:3) at room temperature. | 48 |
| Figure 4.10 - Comparison of dot sizes for 100 nm pitch dot arrays in 100 nm thick PMMA for a range of exposure doses on silicon, using a 30 keV accelerating voltage and 100 nm pitch dots with a 20 s development in IPA:H ₂ O (7:3). Lines correspond to simulated results and symbols correspond to experimental data. Results marked with an x represent a silicon sample with no aluminum layer and developed after being placed in the aluminum etchant MF CD-26 for 3 min. Standard deviation was within 3 nm for each sample..... | 49 |
| Figure 4.11 – SEM images demonstrating the variation in grain size and charge build up between (a) 20 nm of aluminum on PMMA on a fused silica substrate and (b) 30 nm of aluminum on PMMA on a fused silica substrate. 20 nm aluminum films experienced significant charge-build up when imaged at 10 keV and with a 5.9 mm working distance. | 50 |
| Figure 4.12 – Cross section image of 100 nm thick PMMA on a silicon substrate with a 30 nm top coating of aluminum showing a continuous film. Charge-build up during SEM imaging of 30 nm films whereas 20 nm and thinner aluminum films on fused silica substrates did experience charging. | 50 |
| Figure 4.13 - Overlap of predicted and simulated dot diameters using the EBL Simulator tool for prediction of dot diameters and gaps needed for subsequent evaporation and lift-off. This sample was with a fused silica substrate and aquaSAVE conductive polymer at 30 keV accelerating voltage with 100 nm pitch..... | 51 |
| Figure 4.14 - Nanoimprint lithography process flow for mold fabrication. Silicon substrates underwent a thermal oxidation to provide the pillar material as silicon dioxide is known to be less brittle than silicon, allowing for improved lifetime after multiple nanoimprints. | 54 |
| Figure 4.15 – SEM images of thermally grown silicon dioxide pillars on a base silicon substrate with 10 nm of chrome for (a) 50 nm pitch and (b) 100 nm pitch arrays. Etch time for these samples was 20 s using a C ₄ F ₈ /helium . Images were taken at a 30° angle. | 55 |
| Figure 4.16 – SEM image of 100 nm pitch thermally grown silicon dioxide pillars with 10 nm chromium caps of a NIL mold and narrow gaps. Etching parameters allowed for improved feature dimensions and more vertical sides to assist in lift-off. Images were taken at a 30° angle. | 56 |

| | |
|---|----|
| Figure 4.17 - Self-assembled monolayer of trichloro(1H,1H,2H,2H-perfluorooctyl)silane (perfluorodecyltrichlorosilane) which binds to the native oxide layer on silicon. Tests also confirmed that the silane bound the surface of the nanoimprint resist (see Figures 4.18 and 4.19). | 57 |
| Figure 4.18 - Comparison of contact angle measurements on silicon mold material (a) before, and (b) after application of SAM anti-adhesion layer of trichloro (1H,1H,2H,2H-perfluorooctyl)-silane..... | 58 |
| Figure 4.19 - Comparison of contact angle measurements on NXR-1025 NIL resist (a) before and (b) after application of SAM anti-adhesion layer of trichloro (1H,1H,2H,2H-perfluorooctyl)-silane..... | 58 |
| Figure 4.20 - Placement of mold on top of sample after a nanoimprint run. The sample and mold are placed between two sheets of transparent film, which allows a uniform pressure. Temperature was measured on the sample using a thermocouple as seen in the center of the image. After the imprint, a small bubble around the substrates as well in other regions between the films remained. | 60 |
| Figure 4.21 - (Flipped) optical image of nanoimprinted 50 nm pitch regions on a transparent fused silica substrate. The darker shaded boxes correspond to larger dot diameters transferred from the master mold. The values here are the dose factors used which were multiplied by 0.6 fC/dot. | 61 |
| Figure 4.22 - Thermal nanoimprint process used for fabrication of SERS substrates including (1) sample alignment; (2) thermal imprinting and separation process; (3) oxygen plasma; (4) metal evaporation (e.g. copper, gold, silver); and (5) resist lift-off. | 62 |
| Figure 4.23 - 50 nm pitch dots imprinted in ~85 nm thick NXR-1025 thermal nanoimprint resist using a 1 cm x 1 cm mold and fused silica substrate after an etch process. Minimum gap size between dots was approximately 20 nm. | 63 |
| Figure 4.24 - 100 nm pitch dots imprinted in ~85 nm thick NXR-1025 thermal nanoimprint resist using a 1 cm x 1 cm mold and fused silica substrate with ~20 nm diameter features..... | 64 |
| Figure 4.25 - 100 nm pitch dots imprinted in ~85 nm thick NXR-1025 thermal nanoimprint resist using a 1 cm x 1 cm mold and fused silica substrate with an ~20 nm gap distance between opened holes. An etch process was done on this sample to gain clearance in opened dots for subsequent lift-off. | 64 |
| Figure 4.26 – SEM image showing insufficient clearance after the etching process resulted in partial yield of dots during lift-off. Here, gold was evaporated on a fused silica substrate using electron beam evaporation to a metal thickness of ~10 nm. | 65 |
| Figure 4.27 – EBL fabricated 100 nm pitch gold dots on a fused silica substrate after lift-off. The nucleation of the gold layer can be seen with the individual dots..... | 67 |

Figure 4.28 – SEM image of 200 nm pitch 10 nm thick gold periodic dot array fabricated after a NIL process and subsequent lift-off to form metal uniform dot arrays. Lift-off using was done by soaking the samples in a heated N-Methyl-2-pyrrolidone (NMP) solvent prior to sonicating the samples in the solvent. It was found that NMP offered improved results compared to acetone for lift-off for NIL fabricated SERS substrates..... 67

Figure 4.29 – SEM image of 100 nm pitch 10 nm thick copper dots on a fused silica substrate fabricated using NIL and a lift-off process. Lift-off was done by soaking the samples in a heated NMP solvent prior to sonicating the samples in the solvent..... 68

Figure 4.30 – Array of 100 nm pitch copper dots on a fused silica substrate fabricated using NIL with lift-off done using a heated NMP solvent..... 68

Figure 4.31 – EBL fabricated gold honeycomb shaped nanostructures on a fused silica substrate used for SERS. Gold nucleation from deposition can be seen in the structures from the evaporation process. PMMA development was done using a room temperature IPA:H₂O (7:3) development process. Image was provided by Luis Gutierrez-Rivera. ..69

Figure 5.1 - 3D model of Protein A from solution NMR spectroscopy, obtained from the RCSB Protein Data Bank (1BDD) [129]. The protein was rendered using the Avogadro software..... 71

Figure 5.2 – SEM image of 100 nm pitch silver dots on a fused silica substrate with an average 15 nm gap distance between dots. This sample and others were used for obtaining SERS spectra of immobilized protein A. 72

Figure 5.3 - Comparison of the signal intensity of protein A using thiol mediated binding on silver and gold pads. Immobilization of the thiolated protein A on pure silver films gave the strongest SERS signals compared to other films. For these samples, a 1.2 mW, 532 nm excitation wavelength was used for the Raman sampling for 3 s at all wavelengths. Spectra are offset vertically for easier comparison. 74

Figure 5.4 - Laser induced damage to a 10 nm silver film after Raman imaging at full laser power. Reduction of the laser power to 1.2mW was found to allow sufficient signal enhancement without damage to the underlying material. 75

Figure 5.5 - Optical microscope image showing the method of measuring the Raman intensity from a single spot. Here the arrow is composed of a 10 nm thick silver film on fused silica fabricated using EBL with a total area of approximately 1500 μm^2 and a focus in the range of 1 μm at 50X magnification. 75

Figure 5.6 – SEM images of a 10 nm films of (a) gold and (b) silver evaporated on fused silica substrates at 130 000 magnification. Thin metal films were used to compare Raman intensity variations between silver and gold films with immobilized protein A.76

| | |
|--|----|
| Figure 5.7 - Comparison of the SERS spectra of immobilized protein A on silver and gold films and on 100 nm pitch silver dots with 15 nm inter-dot gap distance with the Raman spectrum of the protein in solution at 2 mg/ml. Tests were done with a 532 nm excitation wavelength at 10% power except for the protein in solution which was obtained at full power. A significant difference was seen in a number of peaks after immobilization of the protein..... | 77 |
| Figure 5.8 - Spectra of protein A immobilized on 100 nm pitch silver dots with various inter-dot gaps taken with a 532 nm excitation wavelength and three 1s integrations of the Raman shifted wavelengths. | 78 |
| Figure 5.9 – Comparison of the intensity of the peak at 1380 cm^{-1} from immobilized protein A on silver dots with 100 nm pitch and varying inter-dot gap distances as well as comparison of the Raman signal protein immobilized on a silver film. | 79 |
| Figure 5.10 - Structure of a dopamine molecule visualized in Avogadro [125]..... | 81 |
| Figure 5.11 - ValFold predicted secondary structure of the dopamine binding aptamer modeled in PseudoViewer 3.0. The letters G, A, T, and C correspond to guanine, adenine, thymine, and cytosine nucleic acids, respectively. The long adenine string at the base was terminated with a thiol group to allow immobilization of the DNA with proper orientation..... | 82 |
| Figure 5.12 – Stacked Raman spectra of dopamine with 532 nm and 780 nm excitation compared with simulated peaks. Simulation and analysis was done using General Atomic and Molecular Electronic Structure System (GAMESS), Facio, and MacMolPlt software. Here the 532 nm and 780 nm excitation wavelengths were set to 2.1 mW and 2.7 mW respectively, with 4 s acquisition times across all wavelengths..... | 83 |
| Figure 5.13 - Spectrum of immobilized aptamer on gold honeycombs using a 780 nm excitation wavelength. Protein was immobilized for one hour at a concentration of $1\text{ }\mu\text{M}$ and the aptamer was placed for 10 min at $5\text{ }\mu\text{M}$ for this experiment..... | 84 |
| Figure 5.14 - Spectrum of immobilized aptamer on gold honeycombs using a 780 nm excitation wavelength. Peaks arising from ring bending between 700 cm^{-1} and 800 cm^{-1} were not seen, however similar peaks between 800 cm^{-1} and 900 cm^{-1} were observed. The spectra were smoothed for easier comparison. | 85 |
| Figure 5.15 - SEM images of (a) gold honeycomb structures and (b) gold film used for SERS detection of dopamine using DNA aptamers for immobilization..... | 85 |

List of Tables

Table 1 - Thermal Conductivity and Expansion of Bulk Silicon and Fused Silica. 61

Table 2 - Observed Raman Peaks of Protein A Compared with Published Data and Interpretation of Peaks 77

List of Abbreviations

CCD – Charge-coupled device

DFT – Density functional theory

DUV – Deep ultraviolet

EBL – Electron beam lithography

EDTA – Ethylenediaminetetraacetic acid

EUV – Extreme ultraviolet

FT- Raman – Fourier transform Raman

HFT – Hartree-Fock theory

HSQ – Hydrogen silsesquioxane

IPA – Isopropyl alcohol

MIBK – Methyl isobutyl ketone

NIL – Nanoimprint lithography

PMMA – Polymethylmethacrylate

SAM – Self-assembled monolayer

SCCM - Standard cubic centimeters per minute

SEM – Scanning electron microscopy

SERS – Surface-enhanced Raman spectroscopy

TMAH – Trimethylanilinium hydroxide

TRIS - Tris(hydroxymethyl)aminomethane

Table of Contents

| | |
|---|----|
| 1. Introduction..... | 1 |
| 2. Detecting Biological Molecules and Structures..... | 4 |
| 2.1. Biosensors..... | 4 |
| 2.2. Surface Enhanced Raman Spectroscopy..... | 6 |
| 2.2.1. Raman Scattering..... | 6 |
| 2.2.2. Surface-Enhancement of Raman Signals..... | 9 |
| 2.3. SERS Substrate Fabrication Methods..... | 11 |
| 2.4. Electron Beam Lithography..... | 14 |
| 2.4.1.1. Cold Development..... | 17 |
| 2.4.1.2. Anti-charging Conductive Layers for EBL..... | 18 |
| 2.5. Nanoimprint Lithography..... | 20 |
| 2.6. Motivation..... | 22 |
| 3. Experimental Methods..... | 23 |
| 3.1. Thermo Scientific Nicolet Raman Analysis System..... | 23 |
| 3.2. Raman Imaging and Sample Preparation..... | 24 |
| 3.3. Raith 150 ^{TWO} Electron Beam Lithography System..... | 25 |
| 3.4. NINT Electron Beam Lithography Simulator..... | 26 |
| 3.5. Nanonex NX-2500 Nanoimprint Tool..... | 26 |
| 3.6. Oxford Instruments PlasmaLab 100 ICP Etcher..... | 27 |
| 3.7. Cee 200X Spinner and Cee 1300X Hotplate..... | 28 |
| 3.8. Filmetrics Thin Film Measurement Tool..... | 29 |
| 3.9. Kurt J. Lesker Electron Beam Evaporator..... | 30 |
| 3.10. Hitachi S-4800 Field Emission Scanning Electron Microscope..... | 31 |
| 3.11. General Atomic and Molecular Electronic Structure System..... | 32 |
| 3.12. Molecule Building and Visualization..... | 33 |

| | |
|--|----|
| 4. Substrate Fabrication | 34 |
| 4.1. EBL Fabricated SERS Substrates | 34 |
| 4.1.1. Anti-charging layers in EBL..... | 35 |
| 4.1.2. Exposure and Development | 36 |
| 4.1.3. Comparison of Conductive Layers | 40 |
| 4.1.4. Summary of EBL fabricated devices | 51 |
| 4.2. Nanoimprinted SERS Substrates | 52 |
| 4.2.1. NIL Mold Fabrication | 52 |
| 4.2.2. Mold Etching | 55 |
| 4.2.3. Anti-adhesion Coating | 56 |
| 4.2.4. Nanoimprint Resist Properties | 58 |
| 4.2.5. Nanoimprint Process..... | 59 |
| 4.3. Electron Beam Evaporation, Lift-off, and Fabrication of Metal Nanostructures..... | 66 |
| 5. Biosensor Results and Discussion | 70 |
| 5.1. SERS detection of Protein A..... | 70 |
| 5.2. Aptamer Based Biosensing of Dopamine | 80 |
| 6. Conclusion and Future Work | 87 |
| 7. Works Cited | 91 |

1. Introduction

The ability to design, build, and organize at the nanoscale has brought into our reach a new and essentially unexplored field of research that allows control over molecular-sized features that behave, to a large extent, very differently than larger scaled devices with which we have previously worked. With nanotechnology, referring to dimensions ranging from 1 to 100 nm, there is an ever-increasing enthusiasm as advances in both fabrication and understanding at this scale promise profound technological changes. With all that has already been done, we are only still in the beginnings of what impact this field will have on our lives in the short term and in the future [1–3]. There remains much still to be discovered, with many areas of research still waiting to be explored involving nanotechnology, as Richard Feynman stated in 1960, “simply because we haven’t yet gotten around to it” [4]. The ability to engineer at the nanoscale provides difficult challenges where reproducibility, control, and stability of systems will require significant efforts, skills, and collaborations.

Concerns regarding outbreaks of infectious diseases, bioterrorism, pollutants, and other hazardous chemical or biological threats require the need for low-cost, accurate, and sensitive devices to provide warning of such dangers. Biosensors, which are devices aimed to detect such hazards as well as for detecting other chemicals or biological elements, such as with blood-glucose monitors, can be difficult to build. One area in which nanofabrication has shown great benefits is in biosensing. With an already significant world-wide market for different types of biosensors, some key benefits of nanoscale control can be realized in such areas as resonator mass-sensors [5, 6], field effect transistor based sensors [7], plasmonic sensors including surface-plasmon resonance (SPR) for measuring refractive index changes [8, 9], and surface-enhanced Raman spectroscopy (SERS) which provides a wealth of chemical bonding information

[10–16]. In particular, surface-enhanced Raman spectroscopy, while utilized and somewhat understood for some time now, has had limitations for practical use in biosensing that potentially can be overcome due to the significant advancements in nanotechnology.

In this thesis, nanofabrication methods including electron beam and nanoimprint lithography have been used to fabricate surface-enhanced Raman spectroscopy substrates with nanoscale control for the detection of proteins and other molecules using varying immobilization strategies. This work involves the testing of different plasmonic materials, and characterization of aspects of the fabrication process to gain a greater insight into the control at which features can be made. Testing of different analytes with varying metal geometry, material, pitch and spacing, allowed for tuning of the features to allow high enhancements with control over the intensities obtained. SERS spectra of different proteins showed that distinct signals could be seen while fluorescence became a significant problem for other proteins at high frequency excitation. Due to the surface sensitivity of SERS, a dopamine binding DNA aptamer was used for specific binding to allow for detection of binding to the dopamine molecule.

Chapter 2 in this thesis presents a literature review on biosensing, emphasizing surface plasmonic sensing SERS. This chapter will also cover some of the challenges that need to be overcome for practical use of such sensors including such aspects as material compatibility, nanoscale reproducibility, and immobilization requirements for detection. Details on some key aspects of nano-fabrication involved in building and testing nanobiosensors will be presented in this chapter to give a basis for the aspects involved in this research.

Chapter 3 discusses the details of the experimental techniques developed and used for the various aspects of biosensor fabrication, biofunctionalization, and detection of analytes including an overview of some of the key tools for fabrication and analytical testing.

Chapter 4 gives an overview of fabrication methods and results for nanoscale dielectric SERS substrates using electron beam lithography (EBL) and nanoimprint lithography (NIL) with their corresponding plasmonic enhancement.

Chapter 5 gives an analysis of the various detection capabilities and results obtained for different molecules, proteins and aptamer/ligand binding as well as simulation results of the Raman spectrum of different molecules.

Chapter 6 concludes this thesis by giving an overview of the results and analysis focusing on some of the items that seemed most significant in this work. An outlook on the future work that could be performed is also given.

2. Detecting Biological Molecules and Structures

2.1. Biosensors

Biosensors are analytical devices used for the detection or identification of specific analytes using living organisms or biological elements as the device's recognition component [17–19]. Biological elements used for detection commonly include antibodies/antigens [20], enzymes [21, 22], DNA [23, 24], prokaryotic and eukaryotic cells [25], organelles [26], and synthetic biomimetics [27, 28]. Aspects of biosensors often involve multiple stages of analysis and processing with a flow of information including: (1) exposure to a target in an aqueous solution or gas state; (2) molecular recognition receptors; (3) a transduction system to transform detected signals into a readable or interpretable form; (4) amplifiers and electronics to give data proportional to the detected signals; and (5) display and output to transmit and record the data for the end user (see Figure 2.1) [29, 30].

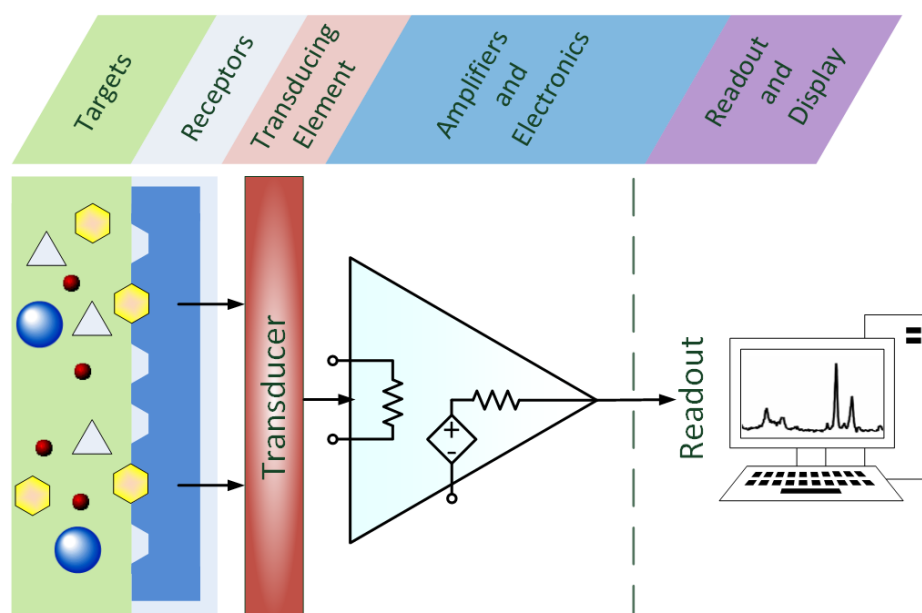


Figure 2.1 – Model of a common sensor system incorporating aspects of specific targeting of analytes using biological elements as receptor components, transducer elements, signal amplification and electronics, and readout display of signal for interpretation from the end user.

Molecular recognition is defined as non-covalent binding between two or more molecules where there is a strong and long-lived interaction arising from molecular complementarity [31–33]. Such longstanding interactions stem from non-covalent bonding such as electrostatic forces, ion-dipole interactions, π - π bonding, hydrogen bonding, and/or van der Waals forces between molecules [34, 35]. Molecular recognition is essential to life and involved in almost every stage of biological processes including DNA replication, protein synthesis, subcellular physiology of receptor-ligand interactions, and immune response involving antibody-antigen pairing [34–37]. Such interactions occurring at the molecular level provide a natural basis for biosensing technologies due to their highly targeted binding capabilities. A number of applications incorporating molecular recognition are now commonly used with a large and growing market, especially in self-testing devices for cholesterol, blood glucose, colon or rectal cancer, pregnancy, ovulation, and occult blood testing [38–40]. Molecular biosensing is usually focused on detection of biological agents such as bacteria cells and spores, viruses, metabolites, and toxins [41, 42]. It is recognized that the most vital factor in an effective biosensor is its specific molecular recognition capability, while other factors such as size, speed of operation, real-time monitoring, sensitivity, cost and accuracy of prediction (in avoiding false reporting) are all dependent on the specific requirements of the device or detection needs [41, 43]. There remains, however, many difficulties in bio-recognition or bio-detection where signal “reproducibility, sensitivity and poor signal-to-noise ratios” can limit the capabilities of detection for many different techniques [44].

One of the other significant challenges commonly involved in biosensing is the immediate detection of analytes for real-time sensing. Often, the need for fast analysis can be crucial for safety and health, where current biosensing modalities are limited. Quantitative analysis can also be an important aspect for a thorough assessment in some

circumstances, while the mere detection of higher (or lower) than expected values would be invaluable in other situations [41]. The underlying factors in any method ultimately come down to the method's capabilities and the requirements needed for a particular sensing device.

2.2. Surface Enhanced Raman Spectroscopy

2.2.1. Raman Scattering

C.V. Raman, in 1928, presented his discovery of “a new kind of radiation or light-emission from atoms and molecules” [45]. This phenomenon, known as Raman scattering, is an inelastic scattering of monochromatic light arising from vibrational modes of probed molecules. Although the number photons that are scattered by an atom or molecule is relatively low, the majority of photons that do experience scattering are due to elastic or Rayleigh scattering, where no new wavelengths of light are produced, with even fewer photons scattered by the Raman effect. In Raman scattering, where photons undergo inelastic scattering and have a resultant change or shift in frequency with lower frequencies corresponding to a lower energy (Stokes shift) or an increase in frequency or energy (anti-Stokes shift), leaving the molecule with a higher or lower vibrational energy after excitation depending on the resultant shift (see Figure 2.2) [46, 47]. These inelastically scattered photons provide unique information on the structure of the molecule. In contrast to fluorescence, where incident light is completely absorbed by the molecule and the molecule is transferred to an allowed quantum state before emission of a photon after a certain resonance lifetime, Raman scattering is mediated by short-lived virtual states of electrons. Such non-resonant scattering is what offers the unique fingerprint information, where shifts in energy remain constant regardless of the excitation frequency. The resulting shifts in the detected light wavelengths,

corresponding to different vibrational modes, are what offer the abundant information composing unique fingerprints for molecules (see Figure 2.3).

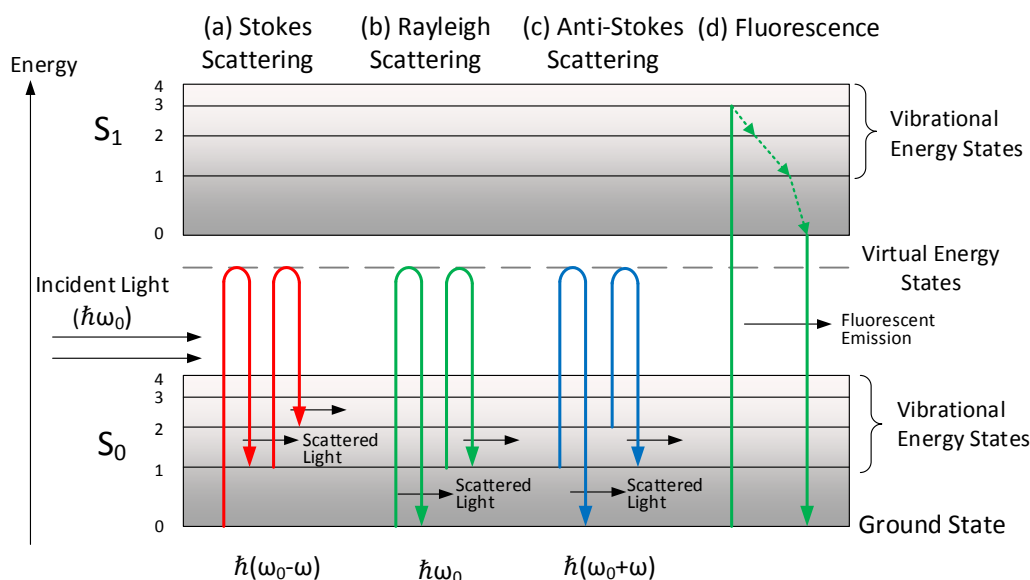


Figure 2.2 - Jablonski diagram showing the change in energies depending on the scattering type. (a, c) Stokes and anti-Stokes shifted Raman scattering, (b) Rayleigh scattering and (d) fluorescent emitted light [48].

Raman spectroscopy is a powerful technique for analytical sciences, yet a major limitation of the method is that the Raman scattering effect for molecules is very low. When compared to fluorescence, Raman scattering generally produces signals several orders of magnitude lower than fluorescence [10, 49, 50]. Cross sections of the scattering, which define the probability of inelastic scattering from a particular molecule, are typically in the range of 10^{-29} m^2 and lower, whereas fluorescent cross-sections can be up to 10^{-20} m^2 and higher [51, 52]. This low Raman cross section for most molecules generally requires large concentrations of the analyte and expensive sensitive detection methods and excitations sources to produce noticeable signals.

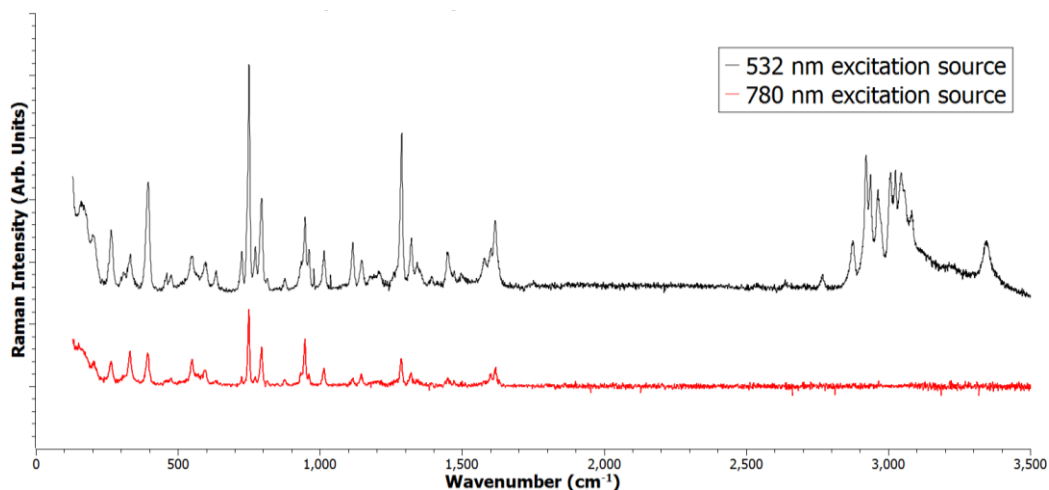


Figure 2.3 - Offset Raman spectra of dopamine powder from own work with 532 nm (black) and 780 nm (red) excitation laser. The shorter wavelengths show increased details but with a trade-off of increased fluorescence for some samples, such as DNA and some proteins. All detected spectra throughout this thesis display the Stokes-shifted spectra.

Only with advancements in many of the optics, including optical filters, low-cost lasers, and charge-coupled devices (CCDs), has Raman spectroscopy become widespread as a reliable analytical tool [49]. Usually molecules with the highest Raman activity are those susceptible to the highest change in molecular polarizability [50, 53]. To overcome weak Raman signals, reporter tags, analogous to fluorescent labeling, allow indirect detection, which has been shown to be effective at measuring very small quantities of analytes. This method, however, suffers from complexities involved in tagging and may not always be feasible for biosensing where certain molecules cannot easily be tagged. Ideally, direct detection of analytes without use of tags allows the most effective detection method for biosensing, which normally requires a molecule to be at least slightly Raman active.

Another challenge with traditional Raman spectroscopy is that weak Raman signals are often “washed-out” by fluorescence, often limiting work to non-fluorescent samples or working at longer wavelengths for improved detection with the trade-off of lower

signals for most peaks. Raman scattering efficiency has loosely been stated to decrease inversely proportional to the fourth power of the wavenumber difference according to the corresponding formula of the Raman intensity, $I_R \propto (\bar{\nu}_0 - \bar{\nu}_j)^4$ where $\bar{\nu}_0$ is the spectroscopic wavenumber of the excitation source ($1/\lambda_0$), and $\bar{\nu}_j$ is the wavenumber of the vibrational mode of a molecule (ν_j/c) [49, 54]. As seen in Figure 2.3, peaks above 2500 cm^{-1} disappear with a 780 nm excitation laser source. This can be attributed partially to this relationship, but more likely a low quantum efficiency of the CCD at longer wavelengths. Another disadvantage of longer wavelength excitation is the increased thermal and electric noise. Methods such as Fourier Transform Raman and improved CCD detectors have enabled Raman spectroscopy at longer excitation wavelengths but still signals can be weak and more difficult to work with [49, 55].

Simulation work predicting the vibrational modes of molecules using quantum chemical computation methods allows for an added understanding of Raman peaks and their corresponding vibrational modes. The General Atomic and Molecular Electronic Structure System (GAMESS) is one example of a chemical computation software which allows for the prediction of such vibrational modes (see also section 3.1.10) [56–58].

2.2.2. Surface-Enhancement of Raman Signals

In 1974, a published Raman experiment of pyridine adsorbed on a silver surface was reported [59]. Later, two groups independently presented and highlighted that the signals obtained were much stronger than expected and could not be explained by the regular Raman effect. Their arguments attribute the enhancement to both a chemical [60] and electromagnetic [61] interaction. These discussions were the first contributions to a technique now known as surface-enhanced Raman spectroscopy or scattering (SERS). Although the exact causes for enhancement are still under debate, it is

generally accepted that the overall enhancement is due to the interaction of the molecules with plasmonic waves in the metal [62], and to some extent, the chemical charge-transfer of the molecule with the surface. SERS involves the enhancement of scattered light from a probed sample due to plasmonic waves created at nanostructured surface. Plasmonics involves the interaction between electromagnetic fields and free electrons in metal. Electrons can interact with the electric component of light, and oscillate collectively due to the light waves. Enhancements well above 10^6 can be seen with some claiming enhancements of as much as 10^{10} [63, 64] using SERS. One of the key advantages of SERS is that it provides chemical bonding information of analyte materials and identification of samples, but recent efforts indicate a potential to provide quantitative analysis as well [12]. Biosensing using SERS in the last few decades has become an area of intense research with a significant increase [64] in studies involving SERS since the early 1980s [9, 13, 65]. There are a number of reasons why SERS has been suggested as such an effective methodology for biosensing. Many biological recognition materials require aqueous solutions to be stable [66, 67]. Because water, and other components found in complex buffers often have weak Raman scattering, background noise can be reduced by properly focusing laser light on SERS surfaces where analytes can be attached through an aqueous solution. SERS is highly dependent on metal substrate fabrication precision, so to a large extent, the challenge of creating an effective SERS biosensor has ultimately come down to a nano-engineering problem, where reproducibility of Raman signals depends on factors such as metal pattern geometry, spacing, size and position of metallic structures, all at nanoscale dimensions [9, 10]. This nanoscale control requires innovative nanofabrication techniques. The SERS effect also relies on the bio-functionalization of surfaces with the molecular recognition material, which is another significant biochemistry problem [11, 12]. The

many aspects of SERS biosensors involve multi-disciplinary studies across among a number of research fields.

2.3. SERS Substrate Fabrication Methods

A number of different methods for producing SERS biosensors have been demonstrated with increasing complexity in fabrication as higher control over the consistency in signal enhancement is required. Metallic spheres in solution offer unique abilities to detect analytes in the solution with in-vivo monitoring, but the method is limited in reproducibility of signal enhancements (see Figure 2.4). Changes in inter-metallic particle gaps can result in large fluctuations in Raman signals of adsorbed analytes due to regions of intense electro-magnetic signals between particles often referred to as “hot spots”. Signals arising from hot spots between particles can give misleading results due to the random nature of their motion [12, 63, 68, 69]. The ability to control such hot spots on a flat surface offers a number of advantages including the possibility to control metallic feature sizes and geometry [10]. Roughened metal surfaces, metallic nanospheres on a surface, and nanosphere lithography have been used extensively to provide high signal surfaces for SERS measurements. However, even such control over features such as metal particle sizes, pitch, and proximity to neighboring metallic features is crucial to validating SERS for reliable biosensing [70].

In order to fabricate highly reproducible SERS substrates, nanofabrication technologies such as electron beam lithography (EBL) and nanoimprint lithography (NIL) both offer advantages of nanometer-scale resolution with each having certain advantages and challenges in fabrication. Electron beam lithography, a standard for fabricating features with resolution down to below 10 nm [71–78] offers an effective method for fabrication of SERS devices due to the nanoscale control over features and flexibility in testing

different device designs. A major limitation in electron beam lithography, however, is the slow patterning or exposure.

Another emerging technology, which has quickly become an important nanofabrication technology, is nano-imprint lithography (NIL). NIL offers both high-resolution fabrication, and the potential for high throughput fabrication of devices. This technology requires the use of a mold or stamp, which is fabricated by EBL but can be used for the fabrication of a large number of subsequent “copies” of the original mold. NIL has been shown to also provide sub 10 nm resolution, with theoretical lower limits than what has already been demonstrated [79, 80]. Figure 2.5 illustrates the periodicity of features that can be fabricated at the nanoscale for the detection of biological agents.

Dielectric substrates have also been shown to significantly increase the intensities in SERS due to localized and focused fields existing at the surface between the metallic features [81]. Also, high quality fused silica, a clear glass with high transmission of optical wavelengths and excellent dielectric properties, provides transparency for SERS imaging with a very low background spectrum compared to many other substrate materials such as silicon [82, 83].

Fabrication on dielectric substrates, especially at the nanoscale, produces significant challenges with nanofabrication processing. Issues regarding charge build-up during fabrication, adhesion, and other factors need to be considered when working with glass or any type of insulating substrate. These difficulties can be overcome but require attention. The ability to fabricate on transparent dielectric materials could prove to be critical for fabricating SERS biosensors for detection of analytes in solution where the potential for microfluidic channeling would be beneficial [84].

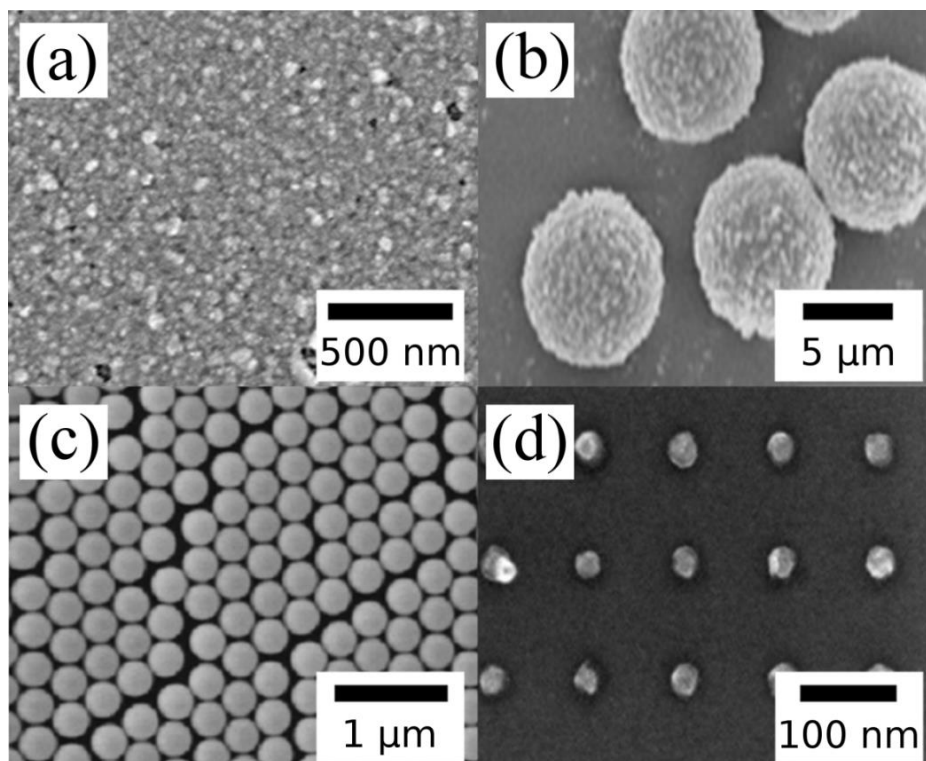


Figure. 2.4 - Some common SERS platforms for signal enhancement. (a) Roughened silver surface, (b) metallic spheres in solution [85], (c) nanosphere particle arrays [86], and (d) EBL fabricated periodic metal dot array. Images (b, c) published with permission. Images (a, c) obtained from experimental work.

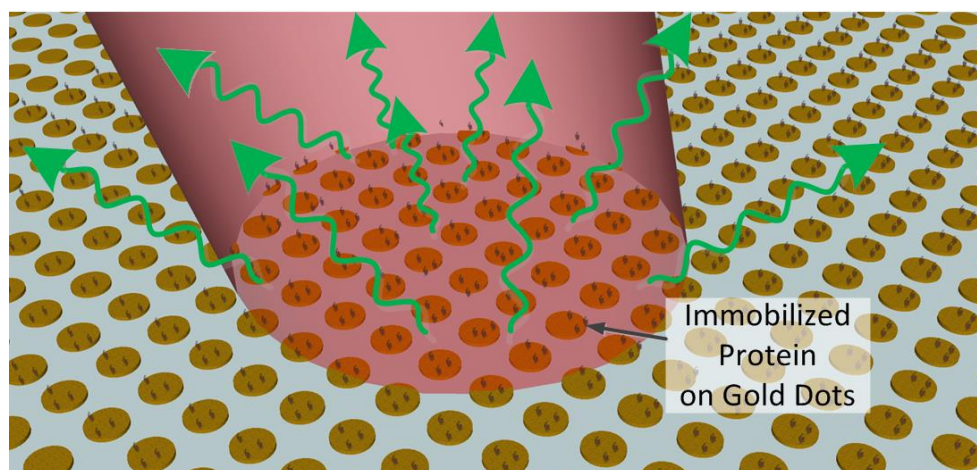


Figure 2.5 - Illustration of a laser beam focused on nano-patterned metallic dots with immobilized protein. The green arrows represent the scattered Raman light.

2.4. Electron Beam Lithography

Electron beam lithography (EBL) is an invaluable enabling technology for nanofabrication due to its flexibility for direct writing of sub 10 nm features, which is used for direct lithography as well as mask generation for deep ultraviolet (DUV) and extreme ultraviolet (EUV) technologies. In EBL, a beam of electrons, focused down to a spot as small as a few nanometers in diameter, scans across the surface of an electron-beam resist to generate a specific pattern, causing a change in the solubility of the resist in patterned or exposed regions. Electron beam (E-beam) resists that incur a higher solubility after exposure are known as positive tone resists whereas negative tone resists have a lower solubility after exposure. For many positive tone resists, such as poly(methyl methacrylate) (PMMA), ZEP520, and SML, electron beam exposure results in scission of the polymer chains composing the resist. The segmentation of the polymer chains into smaller fragments is what allows the resists to become soluble in the developer. For negative-tone EBL resists, such as hydrogen silsesquioxane (HSQ), Ma-N, and UVN30, low solubility is caused by cross-linking reactions creating larger, less soluble structures [73, 87]. The process of electron beam lithography includes: (1) Spin-coating of a uniform layer of electron beam resist on a substrate; (2) exposure of the resist material in a vacuum chamber with an electron beam patterned across the resist; and (3) development of the sample with a specific developer to remove the soluble regions (see Figure 2.6).

Ultimately, the resolution attainable is limited not entirely by the electron beam spot size but rather from a number of factors including resist chemistry, resist development after exposure, substrate charging due to poor charge dissipation of electrons during exposure, as well as from both forward and back-scattered electrons and their resultant generation of secondary electrons [73, 74, 77, 88]. So-called proximity effects in EBL

occur outside directly exposed areas due to forward and back-scattering. The effects of the beam energy play a major role in the EBL process with different energies being advantageous depending on the application. High energy ~ 100 keV electrons are able to penetrate deeper into the samples with less forward scattering of the beam [89], allowing higher resolution features. Proximity effects are more prevalent for high electron beam energies as the backscattered electrons travel a further distance in the substrate before they reach the resist. Trade-offs of lower pitch resolution due to increased back-scattering, higher doses as most of the electrons penetrate deep into the substrate as opposed to the resist, and possible damage to underlying features have also given rise to fabrication of features with lower energies in the sub 10 keV range [76, 90].

Mechanisms involved in resist development post-exposure also play a critical role in the quality and resolution of EBL-patterned devices. Collapse of the resist structure can occur during development and drying due to intermolecular or capillary forces between the liquid and the resist and depending on the mechanical strength of the resist. High aspect ratio features can be challenging to fabricate due to poor adhesion, and the resist structure. Resist swelling, during development, internal stress due to rapid post-bake cooling and thermal mismatching between the resist and substrate [91], and other developer properties are some of the many factors which control the resolution attainable in EBL [73, 92].

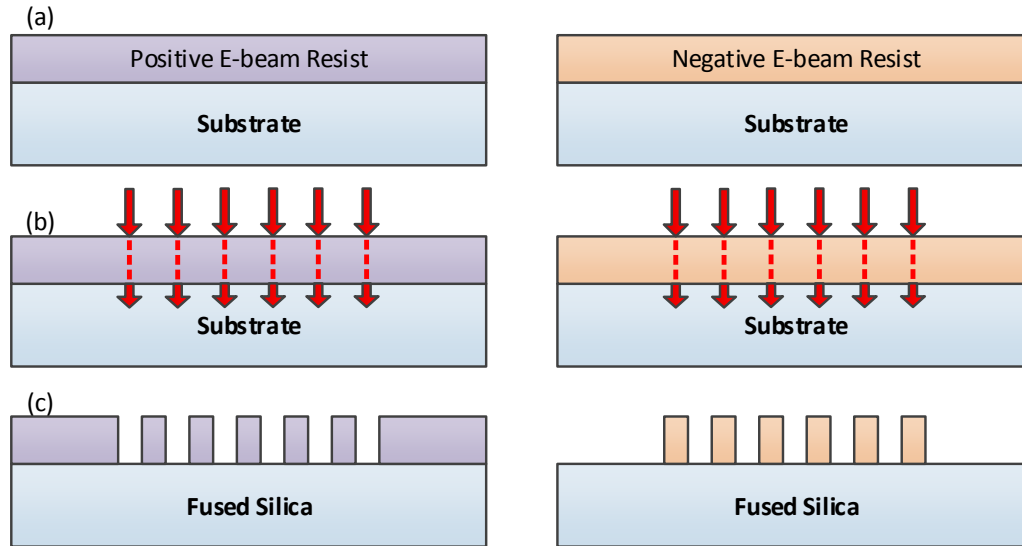


Figure 2.6 - EBL Process for positive (left) and negative (right) toned resists involving: (a) spin coating of resists; (b) electron beam exposure of patterned regions; and (c) development of resist to remove soluble regions.

Useful for testing different aspects of EBL, exposure dose scales can be helpful in determining the ideal parameters for the EBL exposure and development. Color variations of features seen with an optical microscope can give useful feedback about over-exposure, over-development, and clearance even though nanoscale features cannot be seen directly at low magnifications. Figure 2.7 shows an example of a 100 nm pitch array of dots where the dose per dot increases from left to right with the base dose being multiplied by the corresponding dose factor. The applicable dose window is referred to as a range of doses that allow well-defined features without degradation or combination between adjacent patterns.

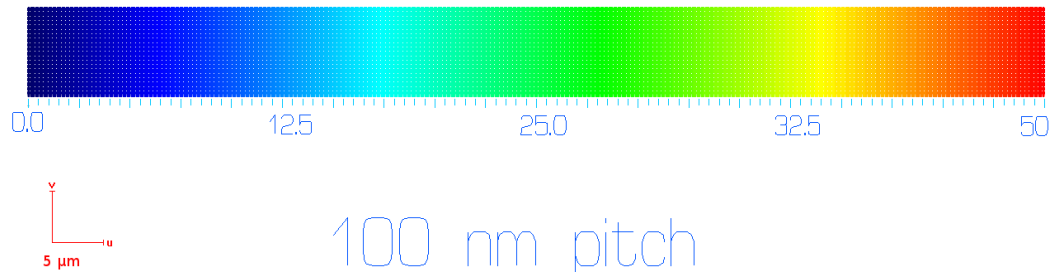


Figure 2.7 - CAD illustration of a 100 nm pitch dose grating with scale numbers and colors corresponding to different dose values (dose factors) of individual dots composing the array. Experimental results showed that the dot size of patterned features increased with higher dose factors, which varied depending on the fabrication process.

2.4.1.1. Cold Development

Cold development was employed to improve resolution for fabrication of features requiring greater resolution than possible at room temperature using positive tone resists [6, 73, 77, 93–95]. As the developer surrounds the resist fragments, a gel region is formed at the resist-solvent interface (see Figure 2.8). By cooling the developer, the solvent is less able to penetrate the partially exposed region, thus limiting the size and width of the gel region [96]. With the cooler temperatures, this reduces the solvent's ability to penetrate in unexposed resist areas, improving the resolution.

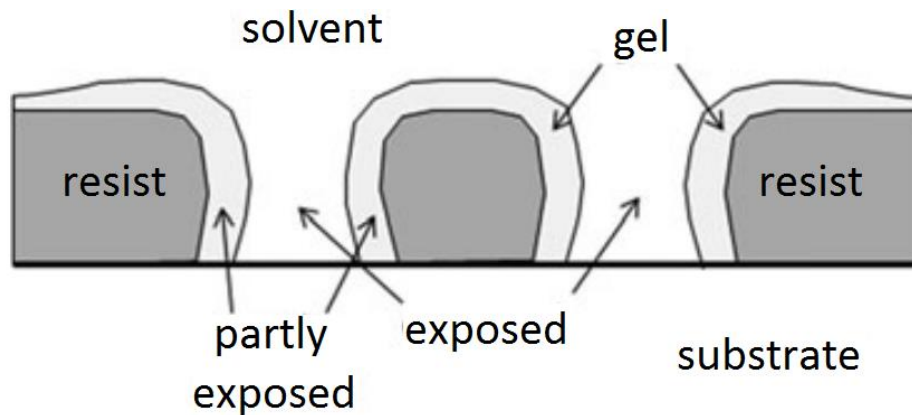


Figure 2.8 - Cross-section illustration of positive tone electron-beam resist during development. Gel formation occurs from interaction between the solvent and resist. Cooler temperatures during development prevent the gel region, which contains partially exposed polymer from being dissolved quickly, allowing increased resolution for electron-beam lithography. (Reproduced from [97]).

2.4.1.2. Anti-charging Conductive Layers for EBL

Charging effects during EBL processing can severely degrade the quality of patterned features during the exposure process, as beam defocusing, distortion, and displacement limit the resolution obtainable. Conductive layers, placed either above or below the resist layer have been shown to extend the resolution and quality of EBL by allowing discharging of the samples during exposure (see Figure 2.9 and Figure 2.10) [74, 99–101]. Figure 2.11 shows an image of a fused silica substrate, which requires conductive layers placed either above or below the resist layer, however, placement above the resist layer allows for no modification to underlying processes. Due to the complexity of working with conductive layers, simulation of the EBL process allowed for comparison with experimental results to determine the effects of electron beam broadening due to the conductive layers [101]. Figure 2.10 shows a schematic of the overall fabrication process using electron beam lithography and lift-off to produce the nano-structures for SERS.

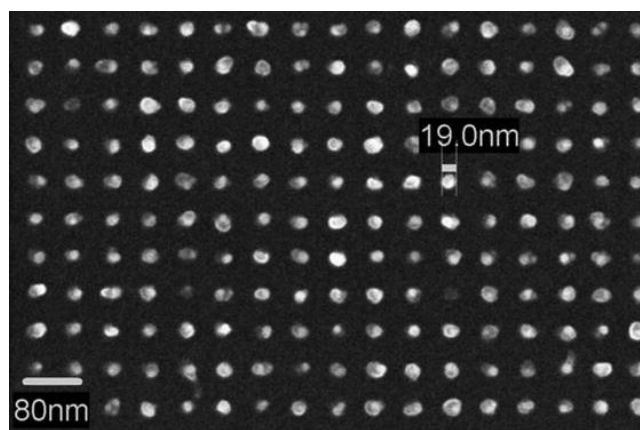


Figure 2.9 - 50 nm pitch gold dots fabricated on a fused silica substrates using a PMMA lift-off process and an anti-charging layer of aquaSAVE conductive polymer. Image obtained with permission from [74].

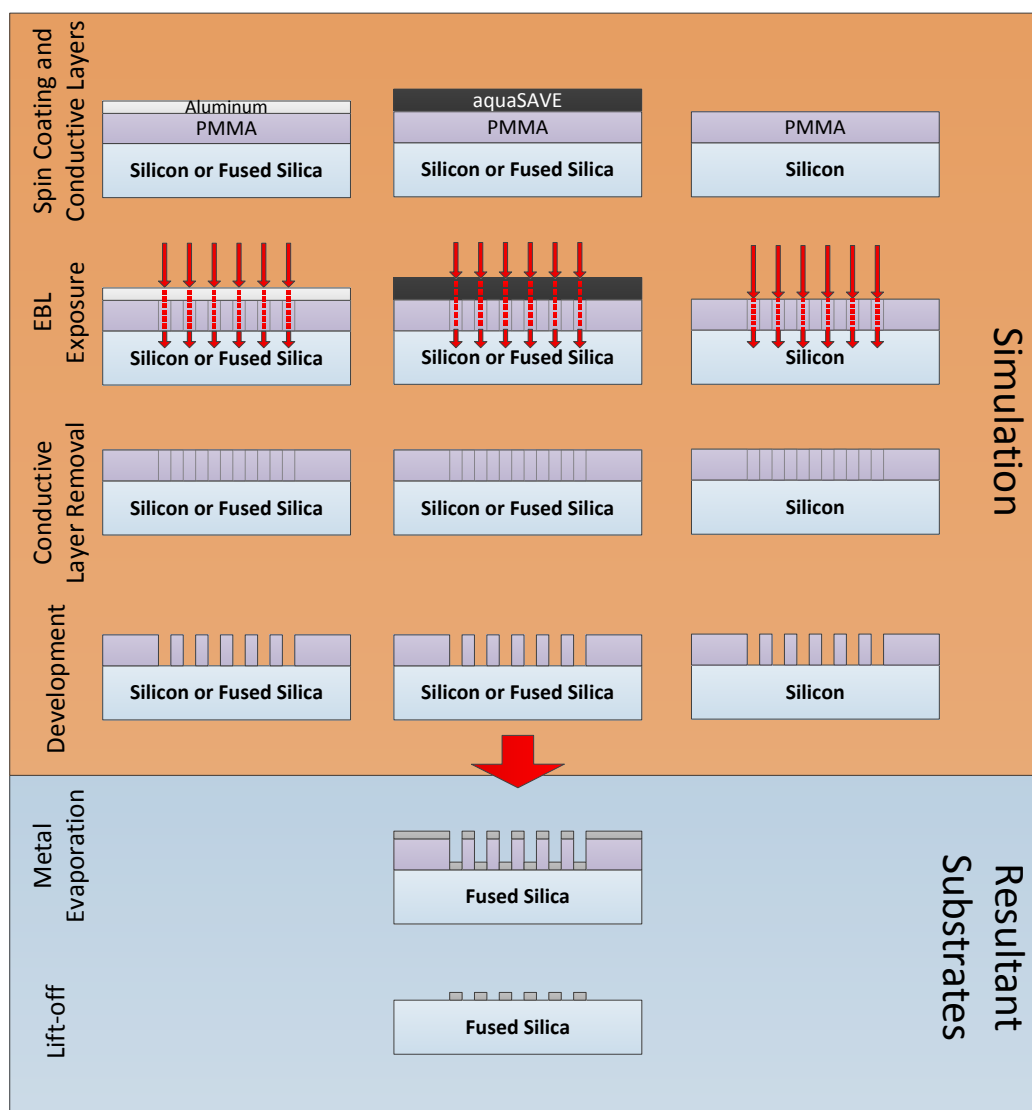


Figure 2.10 - Schematic of EBL fabricated substrates including simulation stage where the EBL Simulator was used to compare with experimental results for silicon and fused silica substrates investigating the effects of the conductive layers for different doses of 100 nm pitch holes in PMMA. Lift-off processing was done on fused silica substrates with aquaSAVE conductive polymer to obtain dot pitches ranging from 40 nm to 200 nm with varying gap sizes [74].

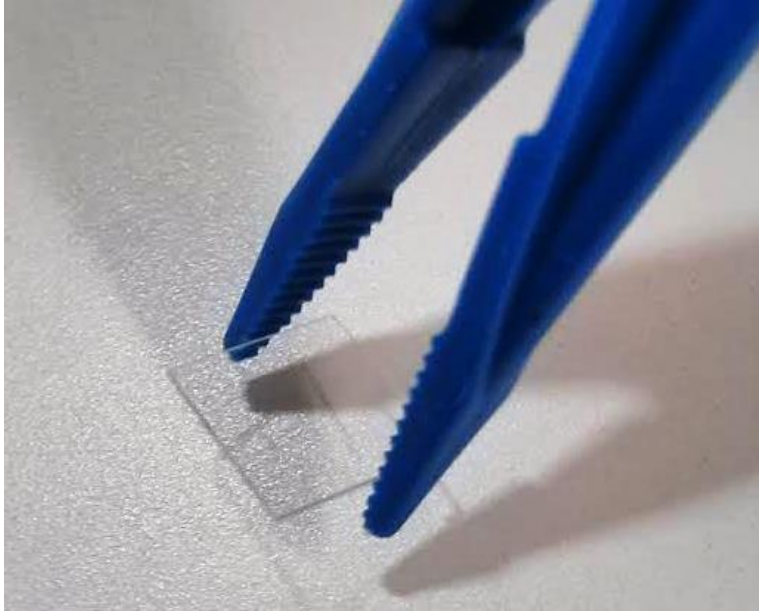


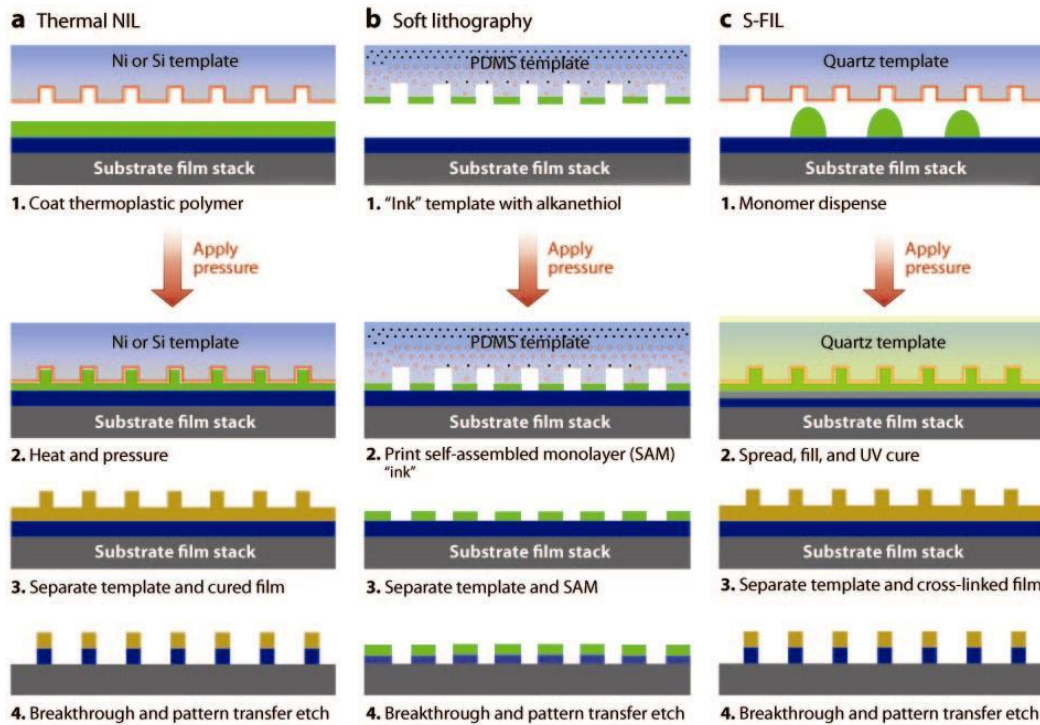
Figure 2.11 - Image of a fused silica sample used as a substrate material for fabricating SERS devices. Fabrication on fused silica substrates was done with both EBL and NIL as fused silica had excellent optical and electrical properties helpful for SERS.

2.5. Nanoimprint Lithography

Since the initial demonstration of nanoimprint lithography (NIL) in 1995 [102], it has quickly gained ground as a viable nanofabrication technology and considered a next generation lithography (NGL) possibility for microelectronics to replace photolithography as integrated circuit features reduce below 14 nm [103]. The potential low costs, simplicity and resolution of NIL have presented this technology as a viable solution to the semiconductor and other nanotechnology industries where commercial applications are beginning to emerge [104–106]. NIL is the process of transferring features from a high-resolution, patterned surface of a mold (or template) by pressing it into a deformable material (nanoimprint resist), and leaving a replicated copy of the original pattern in the new sample [80, 104, 107]. A number of variations on this process have been shown, with common methods including thermal, ultraviolet (UV) (used with step-and-flash), and soft lithography imprinting (see Figure 2.12) [83, 104, 108]. Some of the challenges involved with NIL include proximity effects due to

neighboring features displacing resist, sticking between the mold and sample, alignment, contamination after several imprints, and mold wear or damage [80, 107–110].

One of the challenges to overcome for NIL is reducing the adhesion or sticking between the mold and sample, where contamination and mold damage often occur after a number of consecutive imprints. Methods to reduce the sticking have evolved, usually consisting of some type of chemical modification to the mold or to the resist material itself or to both in order to lower their surface energies, improving separation [107, 111, 112].




 Costner EA, et al. 2009.
Annu. Rev. Mater. Res. 39:155–80

Figure 2.12 - Process steps for the three basic nanoimprint lithography (NIL) techniques: (a) thermal nanoimprint lithography, (b) soft lithography (microcontact printing), and (c) ultraviolet (UV) (step and flash) nanoimprint lithography (S-FIL) (Reproduced with permission [104])

2.6. Motivation

As a major challenge involved in SERS, control over features at nanoscale dimensions is critical for reliable detection for biosensing applications. In this work, nanofabrication methods including both electron beam lithography and nanoimprint lithography were used to fabricate SERS substrates which were tested for their capabilities as SERS biosensors. Aspects of fabrication, with variations in plasmonic structures for increased signal and control over Raman signal enhancements, required significant adjustments in the various stages of fabrication to improve consistency and signal enhancement. Testing of the SERS signals from different analytes to determine the effectiveness of the devices was critical to this work. Different metals, geometries, feature spacing and pitch, as well as other aspects of substrate preparation required continual analysis and feedback from the measured SERS spectra of different analytes used for testing. SERS spectra of different biological elements including proteins, DNA aptamers, and small molecules, were used for benchmark testing and eventual demonstration of bio-detection using targeted molecular complementarity.

3. Experimental Methods

This chapter provides a summary of some of the key fabrication tools and software used in this work. Measurement and imaging tools used for evaluation and analysis of experimental work are also included in this chapter.

3.1. Thermo Scientific Nicolet Raman Analysis System

The Thermo Scientific Raman system used in this work allows both microscope and macro imaging with microscope magnification to 100X. This capability has allowed accurate analysis to determine which regions of substrates produce the highest Raman signal down to 540 nm resolution. The system allows for imaging with both 532 and 780 nm wavelength excitation with charge-coupled device (CCD) cooling down to -100 °C for improved signal-to-noise imaging, especially at 780 nm wavelength excitation. The software provided also allows for advanced subtraction of signals using custom databases as well as imported Raman spectra libraries for effective signal processing and interpretation. The system is also capable of remote sensing with an optical fiber cable, which although not used in this work, would be beneficial for the commercialization of future SERS devices [113].



Figure 3.1 - Thermo Scientific Nicolet Almega XR Micro and Macro Raman Analysis System used for Raman spectroscopy of signals from SERS substrates and other spectra. The system has both 532 and 780 nm excitation sources with CCD cooling to $-100\text{ }^{\circ}\text{C}$ for low noise detection of Raman signals (www.thermoscientific.com).

3.2. Raman Imaging and Sample Preparation

To allow Raman imaging of sensitive analytes, an aqueous environment needs to be maintained for both immobilization and imaging of analytes. Thus, substrates were placed in a buffer solution and capped with a thin glass cover, which has low impurities to avoid adding background to the Raman spectra. The samples were submerged in a compatible buffer and sealed in the solution using a hydrophobic vacuum sealant (see Figure 3.2), which did not appear to result in any noticeable contamination to the samples. Raman measurements of the silicone-based vacuum sealant, were done and compared with every run to assure that contamination from the sealant was not seen in the spectra.

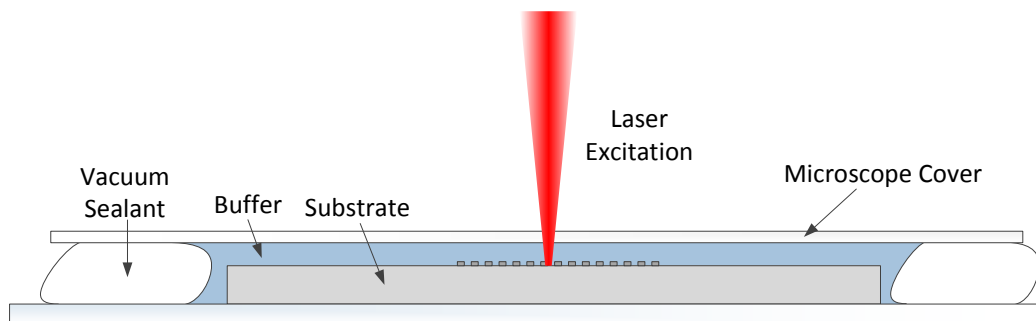


Figure 3.2 - Samples were kept in a buffer solution during Raman imaging, as many biological analytes require specific conditions to prevent degradation. The samples were sealed in the buffer solution with a transparent microscope cover.

3.3. Raith 150^{TWO} Electron Beam Lithography System

The Raith 150^{TWO} system offers the flexibility of providing high-resolution patterning with a range of low accelerating voltages from 0.1 keV – 30 keV. It offers load locking of samples with up to 8" wafer handling and stitching errors below 25 nm, and is capable of sub-10 nm feature patterning.

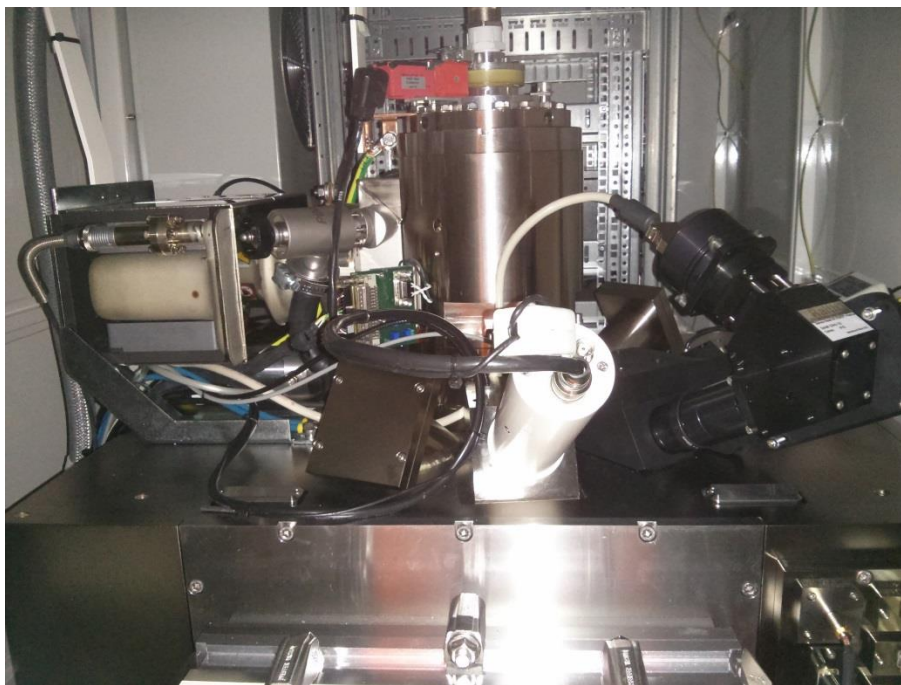


Figure 3.3 – Image of the column and detector components of the Raith 150^{TWO} electron beam lithography system which is used at the University of Alberta (www.raith.com).

3.4. NINT Electron Beam Lithography Simulator

Our group has developed the NINT electron beam lithography simulator which allows both the visualization and analysis of EBL structures with nanometer resolution. The tool allows of high accuracy predictions, with significant control over a number of parameters to allow adjustments to theoretical calculations of both the exposure, and development stages. Various options include choice over substrate material, resist thickness for both ZEP and PMMA, development time, temperature, and a number of other features [6, 114]. The simulator predicts the spatial distribution of the yield of scission of polymer chains occurring from the impact of primary, secondary, and backscattered electrons. This then is employed to determine the development parameters for different developers IPA:H₂O (7:3) for PMMA, ZED-N50 for ZEP and MIBK:IPA (1:1) for both [6, 95, 101, 114].

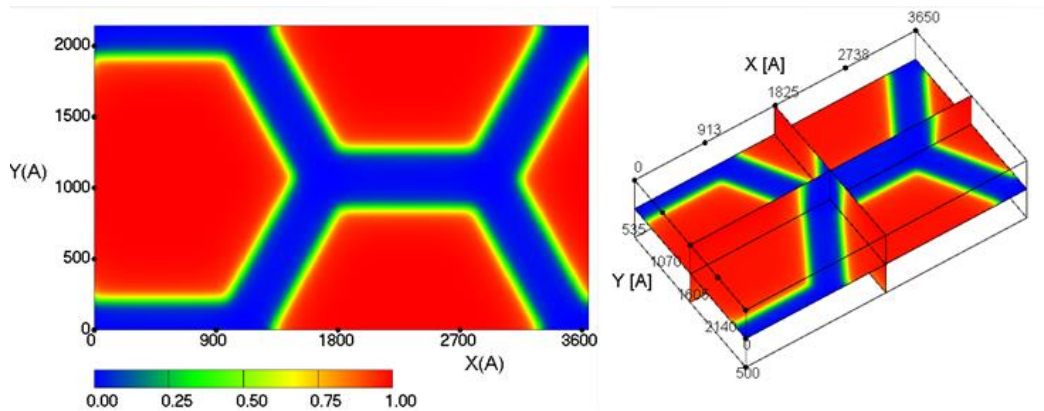


Figure 3.4 - Top view (left) and 3D (right) visualization of the yield of scission for PMMA 950K using the NINT Electron Beam Lithography Simulator. The software is able to predict both exposure and development patterns in PMMA and ZEP resists. The units displayed are in Angstroms.

3.5. Nanonex NX-2500 Nanoimprint Tool

The nanonex NX-2500 nanoimprint system offers both UV and thermal imprint capabilities with sub 1 μm alignment and sub 10 nm resolution imprinting. The unique

air cushion press systems allows for a range of different sample sizes and shapes. In this thesis, all samples were $\sim 1 \times 1$ cm diced squares. Experiments in this work included thermal imprints using a NXR-1025 thermal imprint resist (Nanonex Corp.).



Figure 3.5 - Nanonex NX-2500 Nanoimprint system used for nanoimprinting. The tool allows for both thermal and UV imprinting (www.nanonex.com).

3.6. Oxford Instruments PlasmaLab 100 ICP Etcher

The Oxford Instruments PlasmaLab system is an inductively coupled plasma etching system that allows for anisotropic etching which is ideal for lift-off and nanoimprinting as sidewall coverage during evaporation can prevent proper lift-off from occurring. With liquid nitrogen cooling, the system also gives improved anisotropy as etched resist in deep trenches is more likely to be re-deposited on sidewalls, which further improves the lift-off of metal.



Figure 3.6 - Oxford Instruments PlasmaLab System used for etching of NIL molds and NIL substrates (www.oxford-instruments.com) .

3.7. Cee 200X Spinner and Cee 1300X Hotplate

The Cee 200X spinner and hotplate (Brewer Science), allows for spin coating of samples with a high torque for fast ramp rates and spin speeds of up to 10 000 rpm. The top cover design improved consistency of the resist thickness from run to run compared to other spinners that were used where rates were inconsistent due to varying air flow.



Figure 3.7- Cee 200X spinner (left) and hotplate (right) from Brewer Science used to spin and bake substrates for EBL and NIL (www.brewerscience.com).

3.8. Filmetrics Thin Film Measurement Tool

The filmetrics thin film measurement tool uses spectral reflectance information from a range of wavelengths to determine thin film thicknesses. The tool was used extensively to measure the different thickness of thermal oxides, EBL and nanoimprint resists, as well as to determine the etch rates needed for NIL mold fabrication and clearance etches. The tool was also able to measure resist thicknesses on fused silica substrates with 10-20 nm accuracy and 0.01 nm accuracy on opaque substrates such as silicon.

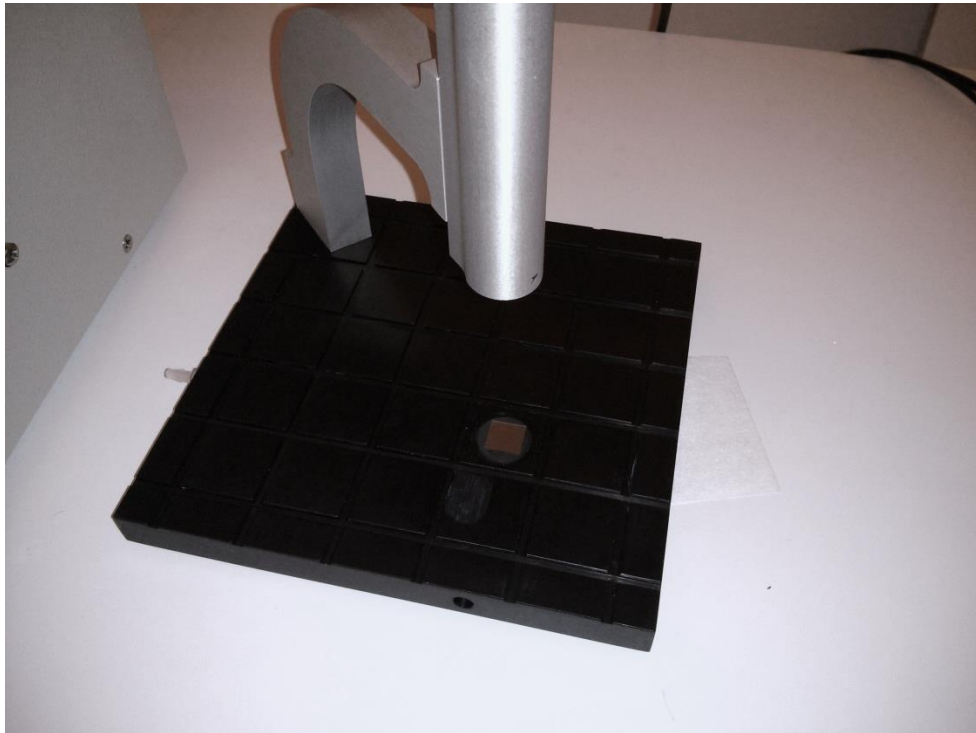


Figure 3.8 - Filmetrics measurement system used for measuring thin film thicknesses on various substrates. Thickness measurements were obtained with resolution and accuracy less than one nanometer for many resists thicknesses measured.

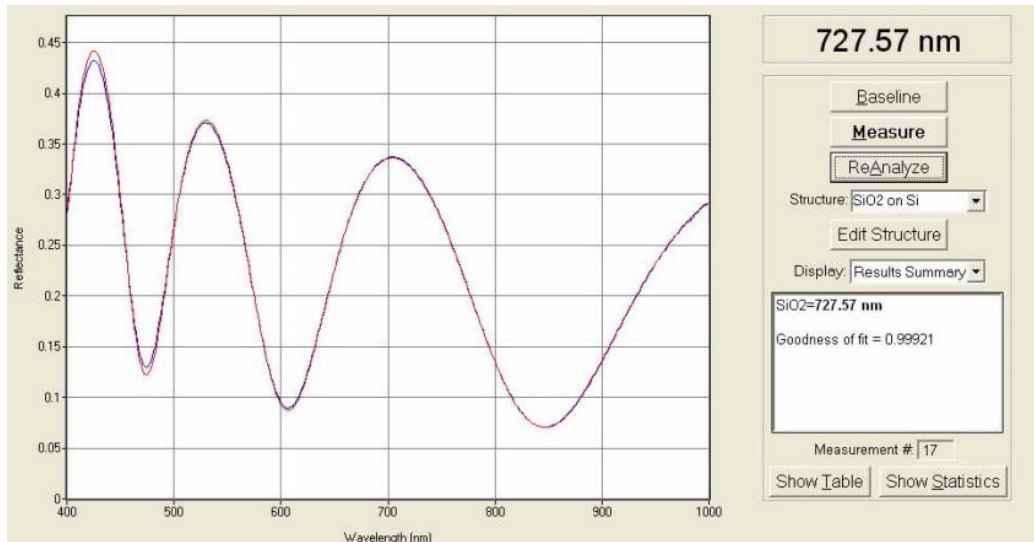


Figure 3.9 - An example of the measurement display interface of the filmetrics thin film measurement system. Accuracy of the measurements was within a few nanometers.

3.9. Kurt J. Lesker Electron Beam Evaporator

The Kurt J. Lesker evaporator is a physical vapor deposition tool for electron beam evaporation of various materials. The system allows loading of up to four metals, held in crucibles, allowing multiple material layers to be added, which is often needed for adhering some metals such as silver or gold to a surface using a metal such as chromium or titanium as an adhesion promoter. The system is a bell jar setup which allows a significant distance between the samples and the metal crucible which provides improved directionality for lift-off. The crucibles are water cooled from below and give a uniform temperature gradient within the heated metal allow for consistency between runs. The system is able to reach a base pressure of below 7×10^{-5} Pa ($\sim 5 \times 10^{-7}$ Torr) within 2 hours.



Figure 3.10 - Kurt J. Lesker water-cooled, bell jar, electron-beam evaporation system with cryo-pumped chamber and four-pocket crucible holder.

3.10. Hitachi S-4800 Field Emission Scanning Electron Microscope

The Hitachi S-4800 field emission scanning electron microscope offers a maximum of 1 nm resolution with acceleration voltages between 0.6 keV and 30 keV. The system has both secondary and backscattered electron detectors, which can be used in parallel to provide both surface and atomic variation imaging. This was utilized for imaging of the metallic features on fused silica due to the contrast in atomic number between the metal and the SiO₂ glass. The system is cooled using liquid nitrogen for improved resolution and stability.

3.11. General Atomic and Molecular Electronic Structure System

The General Atomic and Molecular Electronic Structure System (GAMESS), is a simulation tool used to give approximations of the electron wave function and energies of stationary molecules [56-58]. In this work, GAMESS software was used for the prediction of Raman bands in molecules. Although the Raman spectrum for immobilized species can change, especially due to the surface-enhancement of Raman signals, simulation gives helpful insights into both the Raman activity of molecules as well an understanding of chemical interactions that occur [115]. The basic components in determining the Raman spectrum used in this work involved the stages of, (1) geometry optimization and nuclear gradient calculations; (2) Hessian matrix calculation based on predicted potential energies of molecules; (3) calculation of the vibrational modes of the molecules using the Hessian matrix calculations; and (4) determination of the intensities of the different vibrational modes.

Geometry optimization was done using a closed-shell, restricted Hartree-Fock (RHF) method for all molecules, as their valence shells were all full initially. Ions or radical molecules would require a restricted open-shell Hartree-Fock calculation (ROHF) [116]. The basis set for each molecule was chosen as 6-31G(d,p) basis set where the lower core orbitals remained stationary for the calculations [117-119].

The Hessian matrix, which is the second order derivative of the potential energy of the molecule, is calculated with respect to the nuclear or Cartesian coordinates of the molecules, and is used to determine the vibrational modes of the molecules [120, 121]. The Raman intensities were then calculated using a numerical differentiation procedure where electric fields are applied in various directions towards the molecule with electric

field strength of 0.002 N/C to determine intensity of different Raman modes arising from different angles of light [122]. One limitation of the Raman package provided is that the excitation laser wavelength is not incorporated into the calculations causing some discrepancy in the obtained Raman intensities of the molecules.

3.12. Molecule Building and Visualization

Preparation of simulated molecules for GAMESS was done using the Simplified Molecular-Input Line-Entry System (SMILES) [123] for input into Avogadro, an open-source molecular builder and visualization tool [124]. Proteins and their crystal structures were also imported into Avogadro for visualization (see Figure 3.11). Modeling of resultant simulations and visualization of the Raman vibrational modes was done using MacMolPlt [56] and Facio [125, 126], which both offer molecular modeling and visualization for GAMESS.

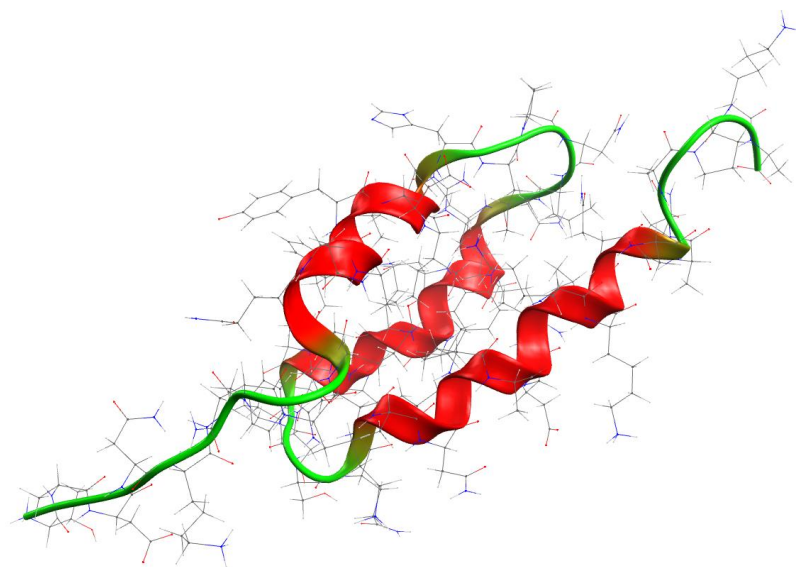


Figure 3.11 - Avogadro: an open-source molecular builder and visualization tool was used to build and visualize different molecules and proteins. This image contains a simple wireframe and cartoon view of the recombinant B domain of staphylococcal protein A obtained from the RCSB Protein Data Bank (1BDD) [127]. Modified protein A was used for benchmark testing for SERS bio-detection.

4. Substrate Fabrication

Variability in the signal enhancement from SERS occurs predominantly from irregularities in shape and positioning of metallic features at the nanoscale. Regions of high signal enhancement or “hot spots” that exist in nanoscale gaps between metal features, due to highly localized electromagnetic fields in the gaps that arise from laser irradiation, can be difficult to control and reproduce uniformly with many conventional fabrication methods. In this chapter, aspects of fabrication using electron beam and nanoimprint lithography are presented for the fabrication of SERS substrates with nanoscale control for reliable signal enhancement. The requirement for placing anti-charging layers on substrates to allow fabrication on dielectric substrates is included with a detailed study on various aspects involved in the application of such layers.

The work towards these goals includes substantial efforts from previous and current group members including Mustafa Muhammad who established many of the methods for EBL fabrication on dielectric substrates, Luis Gutierrez-Rivera, who I worked with closely throughout in testing numerous aspects of design, and fabrication of different features and Marium Japanwala who assisted in designing and fabricating honeycomb and other structures. Figure 4.31 was provided by Luis Gutierrez-Rivera, as an example of the gold honeycomb structures fabricated on fused silica. Considerable collaboration with Taras Fito in using the EBL Simulator, interpreting data, and preparing graphs was done, including assistance in preparing figures 4.4, 4.7-4.8, and 4.10 [101].

4.1. EBL Fabricated SERS Substrates

Substrates of fused silica were used as a base structure to allow fabrication of plasmonic features that could be used for detection of analytes using SERS. Silicon substrates were also used for testing at different fabrication steps to: (1) measure and adjust resist

thicknesses; (2) determine the effects of anti-charging layers during EBL exposure on non-dielectric substrates, including electron beam broadening due to the additional layers; and (3) evaluate the effects of post-exposure processing on resist thickness, adhesion, and surface roughness. Diced 1 cm × 1 cm samples were cleaned to remove organic and metallic contaminants in a piranha (H₂SO₄:H₂O₂ 3:1) bath for 15 min, then rinsed in deionized water and dried in nitrogen. Samples were then baked on a hotplate at 180 °C for 15 min as a dehydration step to improve adhesion of the resist and the subsequent metal layers to the surface of the samples. The substrates were then cooled to room temperature, spin-coated with PMMA 950K (MicroChem) and baked at 180 °C for 3 min to drive out the solvent and reduce stress. Depending on the age of the PMMA used, film thicknesses varied from 90 nm to 100 nm due to solvent evaporation over time. It was found that a 2-s ramp to a range between 3500 rpm and 4000 rpm was needed, depending on the condition of the resist. PMMA thickness was verified using the Filmetrics thin film measurement tool for each batch.

4.1.1. Anti-charging layers in EBL

Samples of both silicon and fused silica were spin-coated according to the previously stated parameters with 100 nm thick PMMA 950K and conductive layers were added on top. Physical vapor deposited aluminum and spin-coated poly-aniline based conductive polymer aquaSAVE (Mitsubishi Rayon Co.) were used as demonstrated elsewhere [74,128] to compare the results of the two conductive layers and for comparison with the simulated results. Conductive layers can be placed both above and below the resist layer; however, placement above the resist layer allows underlying processes to remain unmodified. It was found that for the aluminum layer, deposition using a planar magnetron sputtering system damages the top layer of resist, resulting in up to a 20 nm reduction in the resist thickness after development. Electron beam evaporation did not

appear to have any effect on the thickness of the resist after development. Evaporated aluminum films were deposited at a pressure of $\sim 7 \times 10^{-7}$ Torr and a deposition rate of 0.02-0.03 nm/s using the Kurt J. Lesker evaporation system for all the samples used in the testing. Aluminum thicknesses ranging from 10 nm to 30 nm were used to compare the effects of conductivity and beam broadening from varying thicknesses.

Samples using the conductive polymer for anti-charging were spin-coated with aquaSAVE at 3000 rpm for 40 s with a 2 s ramp. To allow proper coating of the aquaSAVE layer, the liquid needed to be spread across the surface with a dropper to prevent streaking of the polymer during the spin process. The thickness of the aquaSAVE was estimated to be approximately 70 nm.

4.1.2. Exposure and Development

Patterns used for fabrication of SERS substrates were created using computer aided design (CAD) software, to generate GDSII format elements that were utilized by the EBL software to transfer the design to the substrate by exposing the resist layer with the electron beam. EBL exposure dose involves the number of electrons to be applied to a single spot or an overall area or line and is measured in units of electric charge applied to a region. Higher beam energies require a higher dose as a larger percentage of energetic electrons pass through the resist into the substrate with a lower yield of scission. This can be described by an optimal area, line, or dot exposure dose, depending on the structure, usually measured in units of C/cm^2 , C/cm , and C/dot respectively. Area and line doses are commonly composed of individual dots, which are spaced close enough to allow the dots to combine, creating larger features.

Development of the samples was done using a co-solvent of IPA:H₂O (7:3) which has been shown to provide better development than either solely IPA or H₂O which are both

weak developers [74, 95]. For both silicon and fused silica substrates, there was found an applicable dose window, which was larger at higher beam energies. This window greatly depends on the development process as seen in Figure 4.1 which shows a large area of 100 nm pitch dots or pits in developed PMMA resist which gradually increase in size dependent on the increasing dot dose factor.

Honeycomb and other structures for SERS devices were fabricated at both room and cold temperatures with the idea of allowing for increased surface coverage, and narrow gap SERS hotspots [129]. Compared to MIBK:IPA (1:3) which is often used for cold development at temperature below 0 °C, IPA:H₂O (7:3) has been shown to give more reliable nanoscale fabrication results of features while providing reduced line-edge-roughness [95]. IPA:H₂O (7:3) has also been shown to offer up to 40% better sensitivity and 20% higher contrast than MIBK:IPA (1:3) under certain conditions [130]. In order to provide the highest resolution, a temperature of +12 °C was used and samples were developed for 60 s. Temperatures below +12 °C are not advantageous as long development times and higher doses can both cause increased resist swelling and larger effective radii of gyration of the polymer in the solvent, which can limit the ultimate resolution attainable [130].

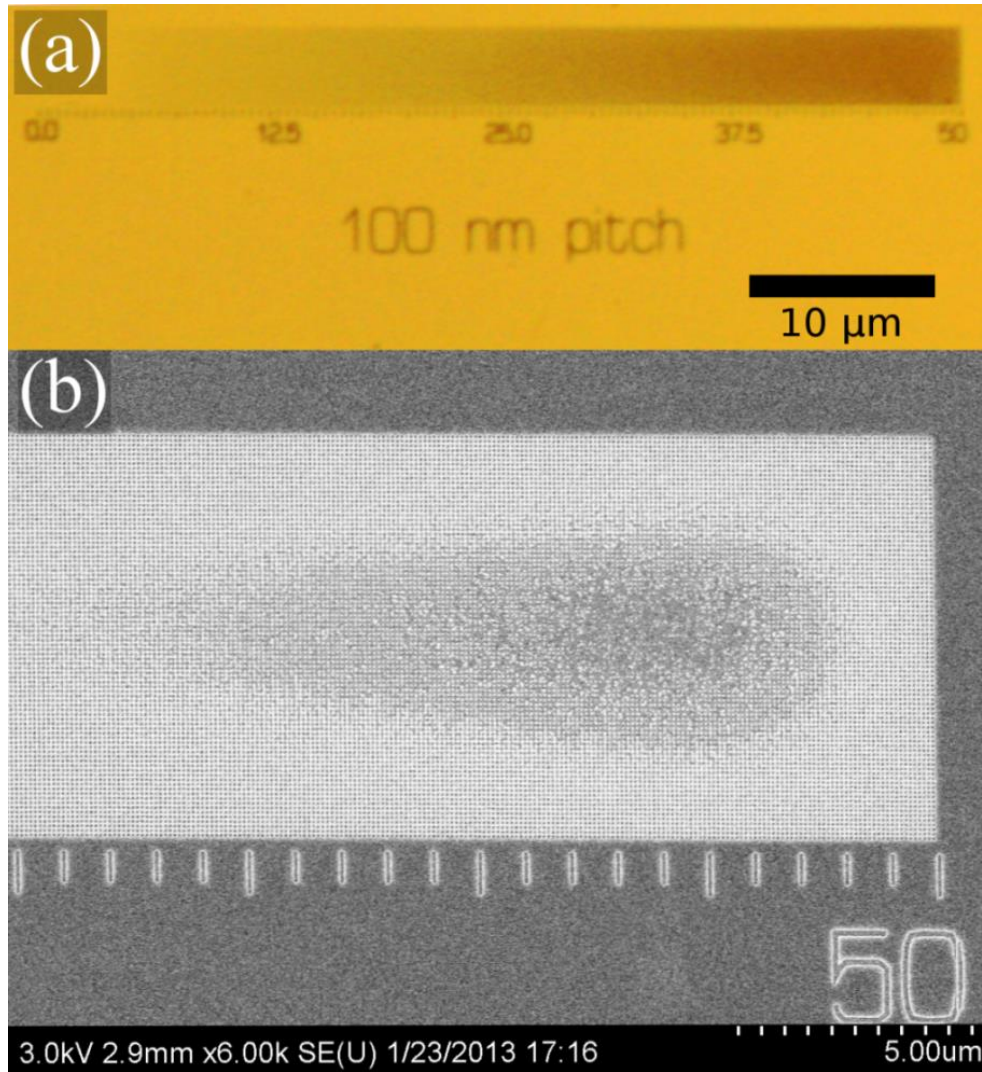


Figure 4.1 - Arrays of 100 nm pitch dots in PMMA on fused silica substrates developed using an IPA:H₂O (7:3) development process. One-hundred nm pitch dots or pits in developed resist over a large area can be seen in: (a) an optical image of a substrate developed at 12 °C; and (b) a SEM image of a sample developed at room temperature at higher magnification showing collapse at high dose factors close to 50 in the central regions due to a higher effective dose. Values on scale bar correspond to a dose factor with a base dose of 0.6 fC/dot, which gradually increase to the right. Experimental results found an approximate 5 nm average dot size variation for every 10 μm distance for cold development.

Prolonged development times are also known to result in degradation of resist-substrate adhesion, which can also lead to collapse. It was observed that the stir sticks could not be operated prior to development as bubbles formed in the developer and remained for up to a minute [73, 131]. It is likely that the bubbles are due to a higher evaporation rate

of IPA than H₂O at cool temperatures [132]. If the bubbles were not allowed to rise prior to development, bubbles would adhere to the surface of the substrate and cause circular regions of undeveloped resist where the bubbles attached. One important aspect of cold development for SERS substrates is that with an increased applicable dose window for varying doses, increased consistency and control over dot size over a range of doses was observed (see Figure 4.1). This is important, as small inter feature gap variations between metal structures is known to have a substantial impact on Raman signal intensities.

Simulation work involving honeycomb and other structures was done for the prediction and interpretation of the experimental work. In order to obtain narrow gaps between metallic features for producing Raman hot spots, adjustments to the electron beam exposure dose, development temperature and time allowed for the fabrication of consistent narrow resist features with honeycomb shaped structures. Comparison with simulation for samples using cold development showed accurate predictions for test samples with silicon and fused silica substrates. Figure 4.2 shows an example of PMMA honeycomb structures fabricated on a silicon substrate. Simulation of the honeycombs with a 150 $\mu\text{C}/\text{cm}^2$ average area dose showed that a residual layer of resist remained after development, which was also seen in experiment, as 150 $\mu\text{C}/\text{cm}^2$ was the starting threshold dose for clearance on most chips. This was confirmed after lift-off in many cases as insufficient clearance during development prevented gold from adhering directly to the underlying substrate. Honeycombs made with 90 nm thick PMMA had features with widths down to ~20 nm. However, reaching a consistency with honeycomb shaped structures was difficult for producing gaps between structures below 30 nm.

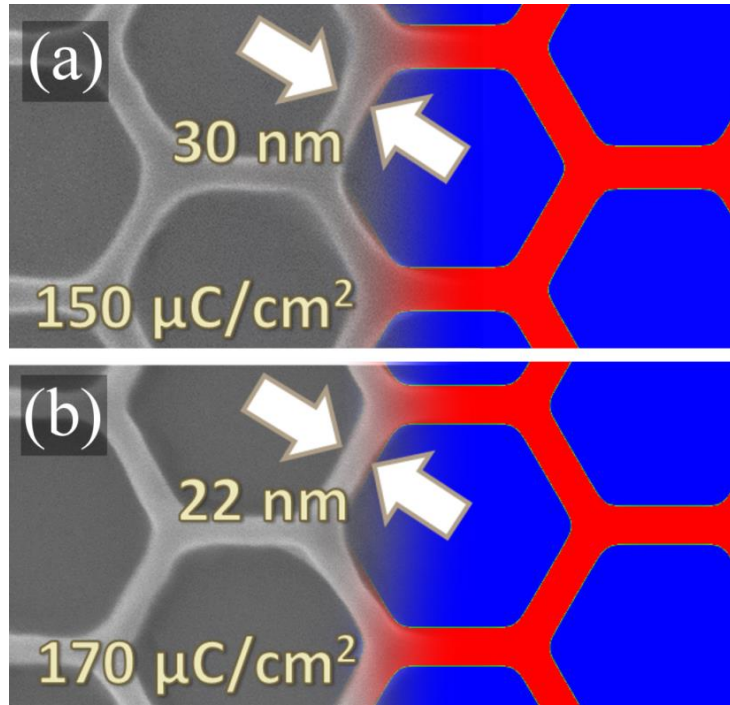


Figure 4.2 - SEM images of PMMA honeycombs as observed (left) and predicted (right) on a silicon substrate with (a) 30 nm PMMA structure widths using a $150 \mu\text{C}/\text{cm}^2$ area dose and (b) 22 nm structure widths using a $170 \mu\text{C}/\text{cm}^2$ area dose with 90 nm thick PMMA resist and developed using a cool, $+12^\circ\text{C}$ IPA:H₂O (7:3) developer for 60 s.

4.1.3. Comparison of Conductive Layers

As mentioned earlier, due to the charge build-up that occurs during EBL exposures on dielectric substrates, conductive layers are needed to allow patterning of features with high resolution. Comparison between such layers, with the assistance of simulation, was done to provide greater insight into the capabilities and advantages of such layers [101]. The conductive layers were placed on top of the resist as their removal prior to development allowed for metal deposited by electron-beam evaporation to enter into patterned regions directly onto the substrate surface. Here, aluminum metal films, which are commonly used for anti-charging in EBL, and a conductive polymer material, aquaSAVE (Mitsubishi Rayon Co.), were compared. The conductive polymer was spun to a consistent thickness according to the recommended parameters. Different aluminum

thicknesses were used to determine the effects on EBL patterning and for comparison with the predicted simulation data.

Exposure and development of 100 nm pitch dots was achieved in PMMA using a range of dot doses from 0 fC/dot to 20 fC/dot over an area of $8.5 \times 100 \mu\text{m}^2$ on multiple samples of silicon and fused silica. Samples were exposed at 30 keV with a 7.5 μm aperture using different conductive layers of aluminum and aquaSAVE conductive polymer with varying conditions. Simulation of the lithography was also done for analysis and interpretation of the results using the EBL simulator. One-hundred nm pitch dots allowed for the most feasible analysis as a large applicable dose window gave a large range of doses prior to feature collapse. Lower pitches, down to 40 nm were fabricated successfully; however, their applicable dose windows were too narrow for thorough analysis.

After exposure, samples coated with aluminum were placed in a TMAH(trimethylanilinium hydroxide)-based etchant, MF-CD-26, that removed the aluminum at a rate of approximately 10 nm/min at room temperature. After removal of the aluminum, samples were rinsed in deionized water and dried prior to development for consistency and to determine the effects of the etchant on the PMMA. Samples using the aquaSAVE conductive polymer were dipped in water for three s and placed directly into the developer without drying. Samples were all developed in IPA:H₂O (7:3) for 20 s then quenched in deionized water prior to drying. The patterns were visualized using a Hitachi S-4800 field emission SEM instrument. Samples were sputter-coated with 3.5 nm of chromium prior to imaging to limit charging. Developed holes in 100 nm PMMA resist can be seen in Figure 4.3 from a side angle of a cleaved silicon substrate with a dot dose of 12 fC/dot showing the profile of the holes from the beam spreading.

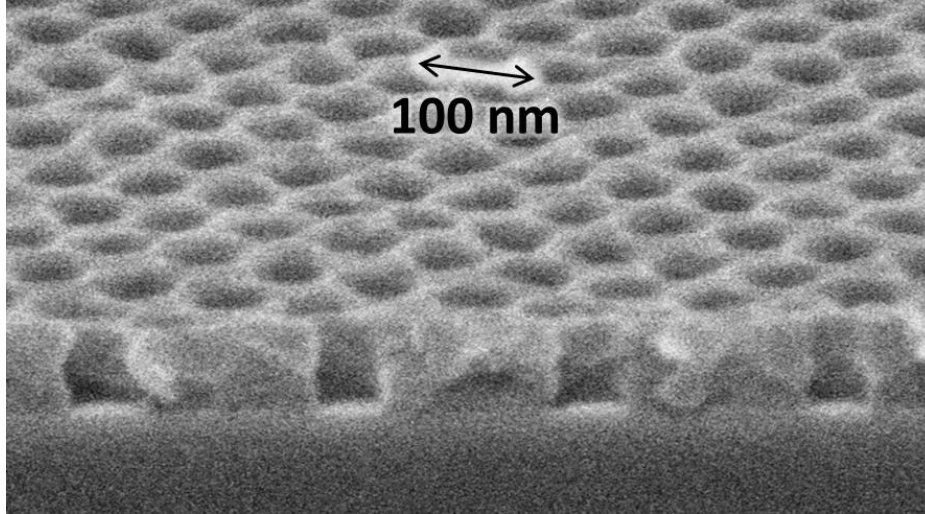


Figure 4.3 - 100 nm pitch developed holes in PMMA resist on a silicon substrate using a co-solvent IPA:H₂O (7:3) developer for 20 s at room temperature with a 12 fC/dot dose with a 30 keV accelerating voltage [74, 101].

To compare different samples, the diameters of the opened holes was measured for various doses using plan-view SEM images. Measurement of the dot diameters in PMMA was done in the center of each array to account for proximity effects from surrounding dots. ImageJ software [133] was used to analyze the images for comparison with the predicted values where average dot diameters were taken from the multiple dots at each dose. Figure 4.4 shows an example of a three-dimensional and cross section simulation which process was used for predicting the width of developed dots in PMMA which allowed for the comparison between experimental and predicted dot sizes.

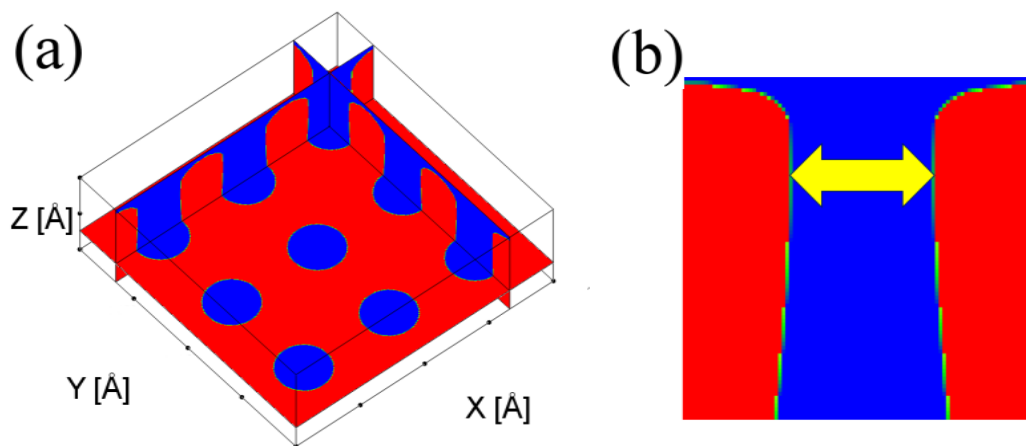


Figure 4.4 – (a) Simulated three dimensional and (b) cross-section development profiles of 100 nm pitch dots in PMMA on a fused silica substrate with aquaSAVE conductive polymer and a 12 fC/dot dose using a 30 keV accelerating voltage with 20 s development in IPA:H₂O (7:3) at room temperature. Measurement of the minimum gap width of features was done using the simulated cross sections. Here, the remaining resist is in red and regions with clearance are shown in blue. The anti-charging layer and substrate are not shown in the simulation. Distances are (a) 3000 Angstroms total width in the X and Y axis and 1000 Angstrom for the Z-axis and (b) 400 Angstrom arrow width.

Figure 4.5 and Figure 4.6 illustrate the variation in the size and quality of features of the dots exposed with the same dose using different anti-charging schemes with different substrates. Overall, the results obtained show that the relative dot size varied the most for cases using aluminum layers. SEM images (a) and (b) from Figure 4.5 compare the dots obtained using aquaSAVE and 10 nm aluminum conductive layers on fused silica substrate. It can be seen that for matching dot doses, the dot diameters varied by about 20 nm. Whereas for silicon substrates, as seen in Figure 4.5 (d, e, f), there was little variation regardless of the inclusion of the conductive layers. The conductive polymer, aquaSAVE, had close consistency with predicted values as seen in Figure 4.7 for fused silica samples, while aluminum layers varied more substantially as seen in Figure 4.8.

Inclusion of thicker, 30 nm aluminum layers, as seen in Figure 4.5 (c), resulted in only slight variations in the dot diameters when used with fused silica substrates. For silicon substrates, however, 30 nm of aluminum resulted in larger than expected dot diameters,

with dots combining together at doses around 13 fC/dot as seen in Figure 4.6. Feature roughness and poor adhesion were seen for all samples with aluminum etching time above 2 min with silicon samples.

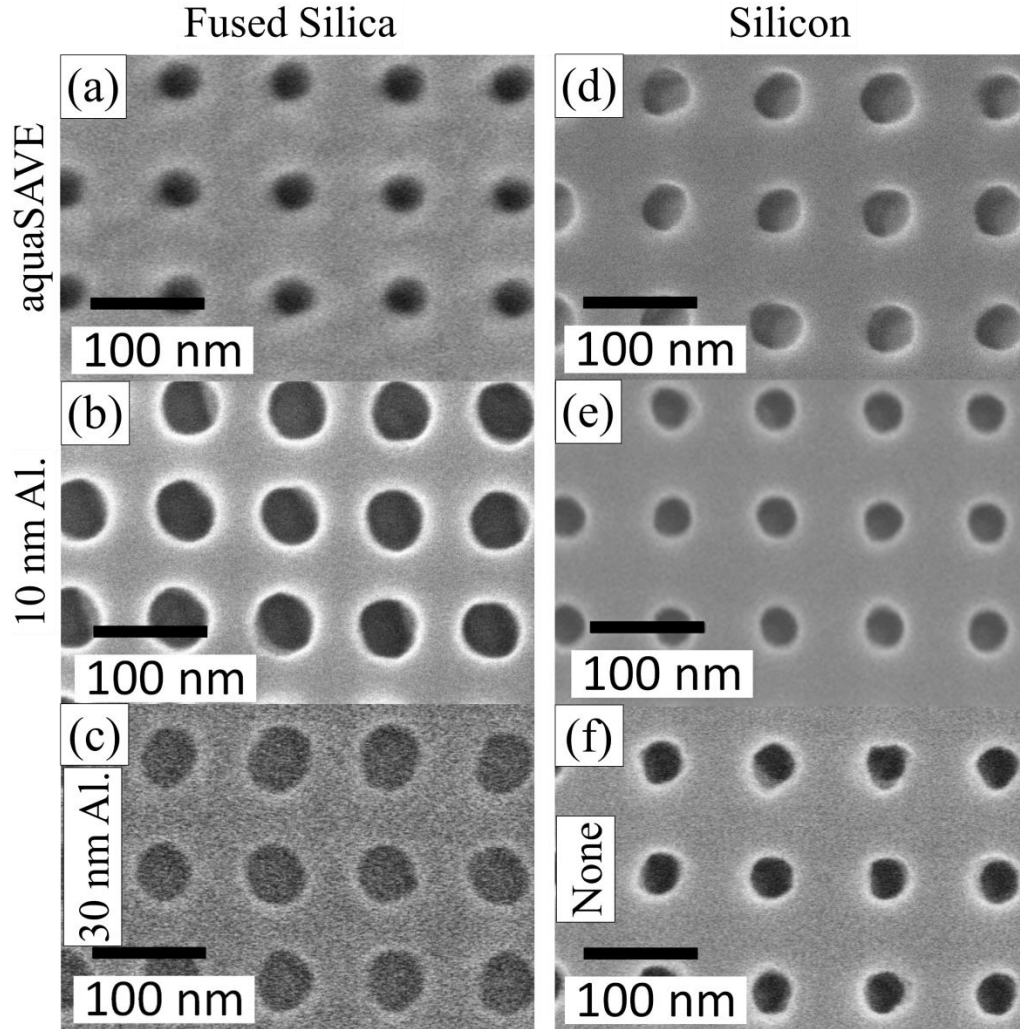


Figure 4.5 - SEM images of 100 nm pitch dots in PMMA with different anti-charging schemes with fused silica samples on the left and silicon samples shown on the right. The left column (a-c) shows fused silica substrates with (a) 70 nm of aquaSAVE conductive polymer, (b) 10 nm of evaporated aluminum conductive layer, and (c) 30 nm of evaporated aluminum conductive layer (stigmation of dots was during imaging and not part of the original pattern). The right column (d-f) shows silicon substrates with (d) 70 nm of aquaSAVE conductive polymer, (e) 10 nm of evaporated aluminum conductive layer, and (f) no conductive layer. All samples were exposed at 30 keV with a 7.5 fC/dot exposure dose and developed for 20 s in IPA:H₂O (7:3) at room temperature with 90-100 nm thick PMMA.

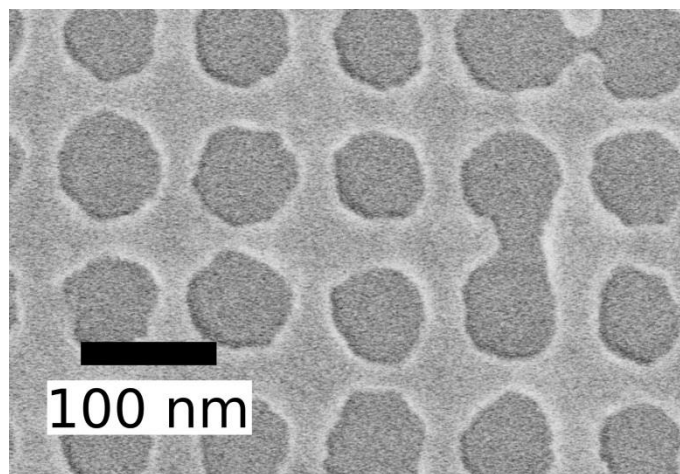


Figure 4.6 – SEM image of 100 nm pitch dots in ~100 nm thick PMMA using a 7.5 fC/dot exposure dose on a silicon substrate with 30 nm of aluminum used for measurement of the effects of using the thick layer. Resist roughness and poor adhesion were seen for all silicon samples exposed to the aluminum etchant for longer than 3 min, with and without aluminum.

Comparison of predicted and experimental 100 nm pitch dots in PMMA obtained using aquaSAVE conductive layers on both silicon and fused silica samples as seen in Figure 4.7 shows that there is a very close agreement. Although comparable to the thickness of the PMMA, the 70 nm aquaSAVE conductive layer did not have a significant effect on resolution of features. Effective charge dissipation using the conductive polymer can also be concluded as the average dot diameters were very close regardless of the substrate material. These results suggest that charge-build up and beam broadening due to the conductive polymer were both unsubstantial, with limited beam broadening correlating with the low density and average atomic number of the conductive polymer.

Comparable dose requirements allows for the translation of process conditions using fused silica substrates compared to silicon when using the conductive polymer. The delicate removal process in deionized water is also beneficial for processing, as it has no noticeable impact to the resist layer, showing an additional benefit of aquaSAVE.

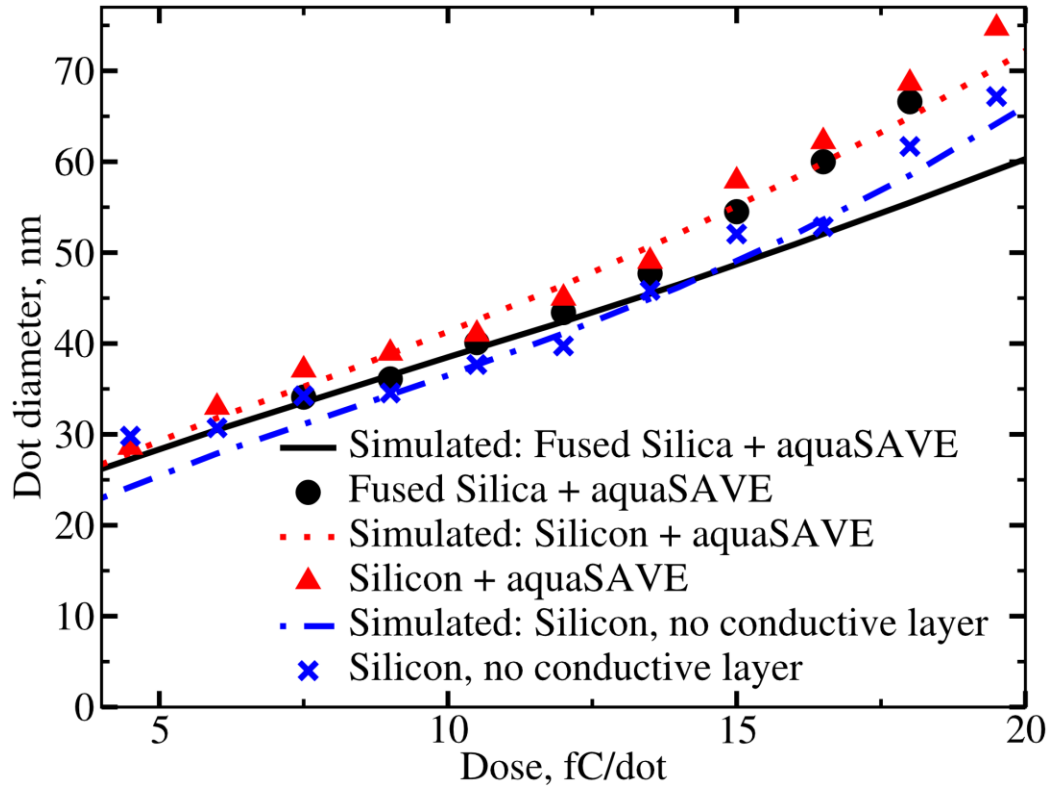


Figure 4.7 - Comparison between simulation and experimental 100 nm pitch dots in PMMA on fused silica and silicon samples with aquaSAVE conductive polymer and silicon with no conductive layers using a 30 keV accelerating voltage with 20 s development in IPA:H₂O (7:3) at room temperature. Standard deviation was within 3 nm for each sample.

Work involving aluminum conductive layers was more complicated as a number of factors were found to affect the quality of EBL exposed patterns in this case. Thin metal films have traditionally been used as one of the methods to mitigate the effects of charge-build up during EBL exposure largely due to the availability and cost of this method [134]. Comparison of measured and predicted dot diameters, displayed in Figure 4.8, shows the discrepancy with experimental results as features were seen to be larger than predicted. As seen in Figure 4.9, high quality narrow dots with 100 nm pitch spacing were successfully fabricated using aluminum on a fused silica substrate, however, a narrow dose window was observed. Such as a significant increase in the dot

diameters was not seen on the silicon substrates however, as the dot diameters between samples with and without 10 nm of aluminum showed little variation.

The contrast between fused silica and silicon substrates suggests that the 10 nm aluminum layer does not completely eliminate the effects of charging during the EBL process. It is generally known that conductivity sharply diminishes for metal film thicknesses below 20–30 nm. This has been attributed to a number of factors, but predominantly to the non-uniform nucleation of deposited films [135, 136].

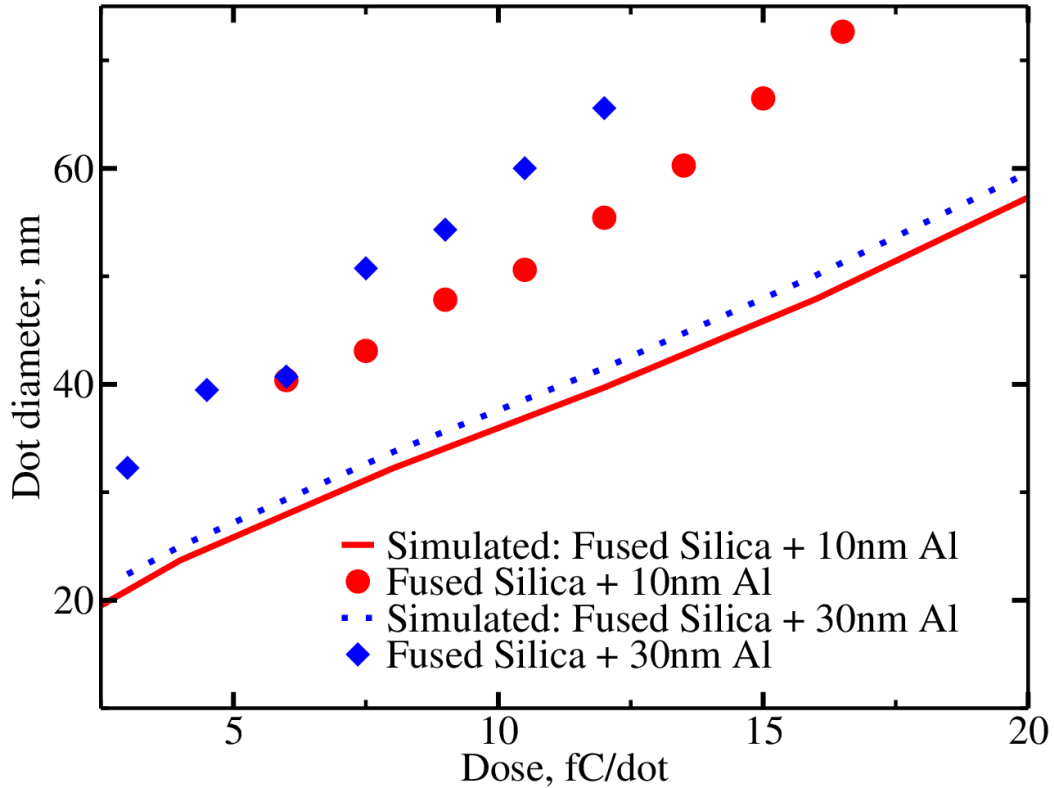


Figure 4.8 - Comparison of dot sizes for 100 nm pitch dot arrays in 100 nm thick PMMA for a range of exposure doses on fused silica, using a 30 keV accelerating voltage and 20 s development in IPA:H₂O (7:3). Lines correspond to simulated results and symbols correspond to experimental data. Standard deviation was within 3 nm for each sample.

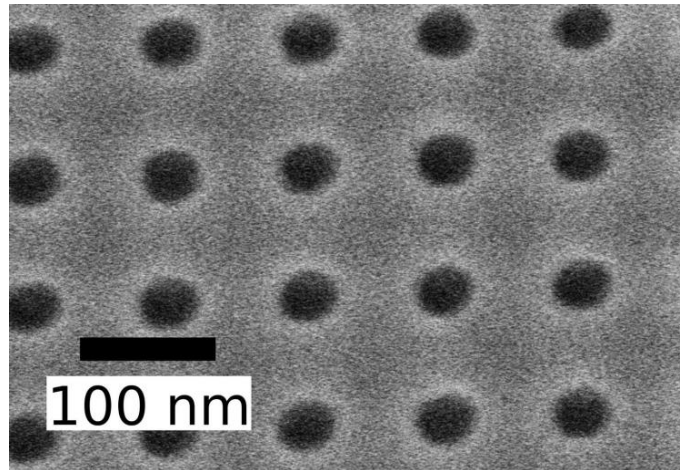


Figure 4.9 - SEM image 100 nm pitch dots in PMMA resist on a fused silica substrate using a 10 nm evaporated aluminum film as a conductive layer exposed at 30 keV with a 6 fC/dot dose and developed for 20 s in IPA:H₂O (7:3) at room temperature.

However, the described charge buildup arguments do not explain the observed difference of measured and predicted dot diameters employing 30 nm thick aluminum layers. SEM imaging of 20 nm and 30 nm aluminum films on PMMA on fused silica substrates confirmed increased charge build-up for thinner aluminum films and minimal charging for 30 nm thicknesses (see Figures 4.11 and 4.12). Elsewhere the effects of the aluminum etchant on PMMA causing poor adhesion have been reported [137]. To investigate the influence of the aluminum etchant on the observed morphology, samples of PMMA on silicon with no aluminum layers were treated by the etchant for different durations before EBL processing. Etching of samples for 30 sec. showed no effect on the development of the holes. As seen in Figure 4.10, these samples produced similar results to other samples with accurately predicted dot diameters. Longer etch times of 3 min, however, created significantly larger dot sizes and a narrow dose range before collapse between dots occurred for dot doses above 9 fC/dot.

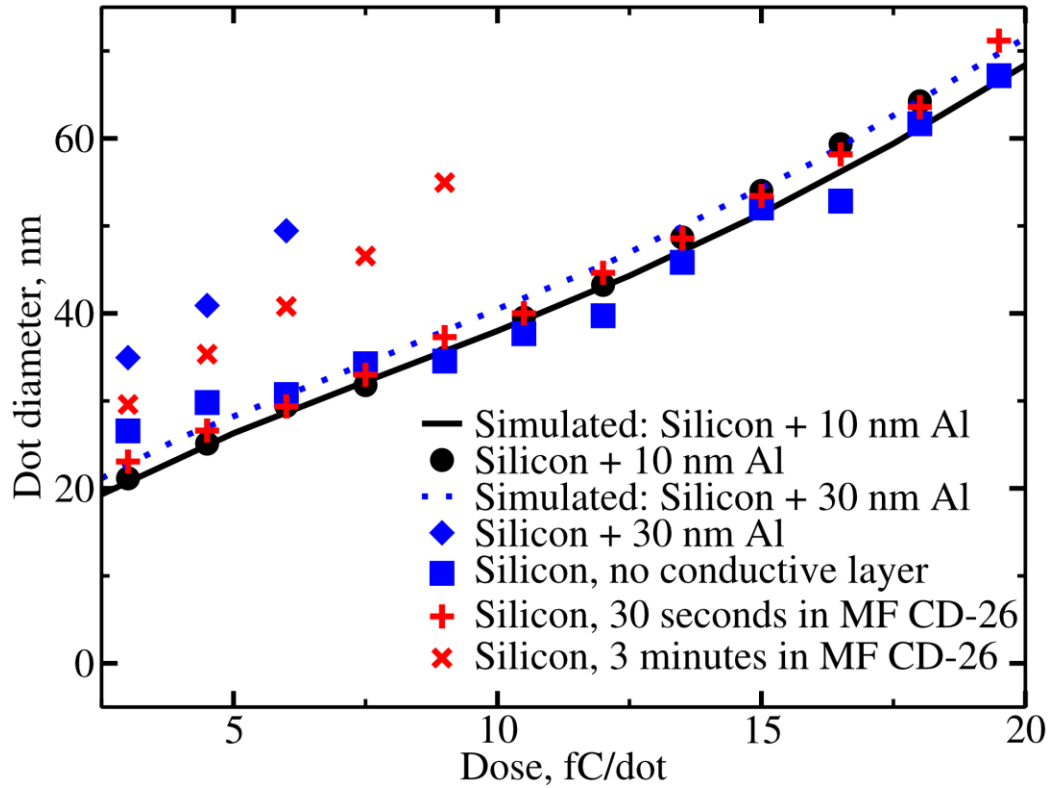


Figure 4.10 - Comparison of dot sizes for 100 nm pitch dot arrays in 100 nm thick PMMA for a range of exposure doses on silicon, using a 30 keV accelerating voltage and 100 nm pitch dots with a 20 s development in IPA:H₂O (7:3). Lines correspond to simulated results and symbols correspond to experimental data. Results marked with an x represent a silicon sample with no aluminum layer and developed after being placed in the aluminum etchant MF CD-26 for 3 min. Standard deviation was within 3 nm for each sample.

As seen in Figure 4.10, comparison between samples with 30 nm of aluminum and samples without aluminum on silicon, using three-minute etch times, showed comparable dot diameters indicating that PMMA resist performance is significantly altered by the aluminum etchant. Despite the thickness of the aluminum layer, it seems to provide limited protection to the resist from the aluminum etchant. The effects of using prolonged etching of the aluminum verify that not only adhesion to the silicon substrate is affected, but also the resolution and quality of the patterning [137].

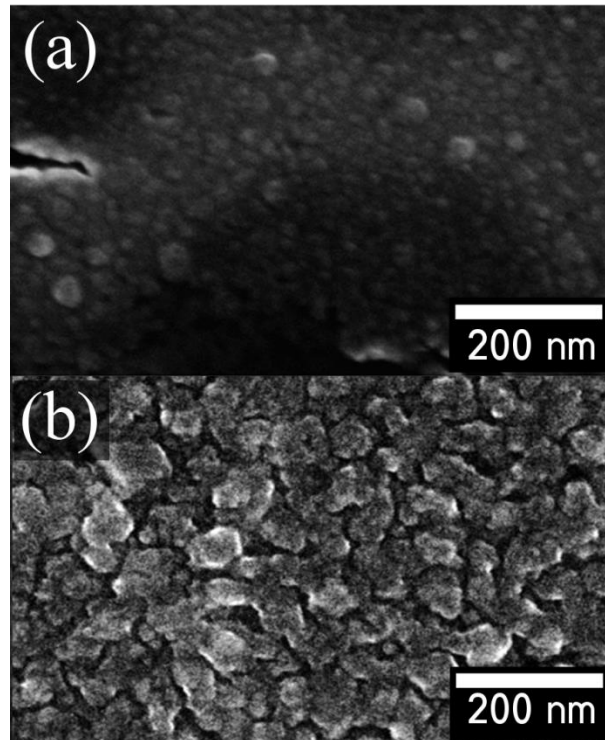


Figure 4.11 – SEM images demonstrating the variation in grain size and charge build up between (a) 20 nm of aluminum on PMMA on a fused silica substrate and (b) 30 nm of aluminum on PMMA on a fused silica substrate. 20 nm aluminum films experienced significant charge-build up when imaged at 10 keV and with a 5.9 mm working distance.

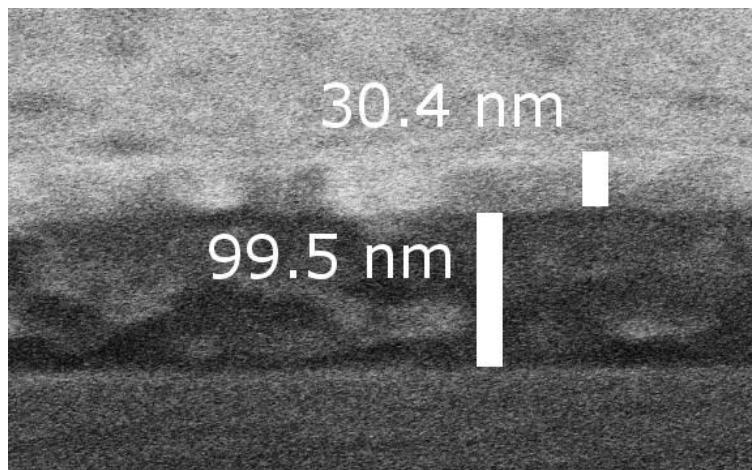


Figure 4.12 – Cross section image of 100 nm thick PMMA on a silicon substrate with a 30 nm top coating of aluminum showing a continuous film. Charge-build up during SEM imaging of 30 nm films whereas 20 nm and thinner aluminum films on fused silica substrates did experience charging.

4.1.4. Summary of EBL fabricated devices

Significant control over substrate patterning was obtained with variations in exposure dose, development temperature and time, including extensive studies done comparing the effectiveness of conductive layers which were needed for EBL exposures on fused silica substrates. The conductive polymer, aquaSAVE, provided exceptional process latitude which allowed for comparable processing conditions for both silicon and fused silica substrates. Aluminum, although capable of providing quality dots, was limited in processing latitude with difficulties arising from both charge-build up during exposure and prolonged etch times of the aluminum layer on silicon. Further, demonstration of an increased process exposure dose latitude using cold development allowed for increased consistency in SERS substrate fabrication, which is advantageous for consistency in SERS biosensing.

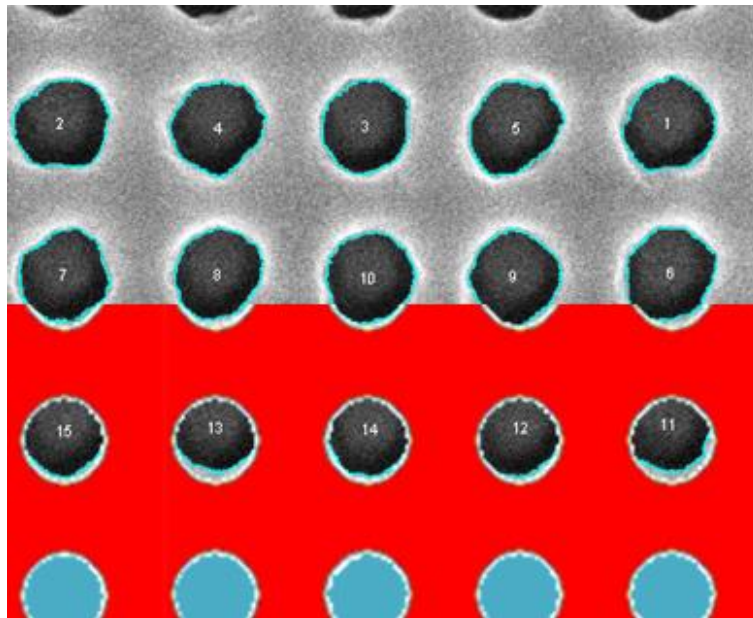


Figure 4.13 - Overlap of predicted and simulated dot diameters using the EBL Simulator tool for prediction of dot diameters and gaps needed for subsequent evaporation and lift-off. This sample was with a fused silica substrate and aquaSAVE conductive polymer at 30 keV accelerating voltage with 100 nm pitch.

4.2. Nanoimprinted SERS Substrates

Nanoimprint lithography (NIL) offers both high-resolution fabrication, and the potential for high throughput fabrication of devices at low costs compared to EBL. Despite the simplicity of NIL, its onset compared to EBL was much later, and hence, new methods and aspects of NIL will continue to develop as it has quickly been shown to be an effective method for mass fabrication of micro- and nano-devices. Due to the need for low-cost, highly reproducible substrates for SERS, NIL offers many possible advantages not available in other methods. The initial costs for NIL mold fabrication is relatively high when using EBL, however batch processing has the potential to significantly reduce cost for plasmonic biosensors. Here NIL substrates were fabricated to demonstrate the feasibility of this technology for control over nanoscale features for different SERS devices. Demonstration of a thermal NIL was done on samples of both silicon and fused silica for comparison and for ease of processing when using the silicon substrates. Although ultraviolet imprinting was possible, a thermal imprinting process was done for simplicity and greater control over the resist thickness, which needed to be precise for accurate etching.

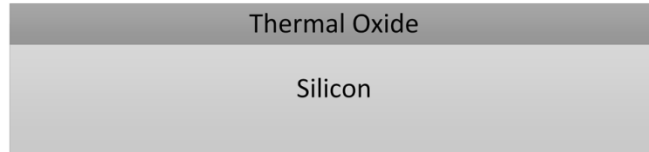
4.2.1. NIL Mold Fabrication

One of the critical aspects of fabricating NIL SERS substrates was the production of a master mold containing the desired features to transfer. Metrics such as feature resolution, geometry, and pitch needed to be incorporated on the mold. A 10 cm silicon prime polished wafer was cleaned in a piranha (7:3 $\text{H}_2\text{SO}_4\text{:H}_2\text{O}_2$) solution for 20 min and rinsed in deionized water, then dried with nitrogen. A thermal silicon oxide layer was thermally grown (wet oxidation) to ~63 nm using the Minibrute furnace in the NanoFab at 900 °C and the thickness verified using a filmetrics, an optical thin film measurement tool. Samples were then diced into 1 cm x 1 cm pieces for ease of

processing. The samples were then cleaned again in piranha, spun with 90 nm of 950K PMMA, and baked at 180 °C prior to application of an aquaSAVE conductive polymer layer which was found to help with consistency and resolution in EBL exposures due to the presence of the dielectric oxide layer. EBL patterns with various dot arrays of varying pitch, and other geometries were patterned in the resist similar to those done for EBL fabricated SERS devices. Proper spacing of up to 50 μm between different arrays was done to prevent proximity effects that can occur in both EBL and NIL. In NIL, neighboring features can cause resist to be displaced and result in variations in the resist thickness across the wafer.

Development of EBL-patterned molds was done using either 20 s in IPA:H₂O (7:3) at room temperature with a water rinse for 40 s with the same developer at 12 °C using a cold plate without drying. After development, 10 nm of chromium was deposited using electron beam evaporation which was needed as an etch mask. After evaporation, lift-off was performed by soaking the samples in acetone for approximately 10-20 min prior to sonication of the samples without drying. The pre-soak was found to assist in the lift-off process as the small grain size of chromium made lift-off more difficult compared to using other metals such as copper, silver or gold. Samples were then rinsed in IPA and water, then dried in nitrogen after lift-off. Figure 4.14 gives a schematic overview of the mold fabrication process.

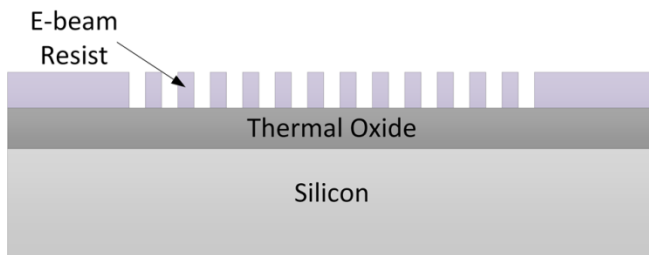
1. Thermal Oxide



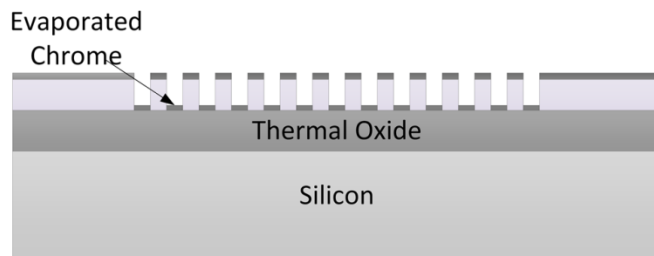
2. E-beam resist and exposure



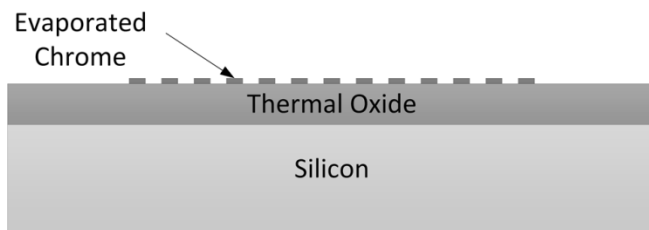
3. Cold development



4. E-beam evaporation



4. Lift-off



5. ICP Etch

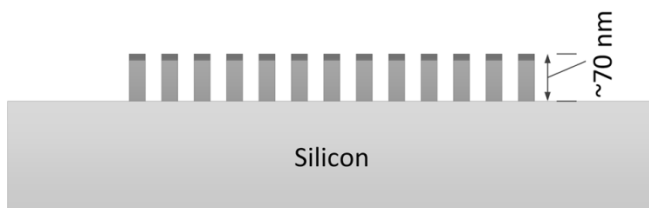


Figure 4.14 - Nanoimprint lithography process flow for mold fabrication. Silicon substrates underwent a thermal oxidation to provide the pillar material as silicon dioxide is known to be less brittle than silicon, allowing for improved lifetime after multiple nanoimprints.

4.2.2. Mold Etching

After performing lift-off, a chrome masking layer on top of the thermal oxide layer remained. An inductively coupled reactive ion etch (ICP-RIE) Oxford Instruments PlasmaLab system was used to etch into the oxide layer creating the structures of the nanoimprinted molds. Etching was done using a C_4F_8 /helium etch recipe at 20 °C using a base pressure of 4 Pa, a 25 sccm flow rate, and a forward power of 150 W were found to be ideal for an etch rate of approximately 2 nm/sec. The underlying silicon layer acted as an etch stop which could be seen in Figures 4.15 and 4.16.

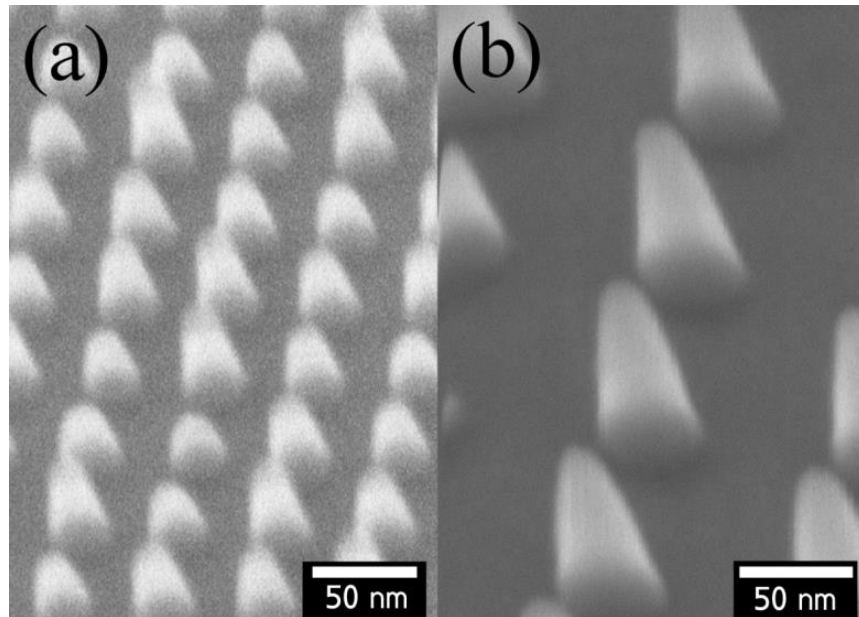


Figure 4.15 – SEM images of thermally grown silicon dioxide pillars on a base silicon substrate with 10 nm of chrome for (a) 50 nm pitch and (b) 100 nm pitch arrays. Etch time for these samples was 20 s using a C_4F_8 /helium . Images were taken at a 30° angle.

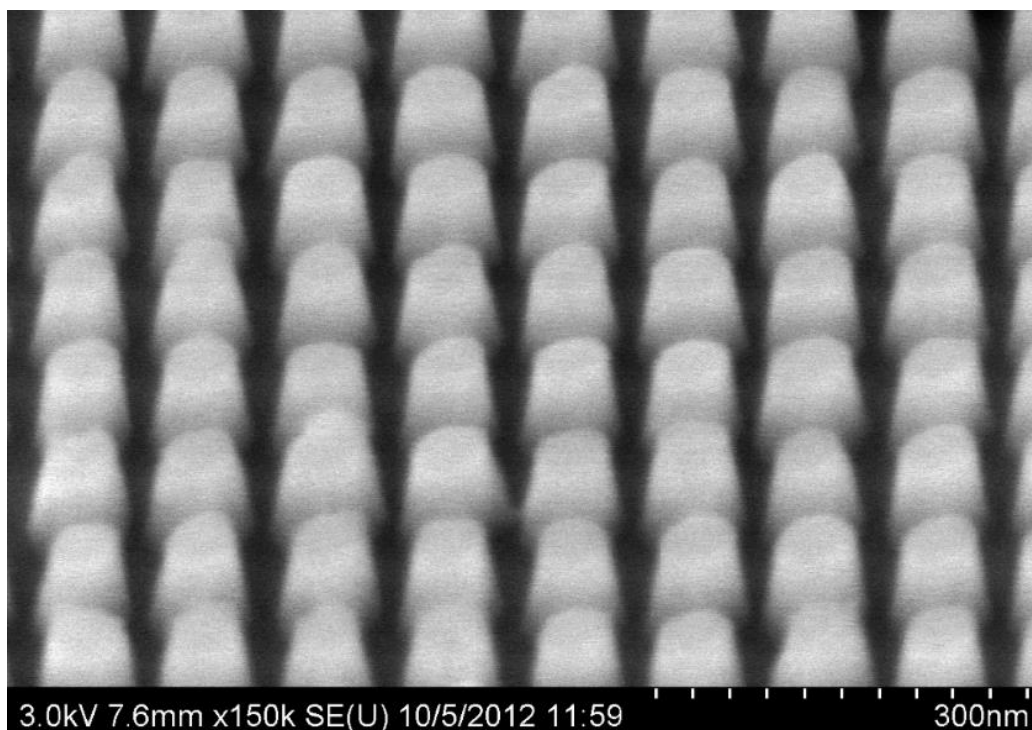


Figure 4.16 – SEM image of 100 nm pitch thermally grown silicon dioxide pillars with 10 nm chromium caps of a NIL mold and narrow gaps. Etching parameters allowed for improved feature dimensions and more vertical sides to assist in lift-off. Images were taken at a 30° angle.

4.2.3. Anti-adhesion Coating

An anti-adhesion layer was applied using a self-assembled monolayer (SAM) of trichloro (1H,1H,2H,2H-perfluorooctyl)-silane on the nanoimprint molds (see Figure 4.17) [138]. This was done by placing the substrates in a vacuum for two hours with a few drops of the silane in a beaker to eventually evaporate and form a SAM on the surface of the silicon. Such SAM on silicon are known to be resistant to many acids and alkali solutions, but can be easily removed with oxygen plasma [139]. It was found that the adhesion layer on the mold was effective as up to 10 runs could be performed before requiring cleaning and re-application of the adhesion layer. Samples with the nanoimprint resist were also found to benefit with the same process, although the exact mechanism of attachment to the surface of the resist is uncertain. Contact angle

measurements before and after application of the anti-adhesion layer on both the molds and samples with the nanoimprint resist showed increased hydrophobicity due to the anti-adhesion layer (see Figures 4.18 and 4.19).

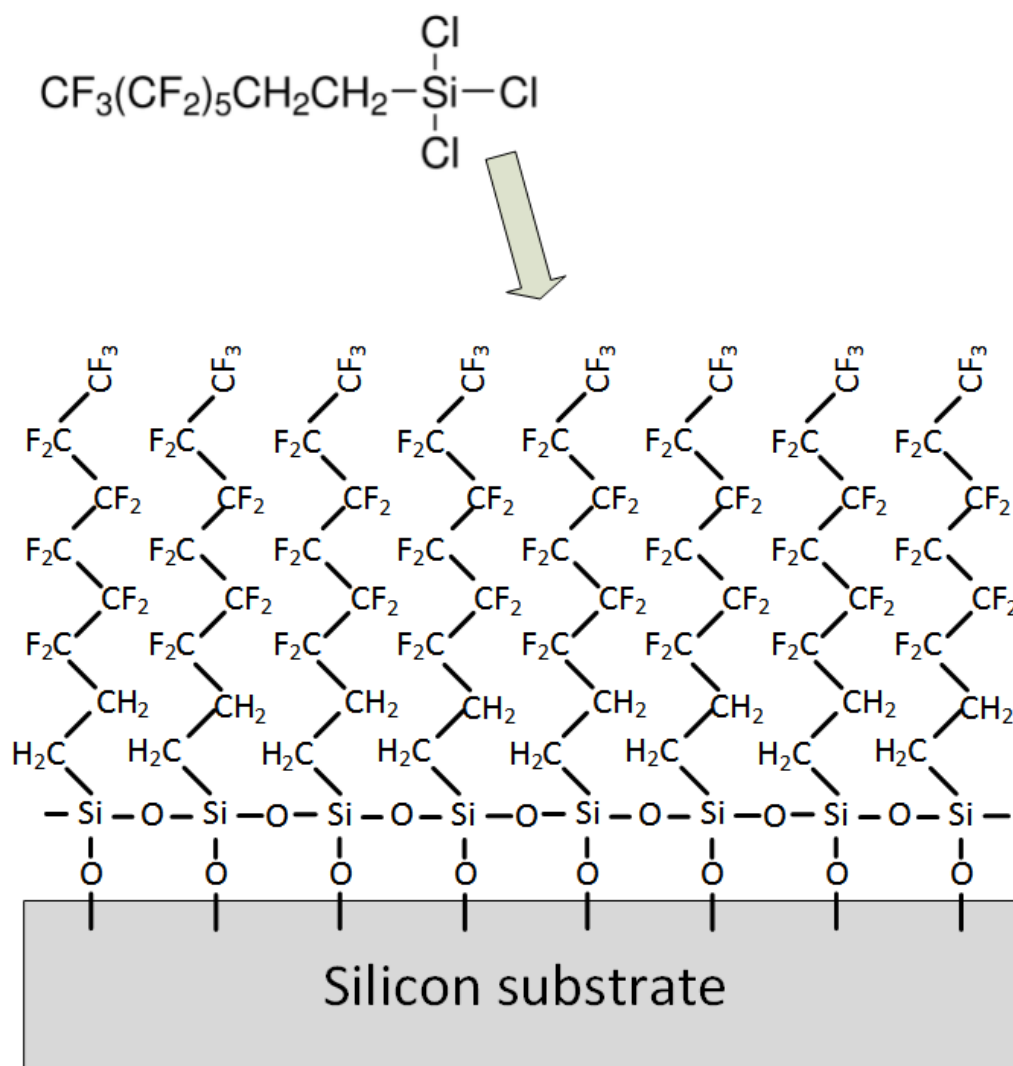


Figure 4.17 - Self-assembled monolayer of trichloro(1H,1H,2H,2H-perfluorooctyl)silane (perfluorodecyltrichlorosilane) which binds to the native oxide layer on silicon. Tests also confirmed that the silane bound the surface of the nanoimprint resist (see Figures 4.18 and 4.19).

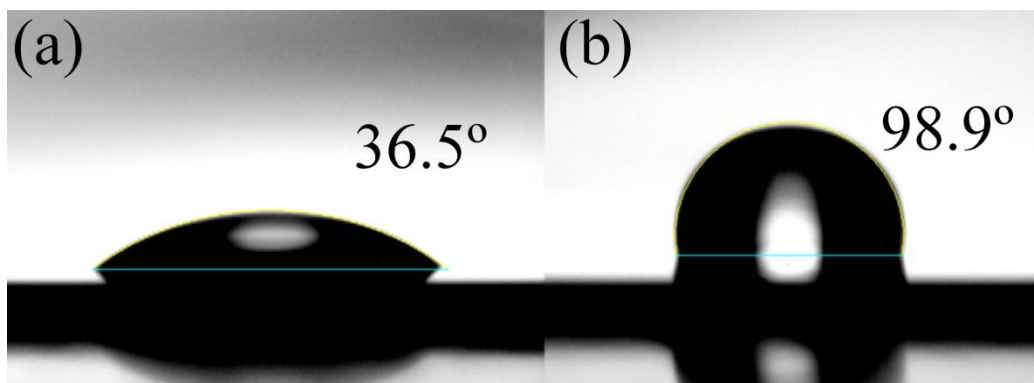


Figure 4.18 - Comparison of contact angle measurements on silicon mold material (a) before, and (b) after application of SAM anti-adhesion layer of trichloro (1H,1H,2H,2H-perfluorooctyl)-silane.

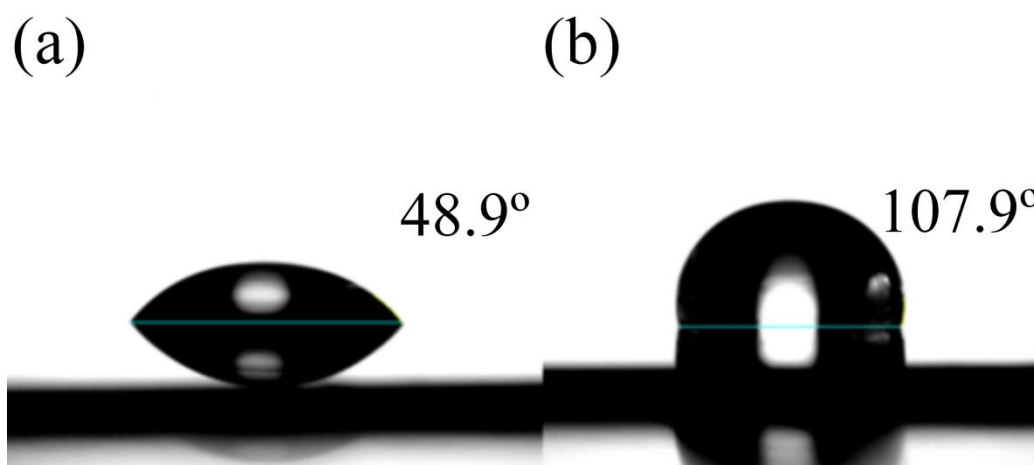


Figure 4.19 - Comparison of contact angle measurements on NXR-1025 NIL resist (a) before and (b) after application of SAM anti-adhesion layer of trichloro (1H,1H,2H,2H-perfluorooctyl)-silane.

4.2.4. Nanoimprint Resist Properties

Thermal imprints were done with both NXR-1025 and 950K PMMA resists. However, NXR-1025 was used for the majority of experiments as it gave better results and consistency compared to PMMA due to the lower pressure and temperature needed for imprinting due to its glass transition temperature of around 60 °C as opposed to the value for PMMA 950K which is between 95 °C and 106 °C [79, 140]. Imprints using PMMA also resulted in damaged molds, likely due to the increased pressure needed for

imprinting. NXR-1025 was thinned in 1-methoxy-2-propyl acetate to achieve ~90 nm resist thicknesses spun at 3000 RPM/sec with a two-s ramp then baked at 160 °C for three min. One advantage of using a thermal resist for lift-off is that only a single layer of resist is required, and the procedure can be performed on both silicon and fused silica or transparent samples with a silicon mold [79].

4.2.5. Nanoimprint Process

Prior to alignment of the mold and sample, the edge bead on the corners and edges of the sample that occurred from spinning the nanoimprint resist was removed. This was done by using the corner of a folded cleanroom wipe that was soaked in acetone and allowed to evaporate until it was slightly damp. If too much acetone remained on the wipe, the acetone would wick into the center of the substrate deforming the resist where the features were to be transferred. It was found that if the edge bead wasn't completely removed, air bubbles would get trapped between the mold and sample, causing inconsistent imprints. After the samples were prepared for the imprint, the mold was placed on top of the sample over the thermocouple (see Figure 4.20

Clearance after imprinting to remove resist from imprinted openings where metal could be deposited was performed using an inductively coupled plasma – reactive ion etching (ICP-RIE) process to achieve anisotropic etching of the resist which was needed to allow lift-off of the resist. Variations with oxygen and helium concentrations were tested as helium allowed for a sufficient pressure while limiting etch rates. Successful processing was done for 100 nm pitch regions consistently after adjusting the etch process to a low power etch for 16 s (see Figures 4.13–4.15).

). The recipe used for the imprint involved a 5 minute chamber pump down, followed by a pre-imprint at 110 °C with a pressure placed on the mold and sample of 620 kPa followed by the imprint process where the sample and mold were heated to 130 °C with

a pressure of 1450 kPa for 30 s. After the imprint, the chamber was slowly vented at a temperature of 50 °C. To improve the separation between the mold and sample, the chips were frozen using liquid nitrogen cooling and then allowed to return to room temperature. The sample, which was made to be slightly larger than the mold, was fastened and high-pressured air was blown between the sample and mold while separation was done using a scalpel.

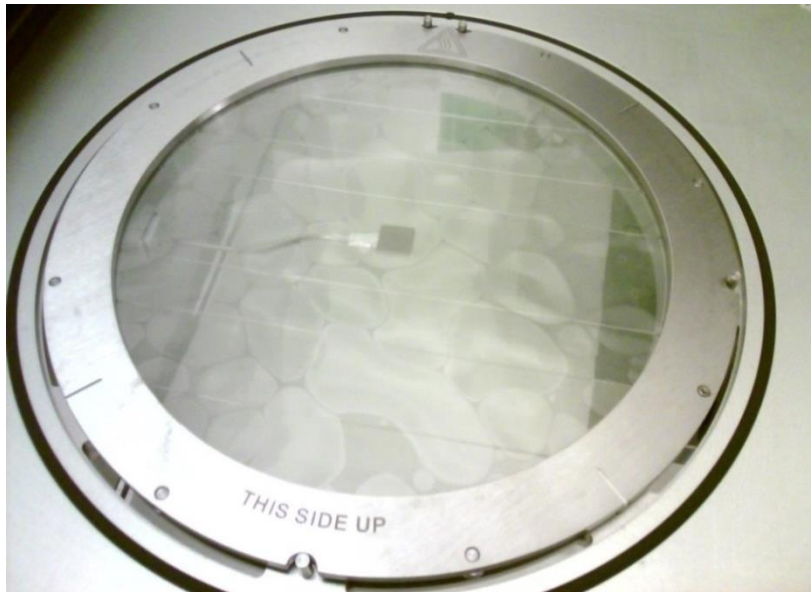


Figure 4.20 - Placement of mold on top of sample after a nanoimprint run. The sample and mold are placed between two sheets of transparent film, which allows a uniform pressure. Temperature was measured on the sample using a thermocouple as seen in the center of the image. After the imprint, a small bubble around the substrates as well in other regions between the films remained.

Silicon samples used to allow ease of inspection and processing in NIL, with results transferred to fused silica samples after the process had been developed. Variations in feature sizes, such as periodic dot arrays of different pitches could be seen optically, as in Figure 4.21, which shows darker shaded regions corresponding to dots with narrow inter-dot gap distances, corresponding to the mold's structures. Imprints on samples with silicon appeared to generally give better yields compared to samples of fused

silica. No exact measurements of the yield were conducted; however, the mismatch in both thermal conductivity and expansion compared to the silicon mold may be one of the causes for different yields. Further, when imprinting fused silica samples, it was found that resist contamination occurred more readily. For 1 cm samples, the expansion at 130 °C of silicon is 260 nm across the substrate whereas fused silica only changes by 55 nm across the wafer, a difference of approximately 200 nm (see Table 1). Although across the patterned region of 300 μm , this only accounts for about a 30 nm difference, which did not seem to have any major effect on the feature transfer. Figure 4.22 shows a schematic overview of the thermal nanoimprint process used in this work.

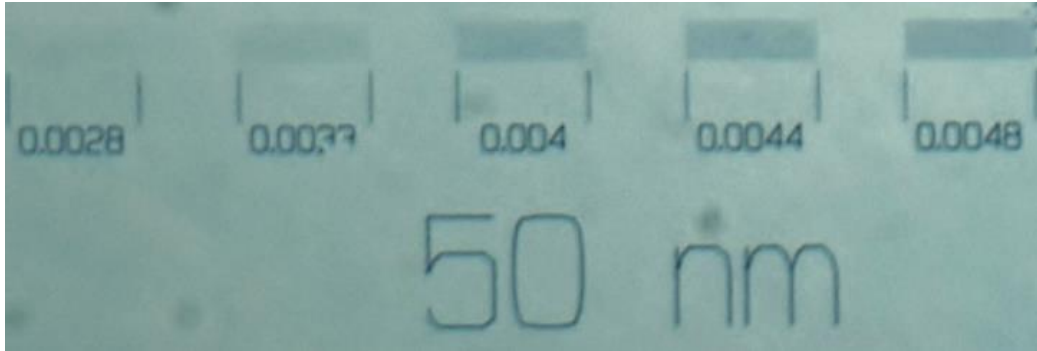


Figure 4.21 - (Flipped) optical image of nanoimprinted 50 nm pitch regions on a transparent fused silica substrate. The darker shaded boxes correspond to larger dot diameters transferred from the master mold. The values here are the dose factors used which were multiplied by 0.6 fC/dot.

Table 1 - Thermal Conductivity and Expansion of Bulk Silicon and Fused Silica.

| Material | Thermal conductivity | Thermal expansion, linear |
|--|---|--|
| Silicon [141] | $130 \text{ W/m}^{-1} \text{ }^{\circ}\text{C}^{-1}$ | $2.6 \cdot 10^{-6} \text{ }^{\circ}\text{C}^{-1}$ |
| Thermally grown silicon dioxide [142, 143] | $1.4 \text{ W/m}^{-1} \text{ }^{\circ}\text{C}^{-1}$ | $0.24 \cdot 10^{-6} \text{ }^{\circ}\text{C}^{-1}$ |
| Fused silica [144] | $1.38 \text{ W/m}^{-1} \text{ }^{\circ}\text{C}^{-1}$ | $0.55 \cdot 10^{-6} \text{ }^{\circ}\text{C}^{-1}$ |

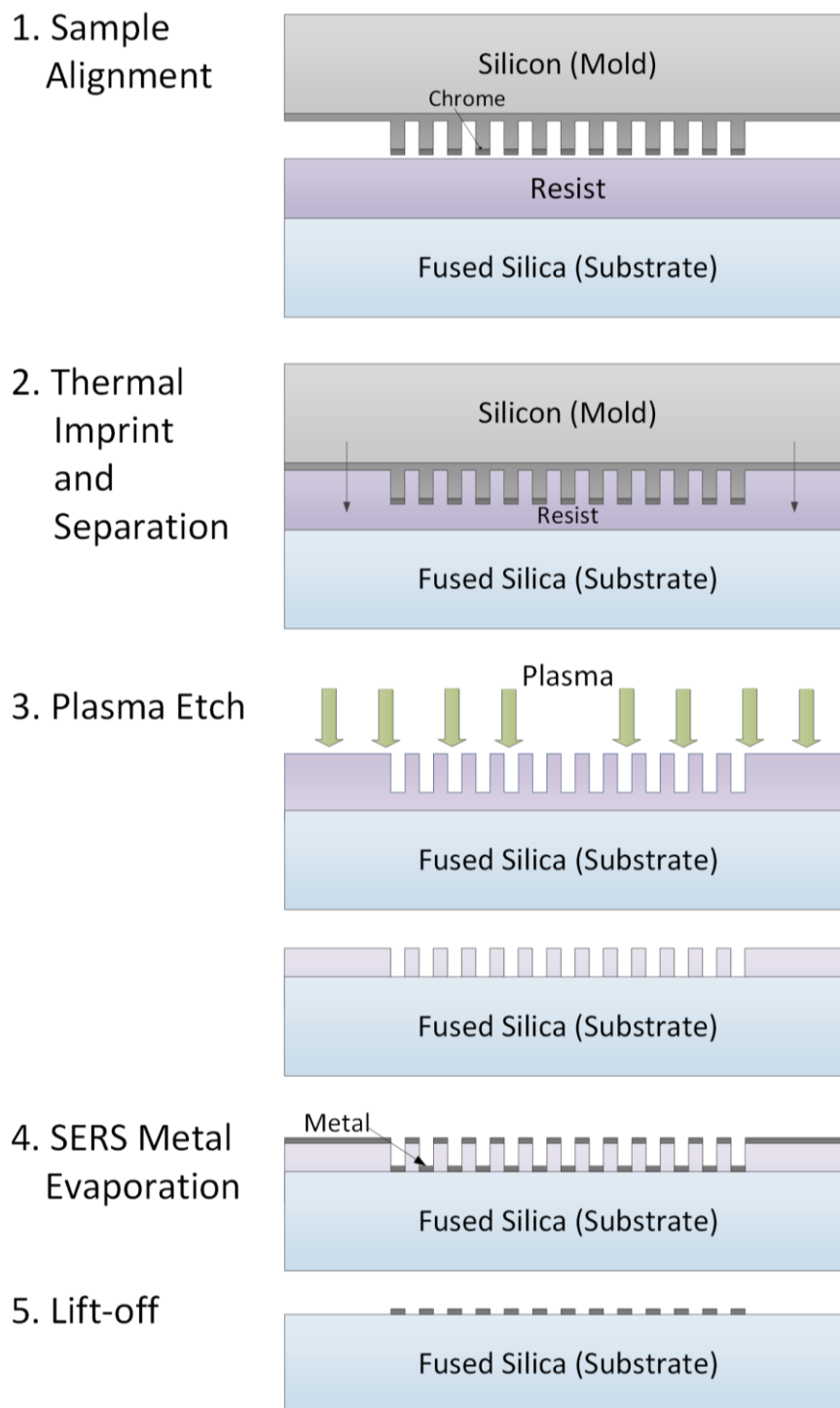


Figure 4.22 - Thermal nanoimprint process used for fabrication of SERS substrates including (1) sample alignment; (2) thermal imprinting and separation process; (3) oxygen plasma; (4) metal evaporation (e.g. copper, gold, silver); and (5) resist lift-off.

Clearance after imprinting to remove resist from imprinted openings where metal could be deposited was performed using an inductively coupled plasma – reactive ion etching (ICP-RIE) process to achieve anisotropic etching of the resist which was needed to allow lift-off of the resist. Variations with oxygen and helium concentrations were tested as helium allowed for a sufficient pressure while limiting etch rates. Successful processing was done for 100 nm pitch regions consistently after adjusting the etch process to a low power etch for 16 s (see Figures 4.13–4.15).

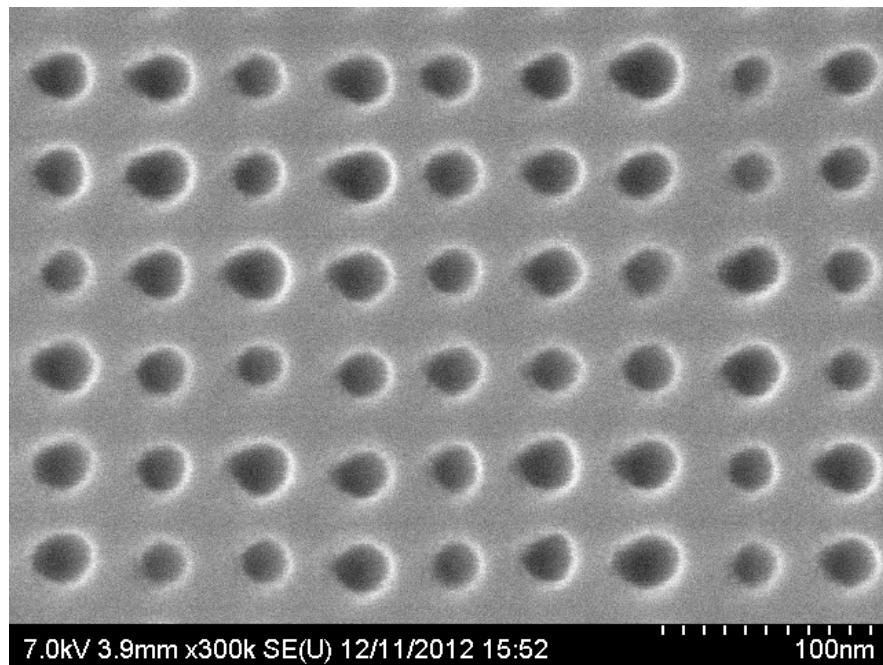


Figure 4.23 - 50 nm pitch dots imprinted in ~85 nm thick NXR-1025 thermal nanoimprint resist using a 1 cm x 1 cm mold and fused silica substrate after an etch process. Minimum gap size between dots was approximately 20 nm.

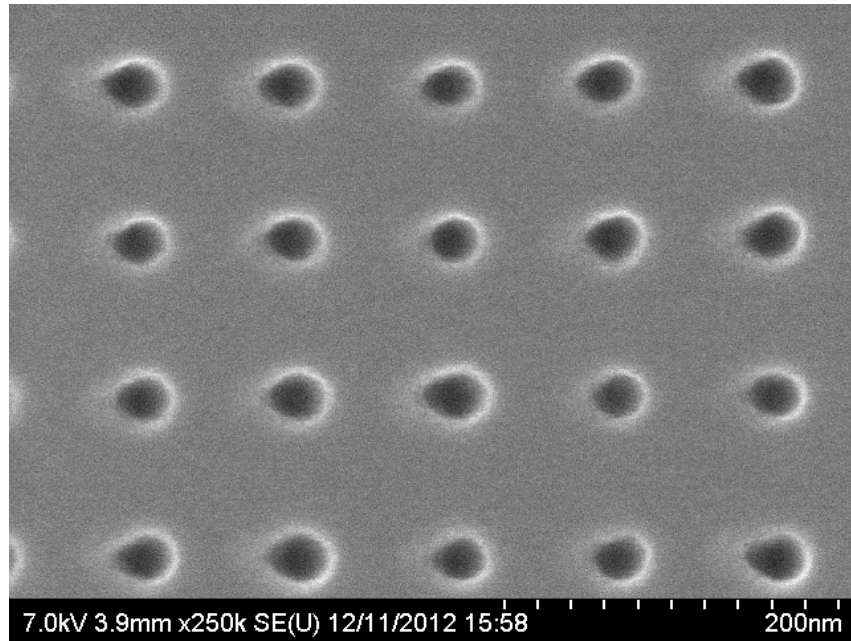


Figure 4.24 - 100 nm pitch dots imprinted in ~85 nm thick NXR-1025 thermal nanoimprint resist using a 1 cm x 1 cm mold and fused silica substrate with ~20 nm diameter features.

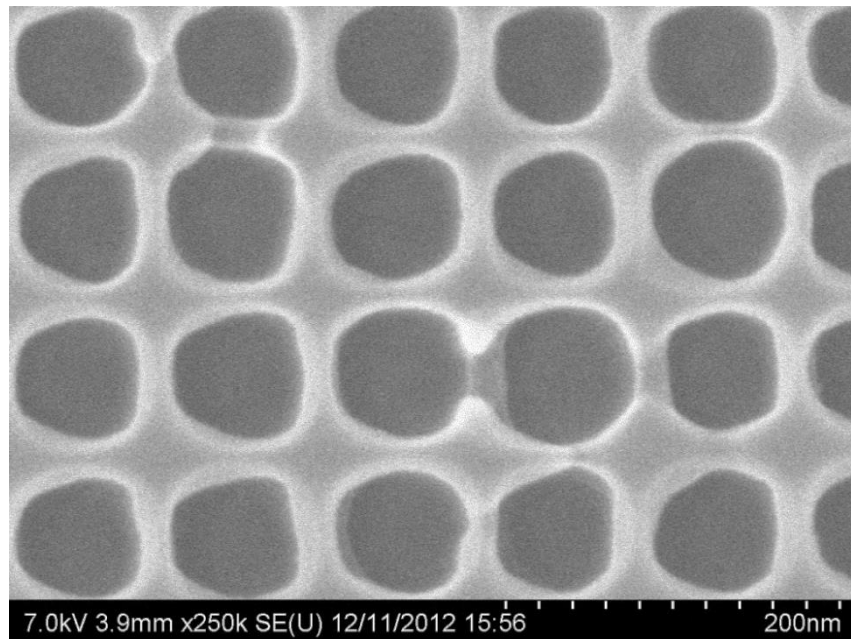


Figure 4.25 - 100 nm pitch dots imprinted in ~85 nm thick NXR-1025 thermal nanoimprint resist using a 1 cm x 1 cm mold and fused silica substrate with an ~20 nm gap distance between opened holes. An etch process was done on this sample to gain clearance in opened dots for subsequent lift-off.

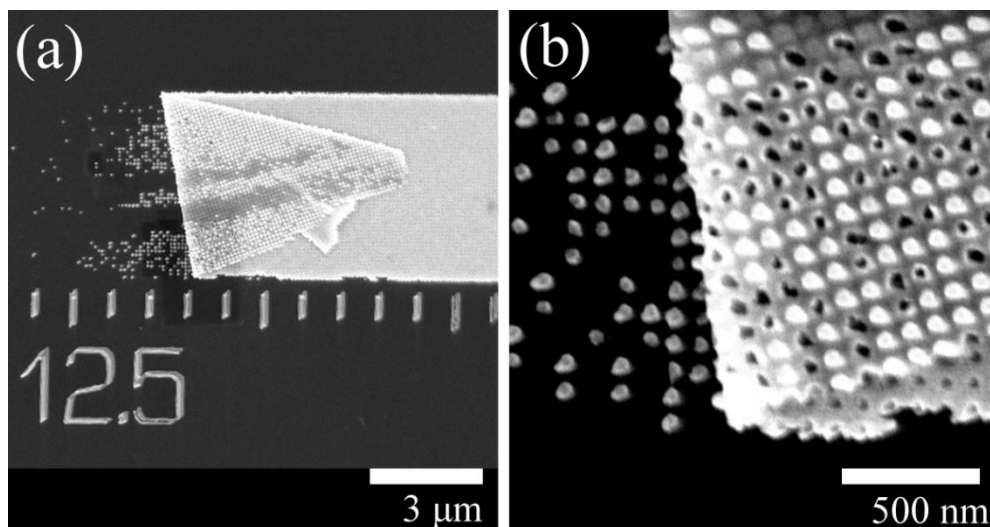


Figure 4.26 – SEM image showing insufficient clearance after the etching process resulted in partial yield of dots during lift-off. Here, gold was evaporated on a fused silica substrate using electron beam evaporation to a metal thickness of ~10 nm.

Insufficient clearance of the pattern regions and isotropic etching resulted in metal features being removed during the lift-off process as seen in Figure 4.26. To improve substrate lift-off for high-resolution features, a bi-layer method was attempted to allow a top surface with a lower sensitivity to etching, which would improve undercut after plasma etching. However, after testing multiple resists including HSQ, ZEP520, and PMMA on top of the NIL resist, it was found that the dispensing solvents removed the NIL resist during spinning. The ability to imprint features down to 50 nm pitch were observed routinely, however clearance, variation in etch rates between opened regions, and undercut profiles from the imprinting made lift-off only possible down to 100 nm pitch regions.

Overall, NIL was found to include various processes of nanofabrication that needed adjustments in order to achieve repeatable imprints and allow for proper lift-off for fabricating SERS devices. Despite many of the challenges seen, consistency in fabrication was obtained for features down to 100 nm pitch. Several aspects including mold design, and fabrication, application of anti-adhesion coatings, modifications to the

temperature, pressure and time of imprints, and the lift-off process all required significant planning and reiterative modifications. The results obtained show the potential feasibility of using nanoimprint lithography for scalability in manufacturing of SERS and other devices requiring nanoscale resolution. Although this field of NIL is continuing to develop, already the control over resolution has allowed for fabrication of devices testable using SERS.

4.3. Electron Beam Evaporation, Lift-off, and Fabrication of Metal Nanostructures

Deposition of the metal used for the nanostructured features for both EBL and NIL fabricated substrates was done using a lift-off process. For fabrication of all SERS devices, 10 nm films of metal were deposited on the surface of the sample by electron-beam evaporation. Thicker metal films above 10 nm did not allow for proper lift-off processing with EBL or NIL due to lift-off process used. Resist patterned samples were placed in the Kurt J. Lesker electron-beam evaporator system and the tool was pumped down to a base pressure below 1×10^{-4} Pascal. Deposition of the metal layers was performed at rates between 0.1 and 0.4 nm/sec for total thicknesses of 10 nm. Films of chromium, silver, copper, gold and nickel, including various combinations of the different metals were used depending on the requirements of the test. Silver, copper, and gold were all used as plasmonic materials whereas chromium was used to improve adhesion of the silver to the fused silica. It was found that no adhesion layer was needed for copper or gold to the glass. Nickel was used in some cases for immobilization of proteins exploiting the strong binding between nickel and histidine tags used on some proteins. Patterned regions in the resist allowed for metal to enter into the opened regions of the resist to adhere to the underlying surface. Figures 4.27–4.29 show periodic dot arrays fabricated using both EBL and NIL.



Figure 4.27 – EBL fabricated 100 nm pitch gold dots on a fused silica substrate after lift-off. The nucleation of the gold layer can be seen with the individual dots.

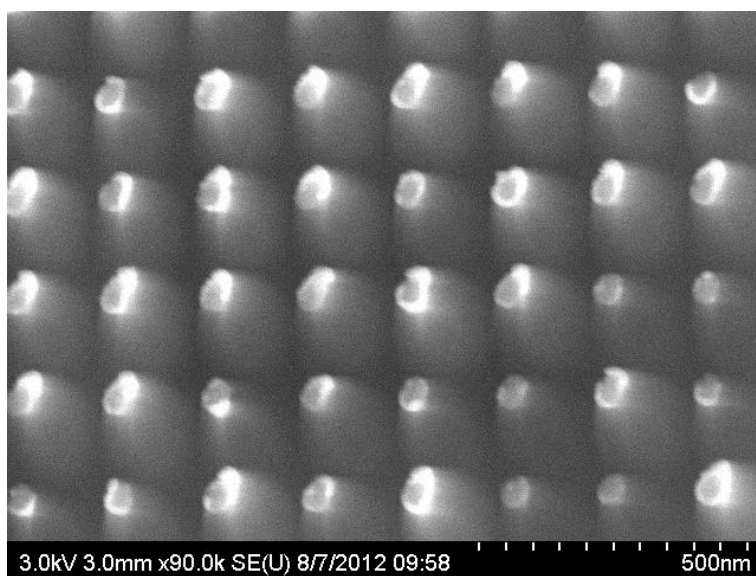


Figure 4.28 – SEM image of 200 nm pitch 10 nm thick gold periodic dot array fabricated after a NIL process and subsequent lift-off to form metal uniform dot arrays. Lift-off using was done by soaking the samples in a heated N-Methyl-2-pyrrolidone (NMP) solvent prior to sonicating the samples in the solvent. It was found that NMP offered improved results compared to acetone for lift-off for NIL fabricated SERS substrates.

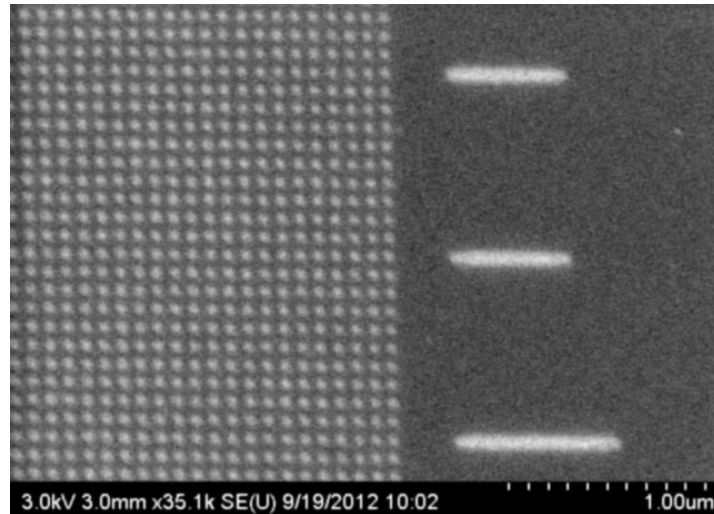


Figure 4.29 – SEM image of 100 nm pitch 10 nm thick copper dots on a fused silica substrate fabricated using NIL and a lift-off process. Lift-off was done by soaking the samples in a heated NMP solvent prior to sonicating the samples in the solvent.

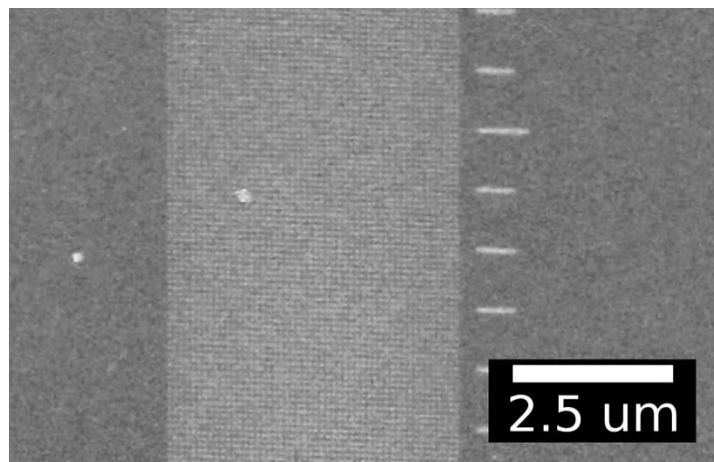


Figure 4.30 – Array of 100 nm pitch copper dots on a fused silica substrate fabricated using NIL with lift-off done using a heated NMP solvent.

Because of the directionality of the evaporated metal, sidewall coverage was limited, which is critical for lifting-off of the resist, which acts as a sacrificial layer. The lift-off process included soaking the samples in a strong solvent of acetone for PMMA resist or NMP heated to above 50 °C for the nanoimprint NXR-1025 resist, and then sonicated for one to two min. It was found that soaking samples in the solvents reduced the time needed for sonication, with EBL-patterned substrates requiring 5 minute soaks in acetone while NIL substrates were soaked for 20 min in a heated N-Methyl-2-

pyrrolidone (NMP) solvent. The solvents cause the resist to swell which assists in the lifting-off process. Metal EBL-patterned substrates were fabricated with various features including honeycombs, and dot pitches down to 40 nm and metal thicknesses of 10 nm (see Figures 4.27 and 4.31). These various geometries were tested using Raman spectroscopy to determine the effects on signal enhancement based on aspects known to give the highest enhancements[11]. For nanoimprinted substrates, 100 nm and higher pitches were consistently obtained; however, lower pitches proved to be too difficult for lift-off, despite some successful imprints observed down to 50 nm pitch. The variation in rate for lower pitches, lack of undercut, and adhesion were some of the main challenges in obtaining the lower pitches with NIL. It was also found that chrome lift-off used for fabricating NIL molds required a longer soak in acetone prior to sonication, which was attributed to the smaller grain size of the chrome. This limited the solvent from removing the top layer of chrome in some cases.

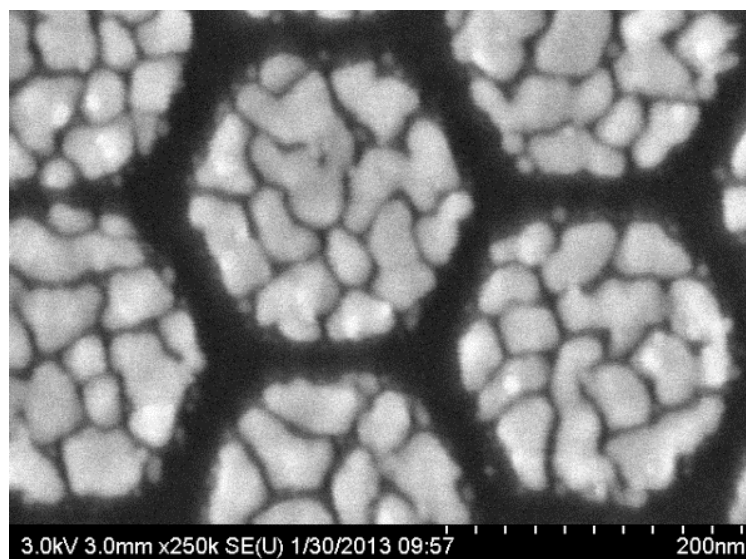


Figure 4.31 – EBL fabricated gold honeycomb shaped nanostructures on a fused silica substrate used for SERS. Gold nucleation from deposition can be seen in the structures from the evaporation process. PMMA development was done using a room temperature IPA:H₂O (7:3) development process. Image was provided by Luis Gutierrez-Rivera.

5. Biosensor Results and Discussion

Tests to determine the effectiveness of the nano-patterned SERS substrates in controlling signal enhancement as well as determining the effectiveness of the substrates for SERS are presented here. Experiments demonstrating the devices' ability to tune signal enhancement based on pitch, and antiparticle spacing are shown. Further, demonstration of specific bonding between and immobilized recognition element, a dopamine binding aptamer and dopamine is shown using honeycomb gold nanostructures fabricated using EBL.

Assistance with SEM imaging, fabrication and other help from Luis Gutierrez-River and Mariam Japanwala was vital to this work. Of note, Figures 5.5–5.6 were obtained from Luis, as well as the spectrum of protein A in solution used in Figure 5.4.

5.1. SERS detection of Protein A

Protein A is a unique protein known to have a strong binding affinity to the heavy chain of immunoglobins or antibodies of many mammalian species. It is a part of a group of proteins that bind antibodies with different specificities [145, 146]. Protein A was discovered originally in the bacterium *Staphylococcus aureus*, and is commercially available along with a recombinant fusion protein linked to protein G of the same family, due to its potential for a number of sensing applications (see Figure 5.1) [147, 148]. The ability to measure the binding of protein A on a surface using SERS, prior to sensing of analytes, can be beneficial to confirming the immobilization of the protein directly. Although SERS requires analytes to be within a short range of the surface, making analyte-antigen detection difficult with SERS, the small size of protein A makes it a useful protein to measure and use for testing of the nanofabricated SERS substrates [149].

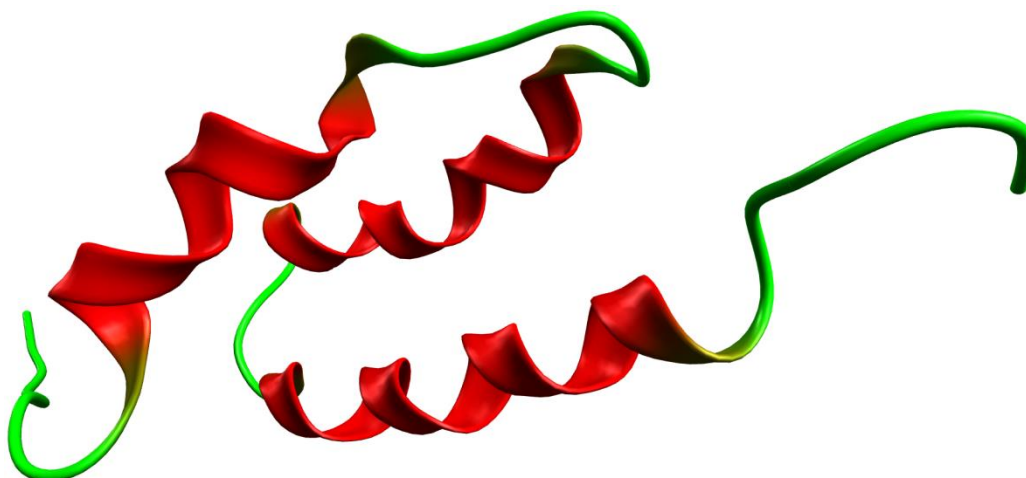


Figure 5.1 - 3D model of Protein A from solution NMR spectroscopy, obtained from the RCSB Protein Data Bank (1BDD) [129]. The protein was rendered using the Avogadro software.

SERS substrates with metal dots of 50, 100, and 200 nm pitch with varying inter-dot gap sizes were fabricated on fused silica substrates using electron beam lithography (EBL) as described in chapter 4. Gap sizes were controlled based on the relative dose used, and verified using SEM images in correlation with optical images taken during Raman measurements. Samples with copper, silver, and gold nanostructures were used to determine the corresponding enhancement from the different metals. Figure 5.2 shows an example of 100 nm pitch silver dots fabricated on a fused silica substrate that was used for detection of protein A using SERS. Evaporated films on fused silica were also used throughout to allow for comparison between the Raman signal of different tests and for faster processing.

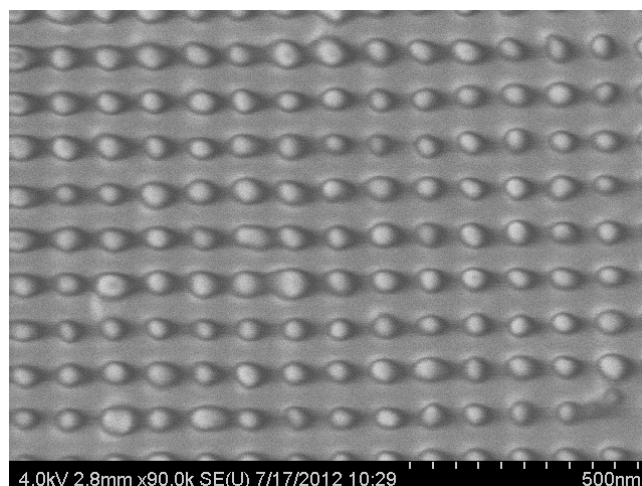


Figure 5.2 – SEM image of 100 nm pitch silver dots on a fused silica substrate with an average 15 nm gap distance between dots. This sample and others were used for obtaining SERS spectra of immobilized protein A.

Protein A molecules were modified to have multiple thiol groups on the outer surface of the protein by attaching thiol-terminated linkers to the surface of the protein. These linkers take advantage of the strong bond between thiol groups and noble metals, allowing for increased yields of immobilization of the protein to the metal. Unmodified and thiolated protein A was obtained from ProteinMods, where the protein was estimated to have approximately 2.8 sulfhydryl groups per protein on the surface which were known not hinder the functional properties of the protein [150].

Drops of protein A and thiolated protein A (490 μ M) were placed on separate samples for 72 hours at 4 °C. The un-thiolated protein A was in a non-buffered water solution with a pH of 7 and the thiolated protein was in a buffer of Na Citrate with a pH of 5.5. The stability of protein in a range of pH values was confirmed by the manufacturer, where changes pH changes from acidic to basic and vice-versa were not expected to cause unfolding of the proteins. After the protein was allowed to immobilize to the surface, samples were rinsed thoroughly in a phosphate buffered saline (PBS) with a pH of 7.4 and sealed in the same buffer, accordingly to the procedure outlined in

section 3.21. Control samples were also tested using the PBS buffer solution for comparison. No tests were conducted with the Na citrate buffer, however comparison between unmodified protein A in water and the thiolated protein showed comparable SERS spectra. Samples with both silver and gold nanostructures were found to be compatible with the Na citrate buffer, while tests with copper found that the buffer reacted with the metal, removing features from the devices. Silver and gold films were used to obtain the basic spectra of protein A, while silver 100 nm pitch dots offered the highest signal enhancement overall. Peaks seen from the PBS buffer at 602, 790, 1063 and 1632 cm^{-1} were unobserved with SERS, however the Raman active spectrum of Na citrate buffer had a number of peak which did overlap with the protein, although the spectrum of un-buffered Protein A gave important information [152].

Raman spectra of immobilized protein A on 10 nm metal films of both silver and gold using thiolated and unmodified protein A in Figure 5.3 show the variation in Raman signal intensity between the different samples. Comparison of the signals shows that for both silver and gold films, the Raman signal from the thiolated protein is much higher than those without, although the spectrum of protein A is visible in each case. The stacked spectra in Figure 5.3 also shows that the silver film gives increased Raman enhancement for many of the peaks observed. Raman spectra were obtained using a 12 mW, 532 nm excitation wavelength with a 6-s acquisition time. It was found that although the signal could be detected from protein A, the laser power needed to be reduced to 10% to not damage the protein and sample due to the high energy and focused spot size of the tool. The reduced laser energy was calculated to be approximately 1.2 mW compared to the full power, compared to the 12 mW full power. Repeated exposures on a single point verified the damage as the signals diminished after various runs at full power (see Figure 5.4). This was attributed to damage or denaturing

of the protein as well as damage to the metallic structures, as verified using SEM when high energies were utilized. No such damage was observed for sampling using a 10% power [153]. Figures 5.4–5.6 show the morphology of both silver and gold pads as well as the focusing tool used for Raman imaging.

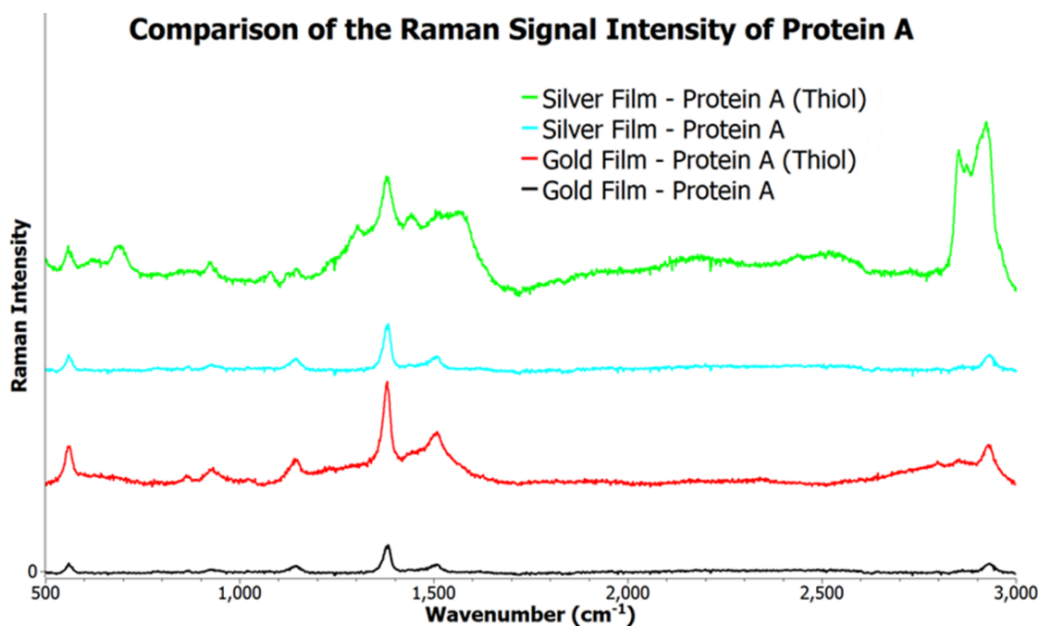


Figure 5.3 - Comparison of the signal intensity of protein A using thiol mediated binding on silver and gold pads. Immobilization of the thiolated protein A on pure silver films gave the strongest SERS signals compared to other films. For these samples, a 1.2 mW, 532 nm excitation wavelength was used for the Raman sampling for 3 s at all wavelengths. Spectra are offset vertically for easier comparison.

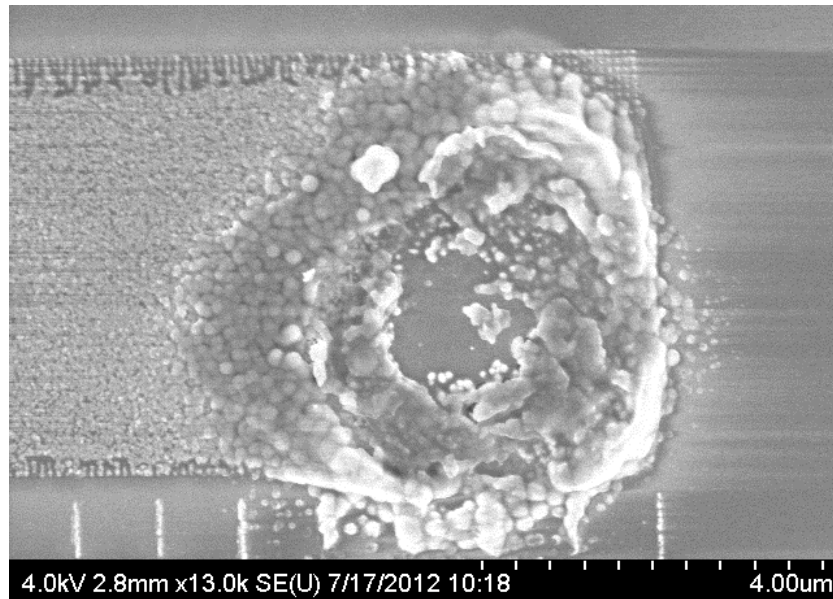


Figure 5.4 - Laser induced damage to a 10 nm silver film after Raman imaging at full laser power. Reduction of the laser power to 1.2mW was found to allow sufficient signal enhancement without damage to the underlying material.

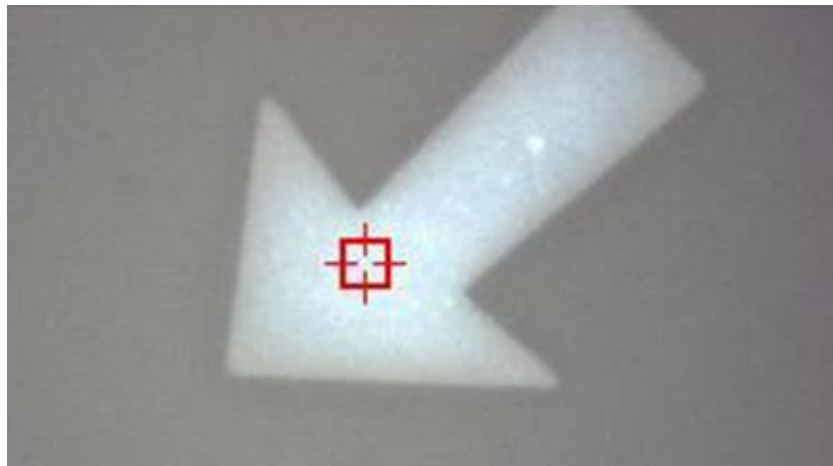


Figure 5.5 - Optical microscope image showing the method of measuring the Raman intensity from a single spot. Here the arrow is composed of a 10 nm thick silver film on fused silica fabricated using EBL with a total area of approximately $1500 \mu\text{m}^2$ and a focus in the range of $1 \mu\text{m}$ at 50X magnification.

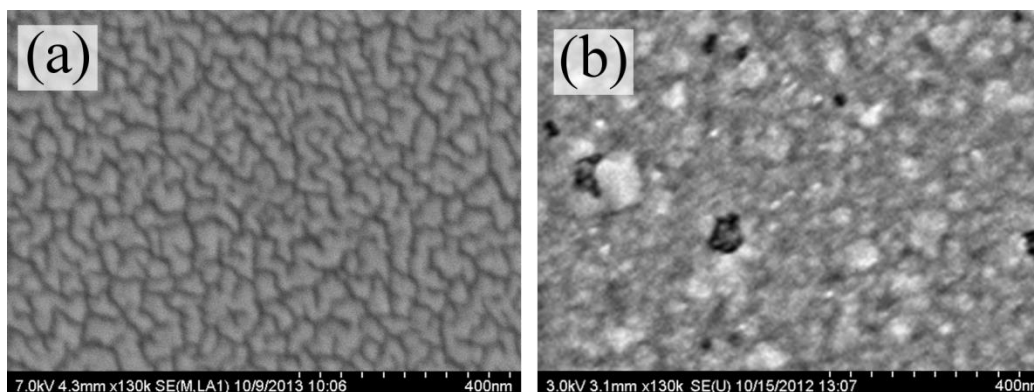


Figure 5.6 – SEM images of a 10 nm films of (a) gold and (b) silver evaporated on fused silica substrates at 130 000 magnification. Thin metal films were used to compare Raman intensity variations between silver and gold films with immobilized protein A.

Figure 5.7 shows the Raman spectra of immobilized protein A on silver and gold films, as well as protein on 100 nm pitch silver dots. The spectrum of the protein in water is also shown for comparison. The nano-patterned dots enhanced the Raman signal approximately more than the silver or gold films of the same thickness. Raman spectra were obtained using a 12 mW, 532 nm excitation wavelength with a 6-s acquisition time, except in the case of the protein in solution which acquired using a longer time. Other tests were performed with lower laser powers and similar results were obtained but with increased noise due to the lower power.

From these results, it was demonstrated that nano-patterned SERS structures gave substantially higher Raman enhancements compared to bare metal structures, with control over inter-gap distances and pitch allowing for precise signal enhancement based on the plasmonic structures. Some of the most significant Raman peaks from protein A observed are recorded in Table 2 compared with published data on protein A. Variations in the Raman peaks between immobilized protein and protein in solution was seen, which is can occur for certain analytes, especially when immobilized on a surface [115, 154].

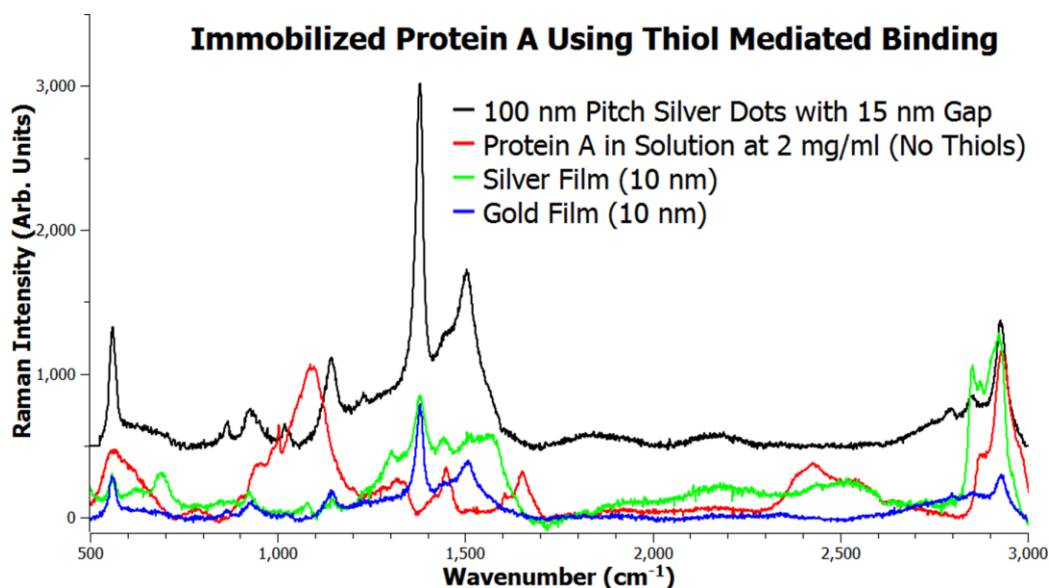


Figure 5.7 - Comparison of the SERS spectra of immobilized protein A on silver and gold films and on 100 nm pitch silver dots with 15 nm inter-dot gap distance with the Raman spectrum of the protein in solution at 2 mg/ml. Tests were done with a 532 nm excitation wavelength at 10% power except for the protein in solution which was obtained at full power. A significant difference was seen in a number of peaks after immobilization of the protein.

Table 2 - Observed Raman Peaks of Protein A Compared with Published Data and Interpretation of Peaks

| Published Data of Raman Shifts in Solution (cm-1) [14, 149] | Raman Peaks (cm-1) Observed from SERS Structures | Postulated Source of Peaks [14, 149, 155, 156] |
|---|--|--|
| 563 | 560 | |
| 781 | - | Tryptophan |
| - | 865 | |
| 950 | 930 | C-C Stretching |
| 1000 | 1020 | Phenylalanine |
| 1091 | 1090 | |
| 1150 | 1144 | lysine |
| 1272 | - | glutamine and asparagine |
| - | 1230 | |
| 1316 | 1305 | |
| - | 1380 | CH ₃ sym. Bend, Tryptophan |
| 1450 | 1450 | |
| 1505 | 1505 | lysine |
| 1605 | - | |
| 1640 | - | C=O stretching |
| 2426 | - | Cysteine sulfhydryl groups |
| - | 2790 | |
| 2890 | 2860 | C-H stretching |
| 2931 | 2929 | C-H stretching |

To further test the capabilities of nano-patterned SERS substrates for controlling signal enhancement, comparison of the SERS signals from thiolated protein A on 100 nm pitch dots with varying inter-dot gap distances was performed. Figures 5.8 and 5.9 show that varying gap distances from the SERS structure had a significant effect on the intensity of the signal obtained. The highest Raman signal was seen as the gap size reduced to 15 nm, which produced signals substantially higher than the silver film with the same parameters (see Figure 5.2).

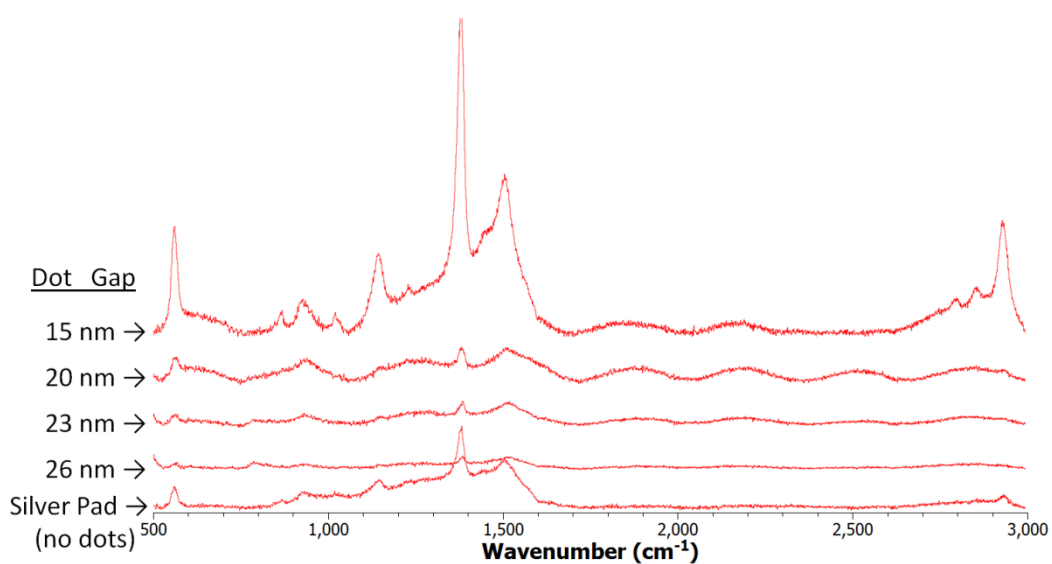


Figure 5.8 - Spectra of protein A immobilized on 100 nm pitch silver dots with various inter-dot gaps taken with a 532 nm excitation wavelength and three 1s integrations of the Raman shifted wavelengths.

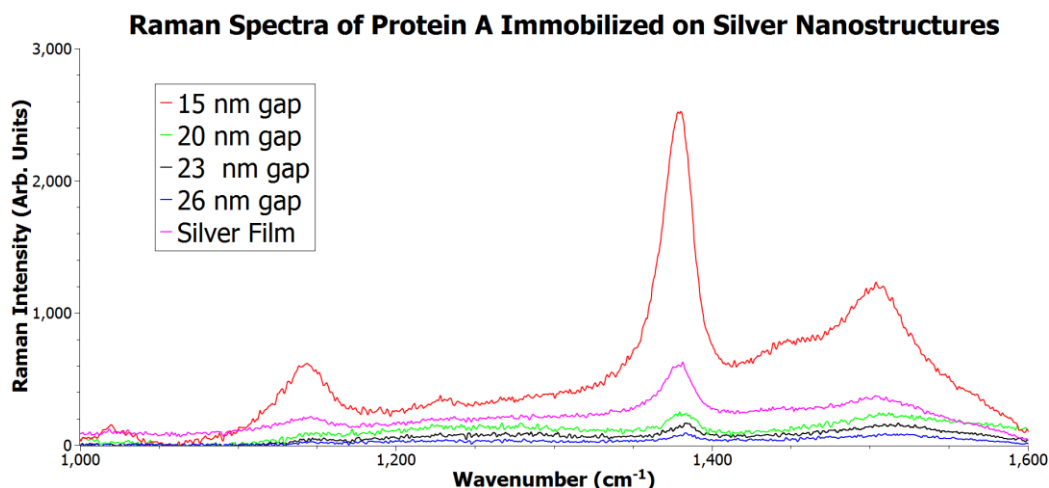


Figure 5.9 – Comparison of the intensity of the peak at 1380 cm^{-1} from immobilized protein A on silver dots with 100 nm pitch and varying inter-dot gap distances as well as comparison of the Raman signal protein immobilized on a silver film.

Sharpened peaks of the signal can be attributed to the increased signal enhancement arising from the small inter-dot gaps, which are known to produce high intensity Raman signals or “hot spots”. These results validated the effectiveness of the nano-fabricated SERS substrates in providing high signal enhancement, as well as control over the signal intensity based on fabricated structures with significant control.

The ability to “tune” the signal intensity of SERS devices using varying dot pitch and inter-dot distances is seen in Figures 5.8 and 5.9. This validates that signal intensities, which are not always predictable with SERS, can be controlled to some extent by regulating the plasmonic structures used for enhancement. A similar experiment with a silver/copper base layer gave comparable results, with an approximate 4:1 signal enhancement comparing the intensity of the metal films with the 15 nm gap sections at 1380 cm^{-1} . Raman peaks in these regions were substantially higher than in regions with silver films, also demonstrating that the high signal was not due to increased concentration of the analyte.

Overall, testing of the SERS devices using protein A validated that plasmonic biosensing using nano-fabricated devices can provide significant control over signal enhancement, which is a fundamental basis for using SERS in biosensing applications requiring control in signal. Control over features, with 100 nm pitch silver dots showing the highest signal enhancement out of signals obtained, which could be due to the matching periodicity of the structures with the excitation wavelength. This work demonstrates that such devices could also be used for the detection of other biological or chemical analytes with high Raman signal enhancement with control over the signals obtained. Additionally, further work demonstrating the reproducibility of the enhancement between multiple samples would be beneficial to furthering this work.

5.2. Aptamer Based Biosensing of Dopamine

Dopamine is a neuromodulator that has critical functions in both brain and nervous system activities. Determining dopamine levels, which are directly related to a number of health related issues including Parkinson's disease, schizophrenia and psychosis, attention deficit disorder, as well as other health issues such including drug abuse, pain, and nausea, is important for basic research in many fields [157-162]. Dopamine itself is strongly Raman active, making SERS a useful technique for detection of the molecule. Methods to immobilize dopamine are required, however, for SERS to be effective as dopamine has no specific binding to metal. Further, binding methods for dopamine require detection of the dopamine molecule, without adding a significant background signal.

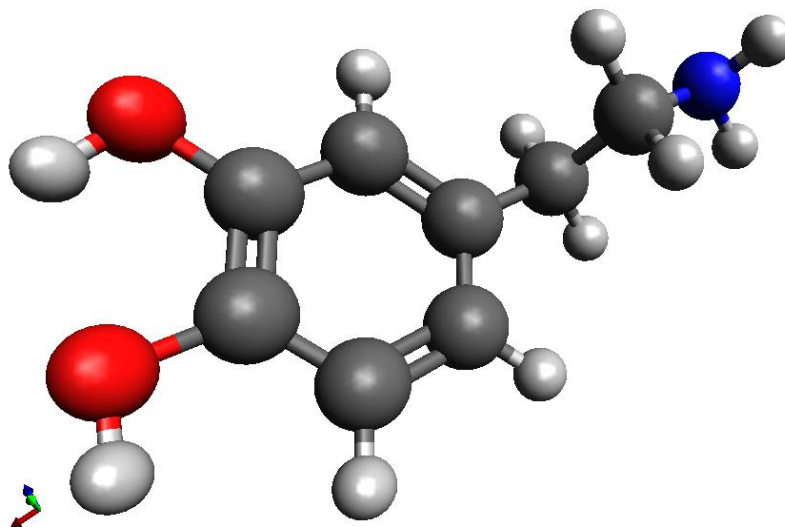


Figure 5.10 - Structure of a dopamine molecule visualized in Avogadro [125].

Single stranded RNA and DNA aptamers have been found to have high binding affinity to a number of small molecules, making them a useful recognition component for biosensing. A RNA aptamer that has been found to bind strongly to dopamine, has been shown to have a DNA homolog, which is known to maintain the same binding sites for dopamine, with an increased binding affinity and a similar specificity to the molecule [163, 164]. The predicted binding site between the RNA aptamer and dopamine was also present on the DNA homolog, which explains why binding was found to be similar for both the RNA and DNA forms (see Figure 5.10).

Aptamers offer many benefits as biorecognition elements for SERS biosensing, their small size and low Raman cross-section are beneficial for detection [165]. Because the SERS effect largely depends on the proximity of the analyte to the surface, the small size of the DNA aptamers allows analytes to be within a few nanometers of the surface. Aptamers are easier than proteins to produce, and are also less expensive and time consuming to make. Since DNA is intrinsically fluorescent [166], it was found that the 532 nm excitation source produced too much fluorescence to detect binding, therefore

all tests were done using a 780 nm excitation source. The laser was set to 2.7 mW, with 4 s total exposure times across all wavelengths measured.

Dopamine binding aptamers were purchased from Integrated DNA Technologies, Inc., with a thiol-modified end, which allows linking of the aptamer to gold surfaces. The sequence of the aptamer starting from the 5' end is S-S/AAAAAAAAA-GTCTCTGTGT-GCGCCAGAGA-ACACTGGGGC-AGATATGGGC-CAGCACAGAA-TGAGGCCC-3'. Predictions of the aptamer folding structure were done using ValFold [167] software and visualized using PseudoViewer 3.0 with similar folding for the highest likelihood estimates, which all maintained similar loop structures of the aptamer (See Figure 5.11) [168].

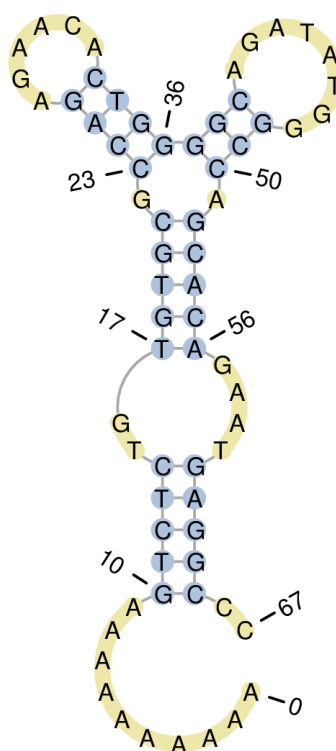


Figure 5.11 - ValFold predicted secondary structure of the dopamine binding aptamer modeled in PseudoViewer 3.0. The letters G, A, T, and C correspond to guanine, adenine, thymine, and cytosine nucleic acids, respectively. The long adenine string at the base was terminated with a thiol group to allow immobilization of the DNA with proper orientation.

A Raman spectrum of dopamine in crystal form was obtained with both 532 nm and 780 nm excitation wavelengths and is shown in Figure 5.11. Simulation predictions, used for determining different peak assignments to the molecule were done using GAMESS simulations are also seen in Figure 5.12 [169]. Much of the Raman spectrum comes from the ring bending from the benzene ring of the molecule, while some C-H stretches at around 3000 cm^{-1} were not observed using the 780 nm excitation wavelength (see Figure 5.12). Some of the other major peaks involved ring bending of dopamine, included those at 395, 550, 595, 750, 795, and 1620 cm^{-1} . N-H vibrational modes at 265, 330, and 880 cm^{-1} were observed. A more thorough analysis of the origins of the different peaks has been published elsewhere [169].

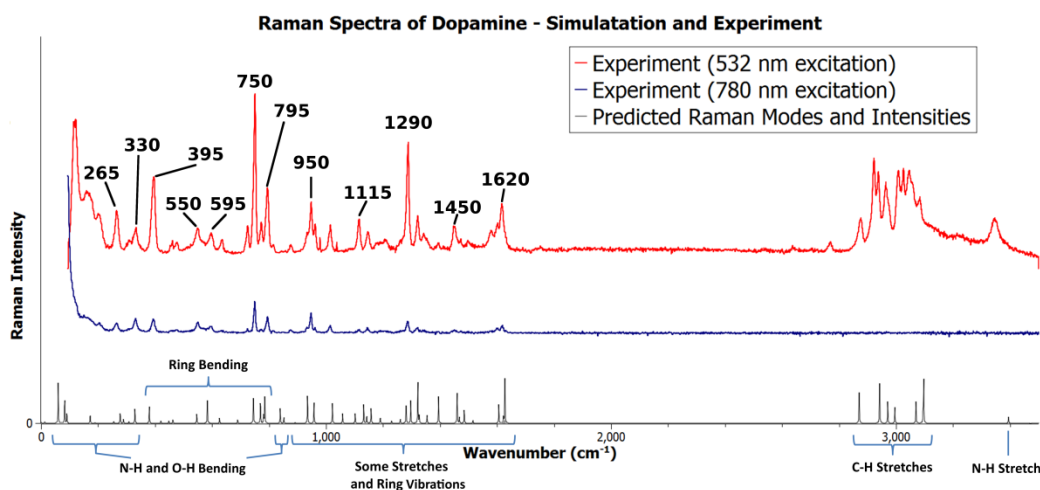


Figure 5.12 – Stacked Raman spectra of dopamine with 532 nm and 780 nm excitation compared with simulated peaks. Simulation and analysis was done using General Atomic and Molecular Electronic Structure System (GAMESS), Facio, and MacMolPlt software. Here the 532 nm and 780 nm excitation wavelengths were set to 2.1 mW and 2.7 mW respectively, with 4 s acquisition times across all wavelengths.

Tests to measure binding of dopamine to the immobilized aptamer using gold films and nano-patterned SERS substrates were carried out on fused silica substrates with various dot arrays and other structures, including gold honeycombs. Dopamine binding aptamer was diluted to $1\text{ }\mu\text{M}$ in a 7.4 pH TRIS(tris(hydroxymethyl)aminomethane)-

EDTA(ethylenediaminetetraacetic acid) buffer and a drop was placed over several substrates with gold films and nano-patterned arrays and left at room temperature for one hour in a covered petri dish to prevent evaporation. Samples to measure the Raman spectrum of the aptamer were rinsed three times in a potassium phosphate (K_3PO_4) buffer and placed in the same buffer solution for imaging, according to the method outlined in section 3.12 (see Figure 5.13). The observed Raman spectra of the aptamer was very weak, with 780 nm excitation (see Figure 5.13 and Figure 5.14). Dopamine solutions in buffer were added to the substrates by placing a 5 μ L drop of dopamine (5 μ M) on the separate samples, mixing with the existing drop of aptamer in buffer to prevent the samples from drying. After ten min the samples were rinsed again in the potassium phosphate buffer and sealed in the microscope slides for Raman imaging to test for binding of the analyte using SERS. Figure 5.13 compares the Raman spectra of immobilized aptamer before and after addition of the dopamine molecule on gold honeycomb structures. Signal from samples exposed to only dopamine showed no resultant dopamine signal, confirming that dopamine does not bind strongly to gold.

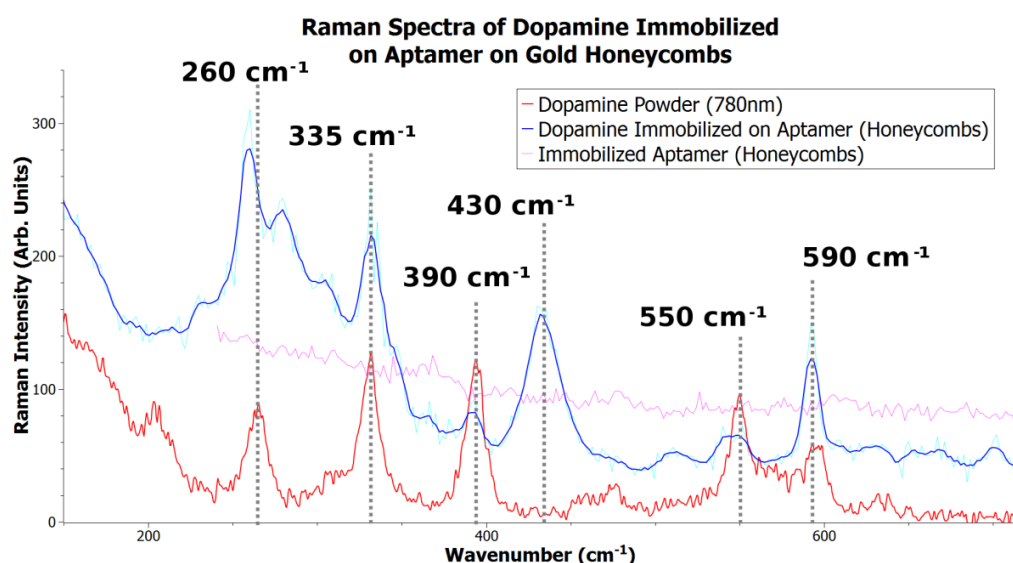


Figure 5.13 - Spectrum of immobilized aptamer on gold honeycombs using a 780 nm excitation wavelength. Protein was immobilized for one hour at a concentration of 1 μ M and the aptamer was placed for 10 min at 5 μ M for this experiment.

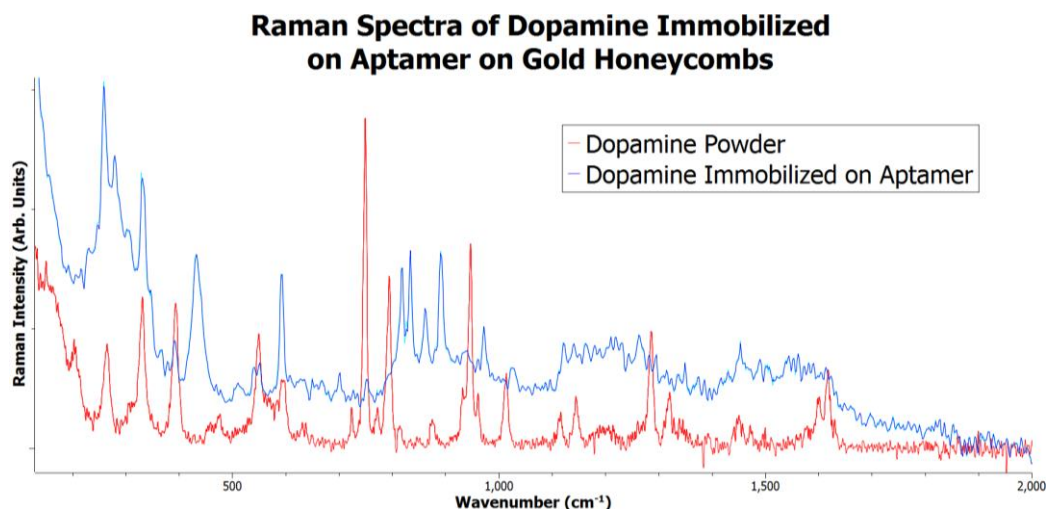


Figure 5.14 - Spectrum of immobilized aptamer on gold honeycombs using a 780 nm excitation wavelength. Peaks arising from ring bending between 700 cm^{-1} and 800 cm^{-1} were not seen, however similar peaks between 800 cm^{-1} and 900 cm^{-1} were observed. The spectra were smoothed for easier comparison.

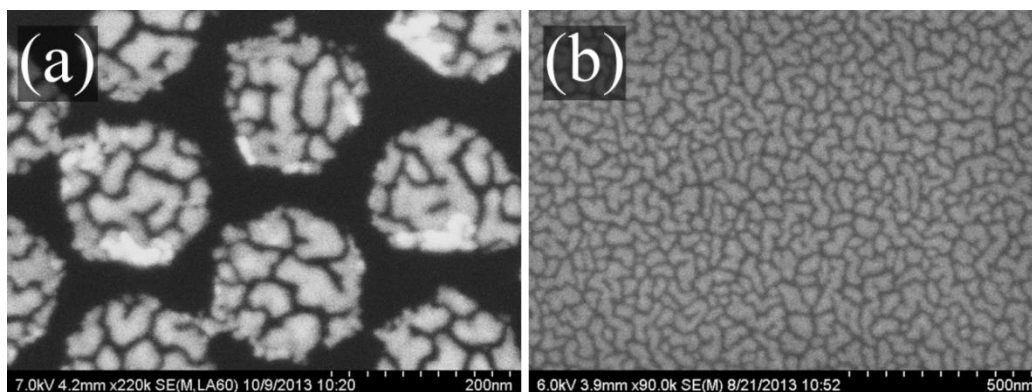


Figure 5.15 - SEM images of (a) gold honeycomb structures and (b) gold film used for SERS detection of dopamine using DNA aptamers for immobilization.

In summary, gold honeycomb structures used for detection of immobilized dopamine on DNA aptamers using SERS was shown to be a valid biosensing detection scheme for the nano-patterned substrates. A number of the Raman peaks originating from the dopamine molecule in powder were observed after binding of the dopamine molecule, however variation in the overall spectrum was different in many regions, which does occur in SERS [115]. Simulation of the Raman spectrum of dopamine powder allowed

for increased understanding of the interaction between the molecule and the aptamer. This aided in explaining possible variations in measured Raman peaks after binding. Tests to determine background signals arising from the aptamer and non-specific binding of the dopamine molecule to gold showed that the aptamer-dopamine pair had excellent specificity, without any significant background signal.

6. Conclusion and Future Work

Reliability of signal intensities in surface-enhanced Raman spectroscopy is one of the major challenges for the detection of analytes with consistent signal enhancement. Critical to achieving large signal intensities consistently in SERS, control over the variability of metallic features at the nanoscale is required. Modern nanofabrication methods including electron beam lithography and nanoimprint lithography have the ability to produce structures at the deep nanoscale with significant control and reproducibility. To demonstrate the effectiveness of these fabrication methods for control over signal enhancement and use in biosensing, EBL and NIL fabricated substrates were demonstrated to be effective methods for producing the required nanostructures. To test whether such devices could be used for the detection of biological sensing of protein and for specific binding of analytes, nanofabricated SERS substrates were used for the detection of dopamine using immobilized DNA aptamers as well as protein A, a commonly used protein in many biosensing applications. In this work, demonstration of a number of the aspects in the fabrication and testing of SERS substrates was given. Conclusions to some of the key aspects of this work are presented here:

SERS Substrate Fabrication

1. Conductive polymers, due to their simplicity in processing, and extension of processing conditions, are an effective method for mitigating the effects of charging during EBL processing for dielectric materials. Their ability to extend processing conditions to those on traditional semiconductive substrates demonstrates their advantage when used for anti-charging.

2. Removal of aluminum layers used for anti-charging in EBL can degrade patterned features for PMMA when excessive etch times are used.
3. Comparison with simulated results allowed for additional understanding of the EBL process, which helped interpreting some experiments such as with aluminum conductive layer removal.
4. Cold development, along with co-solvent development using IPA:H₂O (7:3), is able to extend the processing capabilities for fabrication of SERS substrates, for greater consistency of periodic features with greater consistency than room temperature development. This is ideal for consistency in SERS as variations in processing, exposure dose, and development time are mitigated using cold development.
5. Nanoimprint molds were fabricated using an EBL and ICP-RIE process that allowed for control over pillar heights using a silicon base etch stop using a SiO₂ etch process.
6. Anti-adhesion layers on both silicon based molds and on the surface of the NIL resists were demonstrated to be effective in reducing sticking between samples and molds during imprinting. The hydrophobicity of the surfaces was verified using contact angle measurements.
7. A thermal nanoimprint lithography process was used for the fabrication of arrays of metal nanostructures down to 100 nm pitch with high yields. Aspects including anti-adhesion layers, temperature, time and pressure during imprinting, and plasma etching of resist to gain clearance for lift-off were optimized for controllable substrate fabrication.

SERS Biosensing

8. SERS detection of immobilized protein A was demonstrated using gold and silver nano-patterned structures as well as evaporated films. Nano-patterned periodic structures showed the highest signal enhancements.
9. Control over SERS intensities using highly uniform silver nano-structured dot arrays with varying inter-dot gap spacing and pitch on fused silica substrates was demonstrated confirming the effectiveness of nanofabricated SERS structures.
10. Choice of metal was found to be significant as silver provided the highest Raman signal enhancements, however, chemical incompatibility of silver with some buffers was observed. Gold, however, offered SERS signals with no observed buffer incompatibilities.
11. Gold honeycomb nanostructures were shown to provide the highest overall signal enhancement, offering detection analytes with 780 nm excitation wavelengths where other structures gave little enhancements.
12. Detection of specific binding recognition with high specificity towards dopamine was achieved using a single stranded DNA aptamer immobilized on gold nano-patterned honeycomb structures.

Due to the scope and potential of this work, there is tremendous opportunity for further developments in the field of SERS biosensing. Ideally, with one of the largest challenges to biosensing being the biorecognition interaction, a broader range of analytes, especially those incorporating DNA aptamers would be quite beneficial to pursue. Further efforts in improving the signal enhancement and reproducibility of the

signal of the aptamer/analyte pair will be important. Nano-patterned metal honeycombs structures were required to obtain the enhancement needed for longer wavelengths where periodic dots were ineffective. Further testing and iterations of different geometries that provide both Raman hot spots and compatibility with the excitation source would be a useful area of further focus. The time and cost of fabricating substrates using EBL was a somewhat slow iterative process; however, tests to validate and show the capability of these substrates for quantitative analysis is clearly an important milestone for future testing.

Another fundamental aspect of this work that further work that would be beneficial to pursue would involve additional methods to improve consistency in signal enhancement for quantitative analysis. In order to do such thorough testing, mass fabrication of substrates would be beneficial. NIL offers the potential for high throughput fabrication and further work to improve resolution and consistency would be of particular interest using this method. Bilayer UV imprinting could possibly allow improved lift-off processing while offering consistency and resolution, despite the added complexity of fabrication processing. As new methods, materials, and understanding continue to be developed, the capabilities of NIL will likely have a significant impact on future fabrication in biosensing as well as in many other fields.

Overall, this research has been a fascinating endeavor encompassing a number of aspects of engineering including nanofabrication, physics, chemistry, and analytical spectroscopy. The potential and wide scope of biosensing made this project an exciting, unique, and challenging experience. In particular, the role of my supervisors, colleagues, funding and access to the many tools, resources and people at University of Alberta and the National Institute for Nanotechnology (NRC), was paramount to this allowing work.

7. Works Cited

- [1] G. Timp, Nanotechnology, New York: Springer-Verlag, 1999.
- [2] K. E. Drexler, Engines of Creation 2.0, Wowio Books, 2006.
- [3] M. C. Roco, C. A. Mirkin and M. C. Hersam, Nanotechnology research directions for societal needs in 2020: Retrospective and outlook, vol. 1, Springer, 2011.
- [4] R. P. Feynman, "Theres plenty of room at the bottom," *Engineering and Science*, vol. 23, pp. 22-36, 1960.
- [5] P. Poncharal, Z. Wang, D. Ugarte and W. A. de Heer, "Electrostatic deflections and electromechanical resonances of carbon nanotubes," *Science*, vol. 283, pp. 1513-1516, 1999.
- [6] M. A. Mohammad, C. Guthy, S. Evoy, S. K. Dew and M. Stepanova, "Nanomachining and clamping point optimization of silicon carbon nitride resonators using low voltage electron beam lithography and cold development," *Journal of Vacuum Science Technology B: Microelectronics and Nanometer Structures*, vol. 28, pp. C6P36-C6P41, nov 2010.
- [7] Y. Dan, Y. Lu, N. J. Kybert, Z. Luo and A. C. Johnson, "Intrinsic response of graphene vapor sensors," *Nano Letters*, vol. 9, pp. 1472-1475, 2009.
- [8] X. Hoa, A. Kirk and M. Tabrizian, "Enhanced SPR response from patterned immobilization of surface bioreceptors on nano-gratings," *Biosensors and Bioelectronics*, vol. 24, pp. 3043-3048, 2009.
- [9] J. N. Anker, W. P. Hall, O. Lyandres, N. C. Shah, J. Zhao and R. P. Van Duyne, "Biosensing with plasmonic nanosensors," *Nature materials*, vol. 7, pp. 442-453, 2008.
- [10] M. Fan, G. F. Andrade and A. G. Brolo, "A review on the fabrication of substrates for surface enhanced Raman spectroscopy and their applications in analytical chemistry," *Analytica chimica acta*, vol. 693, pp. 7-25, 2011.
- [11] J. A. Dieringer, A. D. McFarland, N. C. Shah, D. A. Stuart, A. V. Whitney, C. R. Yonzon, M. A. Young, X. Zhang and R. P. Van Duyne, "Surface enhanced Raman spectroscopy: new materials, concepts, characterization tools, and applications," *Faraday Discussions*, vol. 132, pp. 9-26, 2006.
- [12] X. X. Han, B. Zhao and Y. Ozaki, "Surface-enhanced Raman scattering for protein detection," *Analytical and bioanalytical chemistry*, vol. 394, pp. 1719-1727, 2009.

- [13] A. Kabashin, P. Evans, S. Pastkovsky, W. Hendren, G. Wurtz, R. Atkinson, R. Pollard, V. Podolskiy and A. Zayats, "Plasmonic nanorod metamaterials for biosensing," *Nature materials*, vol. 8, pp. 867-871, 2009.
- [14] L. Gutierrez-Rivera, R. F. Peters, S. K. Dew and M. Stepanova, "Application of EBL fabricated nanostructured substrates for surface enhanced Raman spectroscopy detection of protein A in aqueous solution," *Journal of Vacuum Science & Technology B: Microelectronics and Nanometer Structures*, vol. 31, pp. 06F901-06F901, 2013.
- [15] X.-M. Qian and S. Nie, "Single-molecule and single-nanoparticle SERS: from fundamental mechanisms to biomedical applications," *Chemical Society Reviews*, vol. 37, pp. 912-920, 2008.
- [16] S. Eustis and M. A. El-Sayed, "Why gold nanoparticles are more precious than pretty gold: noble metal surface plasmon resonance and its enhancement of the radiative and nonradiative properties of nanocrystals of different shapes," *Chemical Society Reviews*, vol. 35, pp. 209-217, 2006.
- [17] C. T. Minh, *Biosensors*, vol. 1, Springer, 1993.
- [18] M. Zourob, Ed., *Recognition Receptors in Biosensors*, Springer, 2010.
- [19] S. P. Mohanty, "Biosensors: A Survey Report," *University of South Florida, USA*, 2001.
- [20] N. A. Hopkins, "Antibody Engineering for Biosensor Applications," *Recognition Receptors in Biosensors*, pp. 451-529, 2010.
- [21] K. Besteman, J.-O. Lee, F. G. Wiertz, H. A. Heering and C. Dekker, "Enzyme-coated carbon nanotubes as single-molecule biosensors," *Nano letters*, vol. 3, pp. 727-730, 2003.
- [22] J. Wang, "Carbon-nanotube based electrochemical biosensors: A review," *Electroanalysis*, vol. 17, pp. 7-14, 2005.
- [23] K. Kerman, M. Kobayashi and E. Tamiya, "Recent trends in electrochemical DNA biosensor technology," *Measurement Science and Technology*, vol. 15, p. R1, 2004.
- [24] Y. Zhang, Y. Wang, H. Wang, J.-H. Jiang, G.-L. Shen, R.-Q. Yu and J. Li, "Electrochemical DNA biosensor based on the proximity-dependent surface hybridization assay," *Analytical chemistry*, vol. 81, pp. 1982-1987, 2009.

- [25] A. de las Heras and V. de Lorenzo, "In situ detection of aromatic compounds with biosensor *Pseudomonas putida* cells preserved and delivered to soil in water-soluble gelatin capsules," *Analytical and bioanalytical chemistry*, vol. 400, pp. 1093-1104, 2011.
- [26] L. D. Mello and L. T. Kubota, "Review of the use of biosensors as analytical tools in the food and drink industries," *Food chemistry*, vol. 77, pp. 237-256, 2002.
- [27] L. Kindschy and E. Alocilja, "A review of molecularly imprinted polymers for biosensor development for food and agricultural applications," *Transactions of the ASAE*, vol. 47, pp. 1375-1382, 2004..
- [28] T. Vo-Dinh and B. Cullum, "Biosensors and biochips: advances in biological and medical diagnostics," *Fresenius journal of analytical chemistry*, vol. 366, pp. 540-551, 2000.
- [29] S. Li, J. Singh, H. Li and I. A. Banerjee, *Biosensor Nanomaterials*, wiley.com, 2011.
- [30] The Hong Kong Institute of Education, "Biosensor - Model of biosensor," The Hong Kong Institute of Education, [Online]. Available: <http://www.ied.edu.hk/biotech/eng/classrm/main.html>, [Accessed 2013].
- [31] R. S. Root-Bernstein and P. F. Dillon, "Molecular complementarity I: the complementarity theory of the origin and evolution of life," *Journal of Theoretical Biology*, vol. 188, pp. 447-479, 1997.
- [32] D. J. Cram, "The design of molecular hosts, guests, and their complexes," *Journal of Inclusion Phenomena and Macrocyclic Chemistry*, vol. 6, pp. 397-413, 1988.
- [33] A. Harada, R. Kobayashi, Y. Takashima, A. Hashidzume and H. Yamaguchi, "Macroscopic self-assembly through molecular recognition," *Nature chemistry*, vol. 3, pp. 34-37, 2010.
- [34] S. H. Gellman, "Introduction: Molecular Recognition.," *Chemical reviews*, vol. 97, p. 1231, 1997.
- [35] M. Beckerman, *Molecular and cellular signaling*, Springer, 2005.
- [36] P. Hinterdorfer and Y. F. Dufrêne, "Detection and localization of single molecular recognition events using atomic force microscopy," *Nature methods*, vol. 3, pp. 347-355, 2006.

- [37] A. Hunding, F. Kepes, D. Lancet, A. Minsky, V. Norris, D. Raine, K. Sriram and R. Root-Bernstein, "Compositional complementarity and prebiotic ecology in the origin of life," *Bioessays*, vol. 28, pp. 399-412, 2006.
- [38] R. M. de Wildt, C. R. Mundy, B. D. Gorick and I. M. Tomlinson, "Antibody arrays for high-throughput screening of antibody--antigen interactions," *Nature biotechnology*, vol. 18, pp. 989-994, 2000.
- [39] Venture Planning Group, "US Home/Self-Testing Diagnostic Market: Diabetes, Pregnancy, Ovulation, Occult Blood--Business Challenges and Marketing Strategies for Suppliers," Venture Planning Group, 2013.
- [40] C. Lewis, "Home diagnostic tests: the ultimate house call?," *FDA consumer*, vol. 35, p. 18, 2001.
- [41] S. S. Iqbal, M. W. Mayo, J. G. Bruno, B. V. Bronk, C. A. Batt and J. P. Chambers, "A review of molecular recognition technologies for detection of biological threat agents," *Biosensors and Bioelectronics*, vol. 15, pp. 549-578, 2000.
- [42] M. Zourob, S. Elwary and A. Turner, *Principles of bacterial detection: biosensors, recognition receptors, and microsystems*, Springer, 2008.
- [43] V. A. Petrenko and I. B. Sorokulova, "Detection of biological threats. A challenge for directed molecular evolution," *Journal of microbiological methods*, vol. 58, pp. 147-168, 2004.
- [44] L. Mazzola, "Commercializing nanotechnology," *Nature biotechnology*, vol. 21, pp. 1137-1143, 2003.
- [45] C. V. Raman, "A new radiation," *Indian Journal of physics*, vol. 2, pp. 387-398, 1928.
- [46] S. L. Zhang, *Raman Spectroscopy and Its Application in Nanostructures*, 2012.
- [47] J. R. Ferraro and K. Nakamoto, *Introductory Raman Spectroscopy*, San Diego: Academic Press, Inc., 1994.
- [48] A. Jaboski, "Efficiency of anti-Stokes fluorescence in dyes," *Nature*, vol. 131, pp. 839-840, 1933.
- [49] R. L. McCreery, *Raman spectroscopy for chemical analysis*, vol. 225, Wiley.com, 2005.
- [50] C. L. Haynes, A. D. McFarland and R. P. Duyne, "Surface-enhanced Raman spectroscopy," *Analytical Chemistry*, vol. 77, pp. 338-A, 2005.

- [51] L. Kastrup and S. W. Hell, "Absolute optical cross section of individual fluorescent molecules," *Angewandte Chemie International Edition*, vol. 43, pp. 6646-6649, 2004.
- [52] K. Kneipp and H. Kneipp, "Single molecule Raman scattering," *applied spectroscopy*, vol. 60, p. 322A, 2006.
- [53] F.-M. Liu and M. Green, "Efficient SERS substrates made by electroless silver deposition into patterned silicon structures," *Journal of Materials Chemistry*, vol. 14, pp. 1526-1532, 2004.
- [54] D. W. Hahn, "Raman Scattering Theory," *Department of Mechanical and Aerospace Engineering, University of Florida*, 2007.
- [55] D. B. Chase, "Fourier transform Raman spectroscopy," *Journal of the American Chemical Society*, vol. 108, no. 24, pp. 7485-7488, 1986.
- [56] B. M. Bode and M. S. Gordon, "MacMolPlt: a graphical user interface for GAMESS," *Journal of Molecular Graphics and Modelling*, vol. 16, pp. 133-138, 1998.
- [57] M. S. Gordon and M. W. Schmidt, "Advances in Electronic Structure Theory: GAMESS a Decade Later," in *Applications of Computational Chemistry: the first forty years*, Elsevier, 2005, pp. 1167-1189.
- [58] M. W. Schmidt, K. K. Baldridge, J. A. Boatz, S. T. Elbert, M. S. Gordon, J. H. Jensen, S. Koseki, N. Matsunaga, K. A. Nguyen and S. Su, "General atomic and molecular electronic structure system," *Journal of Computational Chemistry*, vol. 14, pp. 1347-1363, 1993.
- [59] M. Fleischmann, P. Hendra and A. McQuillan, "Raman spectra of pyridine adsorbed at a silver electrode," *Chemical Physics Letters*, vol. 26, pp. 163-166, 1974.
- [60] M. G. Albrecht and J. A. Creighton, "Anomalously intense Raman spectra of pyridine at a silver electrode," *Journal of the American Chemical Society*, vol. 99, pp. 5215-5217, 1977.
- [61] D. L. Jeanmaire and R. P. Van Duyne, "Surface raman spectroelectrochemistry:: Part I. Heterocyclic, aromatic, and aliphatic amines adsorbed on the anodized silver electrode," *Journal of Electroanalytical Chemistry and Interfacial Electrochemistry*, vol. 84, pp. 1-20, 1977.

- [62] P. L. Stiles, J. A. Dieringer, N. C. Shah and R. P. Van Duyne, "Surface-enhanced Raman spectroscopy," *Annu. Rev. Anal. Chem.*, vol. 1, pp. 601-626, 2008.
- [63] E. C. Le Ru and P. G. Etchegoin, "Single-molecule surface-enhanced Raman spectroscopy," *Annual Review of Physical Chemistry*, vol. 63, pp. 65-87, 2012.
- [64] B. Sharma, R. R. Frontiera, A. I. Henry, E. Ringe and R. P. Van Duyne, "SERS: Materials, applications, and the future," *Materials Today*, vol. 15, pp. 16-25, 2012.
- [65] S. K. Dondapati, T. K. Sau, C. Hrelescu, T. A. Klar, F. D. Stefani and J. Feldmann, "Label-free biosensing based on single gold nanostars as plasmonic transducers," *Acs Nano*, vol. 4, pp. 6318-6322, 2010.
- [66] Y. Levy and J. N. Onuchic, "Water mediation in protein folding and molecular recognition," *Annu. Rev. Biophys. Biomol. Struct.*, vol. 35, pp. 389-415, 2006.
- [67] N. L. Garrett, P. Vukusic, F. Ogrin, E. Sirotkin, C. P. Winlove and J. Moger, "Spectroscopy on the wing: Naturally inspired SERS substrates for biochemical analysis," *Journal of biophotonics*, vol. 2, pp. 157-166, 2009.
- [68] N. R. Jana and T. Pal, "Anisotropic Metal Nanoparticles for Use as Surface-Enhanced Raman Substrates," *Advanced Materials*, vol. 19, pp. 1761-1765, 2007.
- [69] S. M. Stranahan and K. A. Willets, "Super-resolution optical imaging of single-molecule SERS hot spots," *Nano letters*, vol. 10, pp. 3777-3784, 2010.
- [70] J. Petschulat, D. Cialla, N. Janunts, C. Rockstuhl, U. Hübner, R. Möller, H. Schneidewind, R. Mattheis, J. Popp and A. Tünnermann, "Doubly resonant optical nanoantenna arrays for polarization resolved measurements of surface-enhanced Raman scattering," *Optics Express*, vol. 18, no. 5, pp. 4184-4197, 2010.
- [71] A. Grigorescu and C. Hagen, "Resists for sub-20-nm electron beam lithography with a focus on HSQ: state of the art," *Nanotechnology*, vol. 20, p. 292001, 2009.
- [72] H. Duan, D. Winston, J. K. Yang, B. M. Cord, V. R. Manfrinato and K. K. Berggren, "Sub-10-nm half-pitch electron-beam lithography by using poly (methyl methacrylate) as a negative resist," *Journal of Vacuum Science & Technology B: Microelectronics and Nanometer Structures*, vol. 28, pp. C6C58-C6C62, 2010.
- [73] M. G. Stepanova and S. Dew, *Nanofabrication: Techniques and Principles*, Springer, 2012.

- [74] M. Muhammad, S. C. Buswell, S. K. Dew and M. Stepanova, "Nanopatterning of PMMA on insulating surfaces with various anticharging schemes using 30 keV electron beam lithography," *Journal of Vacuum Science & Technology B: Microelectronics and Nanometer Structures*, vol. 29, pp. 06F304-06F304, 2011.
- [75] M. Mohammad, S. Dew, S. Evoy and M. Stepanova, "Fabrication of sub-10nm silicon carbon nitride resonators using a hydrogen silsesquioxane mask patterned by electron beam lithography," *Microelectronic Engineering*, vol. 88, pp. 2338-2341, 2011.
- [76] A. P. Adeyenuwo, *Fabrication of Nanostructures by Low Voltage Electron Beam Lithography*, Edmonton: University of Alberta Libraries, 2012.
- [77] M. A. Mohammad, T. Fito, J. Chen, M. Aktary, M. Stepanova and S. K. Dew, "Interdependence of optimum exposure dose regimes and the kinetics of resist dissolution for electron beam nanolithography of polymethylmethacrylate," *Journal of Vacuum Science Technology B: Microelectronics and Nanometer Structures*, vol. 28, pp. L1-L4, jan 2010.
- [78] M. Mohammad, S. Dew, K. Westra, P. Li, M. Aktary, Y. Lauw, A. Kovalenko and M. Stepanova, "Nanoscale resist morphologies of dense gratings using electron-beam lithography," *Journal of Vacuum Science & Technology B: Microelectronics and Nanometer Structures*, vol. 25, pp. 745--753, 2007.
- [79] C. Wang, *Advanced nanoimprint patterning for functional electronics and biochemical sensing*, Ph.D. dissertation, Dept. Elect. Eng., Princeton University, Princeton, NJ, 2012.
- [80] H. Schiff, "Nanoimprint lithography: An old story in modern times? A review," *Journal of Vacuum Science & Technology B: Microelectronics and Nanometer Structures*, vol. 26, pp. 458--480, 2008.
- [81] O. Glembocki, R. Rendell, D. Alexson, S. Prokes, A. Fu and M. Mastro, "Dielectric-substrate-induced surface-enhanced Raman scattering," *Physical Review B*, vol. 80, p. 085416, 2009.
- [82] P. Voisin, M. Zelsmann, C. Gourgon and J. Boussey, "High-resolution fused silica mold fabrication for UV-nanoimprint," *Microelectronic engineering*, vol. 84, pp. 916--920, 2007.
- [83] Y. Xia and G. M. Whitesides, "Soft lithography," *Annual review of materials science*, vol. 28, pp. 153--184, 1998.

- [84] G.-B. Lee, S.-H. Chen, G.-R. Huang, W.-C. Sung and Y.-H. Lin, "Microfabricated plastic chips by hot embossing methods and their applications for DNA separation and detection," *Sensors and Actuators B: Chemical*, vol. 75, pp. 142--148, 2001.
- [85] B.-H. Jun, M. S. Noh, G. Kim, H. Kang, J.-H. Kim, W.-J. Chung, M.-S. Kim, Y.-K. Kim, M.-H. Cho and D. H. Jeong, "Protein separation and identification using magnetic beads encoded with surface-enhanced Raman spectroscopy," *Analytical biochemistry*, vol. 391, pp. 24--30, 2009.
- [86] C. Burkhardt, K. Fuchsberger, W. Nisch and M. Stelzle, "Micro-and Nanopatterning of Surfaces Employing Self Assembly of Nanoparticles and Its Application in Biotechnology and Biomedical Engineering," 2010.
- [87] H. Elsner, H.-G. Meyer, A. Voigt and G. Grätzner, "Evaluation of ma-N 2400 series DUV photoresist for electron beam exposure," *Microelectronic engineering*, vol. 46, pp. 389--392, 1999.
- [88] C. E. Lee, "Secondary electron generation in electron-beam-irradiated solids: Resolution limits to nanolithography," *Journal of Korean Physical Society*, vol. 55, p. 1720, 2009.
- [89] A. Broers, A. Hoole and J. Ryan, "Electron beam lithography's Resolution limits," *Microelectronic Engineering*, vol. 32, pp. 131--142, 1996.
- [90] P. A. Peterson, Z. Radzimski, S. Schwalm and P. Russell, "Low-voltage electron beam lithography," *Journal of Vacuum Science & Technology B: Microelectronics and Nanometer Structures*, vol. 10, pp. 3088--3093, 1992.
- [91] R. Divan, D. C. Mancini, N. Moldovan, B. Lai, L. Assoufid, Q. Leonard and F. Cerrina, "Progress in the fabrication of high-aspect-ratio zone plates by soft X-ray lithography," 2002.
- [92] W. Hu, G. Bernstein, K. Sarveswaran and M. Lieberman, "Low temperature development of PMMA for sub-10-nm electron beam lithography," 2003.
- [93] B. Cord, J. Lutkenhaus and K. K. Berggren, "Optimal temperature for development of poly (methylmethacrylate)," *Journal of Vacuum Science & Technology B: Microelectronics and Nanometer Structures*, vol. 25, pp. 2013--2016, 2007.

- [94] M. Mohammad, T. Fito, J. Chen, S. Buswell, M. Aktary, M. Stepanova and S. Dew, "Systematic study of the interdependence of exposure and development conditions and kinetic modelling for optimizing low-energy electron beam nanolithography," *Microelectronic Engineering*, vol. 87, pp. 1104--1107, 2010.
- [95] K. Koshelev, M. Ali Mohammad, T. Fito, K. L. Westra, S. K. Dew and M. Stepanova, "Comparison between ZEP and PMMA resists for nanoscale electron beam lithography experimentally and by numerical modeling," *Journal of Vacuum Science & Technology B: Microelectronics and Nanometer Structures*, vol. 29, pp. 06F306--06F306, 2011.
- [96] B. M. Cord, "Achieving sub-10-nm resolution using scanning electron beam lithography," Massachusetts Institute of Technology, 2009.
- [97] M. A. Mohammad, M. Muhammad, S. K. Dew and M. Stepanova, "Fundamentals of Electron Beam Exposure and Development," in *Nanofabrication*, S. K. Dew and M. Stepanova, Eds., Springer, 2012, pp. 11--41.
- [98] K. Satyalakshmi, A. Olkhovets, M. Metzler, C. Harnett, D. M. Tanenbaum and H. Craighead, "Charge induced pattern distortion in low energy electron beam lithography," *Journal of Vacuum Science & Technology B: Microelectronics and Nanometer Structures*, vol. 18, pp. 3122--3125, 2000.
- [99] Y. Todokoro, A. Kajiya and H. Watanabe, "Conductive two-layer resist system for electron-beam lithography," *Journal of Vacuum Science & Technology B: Microelectronics and Nanometer Structures*, vol. 6, pp. 357--360, 1988.
- [100] C. Samantaray and J. Hastings, "The effect of thin metal overlayers on the electron beam exposure of polymethyl methacrylate," *Journal of Vacuum Science & Technology B: Microelectronics and Nanometer Structures*, vol. 26, pp. 2300--2305, 2008.
- [101] R. Peters, T. Fito, L. Gutierrez.-Rivera., S. K. Dew and M. Stepanova, "Study of multilayer systems in electron beam lithography," *Journal of Vacuum Science & Technology B: Microelectronics and Nanometer Structures*, vol. 31, pp. 06F407--06F407, 2013.
- [102] S. Y. Chou, P. R. Krauss and P. J. Renstrom, "Imprint of sub-25 nm vias and trenches in polymers," *Applied physics letters*, vol. 67, p. 3114, 1995.
- [103] I. Yoneda, S. Mikami, T. Ota, T. Koshiba, M. Ito, T. Nakasugi and T. Higashiki, "Study of nanoimprint lithography for applications toward 22nm node CMOS devices," 2008.

- [104] E. A. Costner, M. W. Lin, W. L. Jen and C. G. Willson, "Nanoimprint lithography materials development for semiconductor device fabrication," *Annual Review of Materials Research*, vol. 39, pp. 155--180, 2009.
- [105] Amazon.com, Inc., "Kindle Paperwhite [Previous Generation]," Amazon.com, Inc., 2013. [Online]. Available: <http://www.amazon.ca/Paperwhite-Resolution-Display-Previous-Generation/dp/B007OZO03M>. [Accessed September 2013].
- [106] Institute of Materials Research and Engineering, "Prototype tools for mass producing nanostructures to launch in," 2011.
- [107] L. J. Guo, "Nanoimprint lithography: methods and material requirements," *Advanced Materials*, vol. 19, pp. 495--513, 2007.
- [108] R. S. Kane, S. Takayama, E. Ostuni, D. E. Ingber and G. M. Whitesides, "Patterning proteins and cells using soft lithography," *Biomaterials*, vol. 20, pp. 2363--2376, 1999.
- [109] M. Li, Nanostructure engineering using nanoimprint lithography, Princeton University, 2003.
- [110] A. R. Janzen, "Nanoimprint Lithography," in *Fabrication of Large Area Resonator Arrays using Nanoimprint*, Edmonton, University of Alberta, 2011, pp. 12-28.
- [111] M. Beck, M. Graczyk, I. Maximov, E. L. Sarwe, T. Ling, M. Keil and L. Montelius, "Improving stamps for 10 nm level wafer scale nanoimprint lithography," *Microelectronic Engineering*, vol. 61, pp. 441--448, 2002.
- [112] S. Y. Chou, P. R. Krauss and P. J. Renstrom, "Nanoimprint lithography," *Journal of Vacuum Science & Technology B: Microelectronics and Nanometer Structures*, vol. 14, pp. 4129--4133, 1996.
- [113] Thermo Fisher Scientific Inc., "Nicolet Almega XR Micro and Macro Raman Analysis System," Thermo Fisher Scientific Inc., [Online]. Available: <http://www.thermoscientific.fr/com/cda/product/detail/1,,1000001344538,00.html>. [Accessed 11 09 2013].
- [114] M. Stepanova, T. Fito, Z. Szabó, K. Alti, A. Adeyenuwo, K. Koshelev, M. Aktary and S. Dew, "Simulation of electron beam lithography of nanostructures," *Journal of Vacuum Science & Technology B: Microelectronics and Nanometer Structures*, vol. 28, pp. C6C48--C6C57, 2010.

- [115] S. Siddhanta and C. Narayana, "Surface Enhanced Raman Spectroscopy of Proteins: Implications in Drug Designing," *Nanomaterials and Nanotechnology*, vol. 2, pp. 1--13, 2012.
- [116] H.-J. Werner and P. Knowles, Getting Started with Molpro, University College Cardiff Consultants Limited, 2012.
- [117] CEM888 Course at Michigan State University Website, "Instructions for using GAMESS," [Online]. Available: <http://www2.chemistry.msu.edu/courses/cem888/gamess-instr.html>.
- [118] G. Petersson and M. A. Al-Laham, "A complete basis set model chemistry. II. Open-shell systems and the total energies of the first-row atoms," *The Journal of chemical physics*, vol. 94, p. 6081, 1991.
- [119] G. Petersson, A. Bennett, T. G. Tensfeldt, M. A. Al-Laham, W. A. Shirley and J. Mantzaris, "A complete basis set model chemistry. I. The total energies of closed-shell atoms and hydrides of the first-row elements," *The Journal of chemical physics*, vol. 89, p. 2193, 1988.
- [120] C. D. Sherrill, "Molecular Vibrations," 2001. [Online]. Available: <http://vergil.chemistry.gatech.edu/courses/chem6485/pdf/vibrations.pdf>. [Accessed 25 09 2013].
- [121] Colby College, "Classical Normal Mode Analysis: Harmonic Approximation," Waterville.
- [122] A. Komornicki and J. W. McIver Jr, "An efficient ab initio method for computing infrared and Raman intensities: Application to ethylene," *The Journal of Chemical Physics*, vol. 70, p. 2014, 1979.
- [123] D. Weininger, "SMILES, a chemical language and information system. 1. Introduction to methodology and encoding rules," *Journal of chemical information and computer sciences*, vol. 28, pp. 31--36, 1988.
- [124] M. D. Hanwell, D. E. Curtis, D. C. Lonie, T. Vandermeersch, E. Zurek and G. R. Hutchison, "Avogadro: an advanced semantic chemical editor, visualization, and analysis platform," *Journal of cheminformatics*, vol. 4, pp. 1--17, 2012.
- [125] M. Suenaga, "Facio: new computational chemistry environment for PC GAMESS," *J. Comput. Chem. Jpn*, vol. 4, pp. 25--32, 2005.
- [126] M. Suenaga, "Development of gui for gamess/fmo calculation," *J Comput Chem Jpn*, vol. 7, pp. 33--53, 2008.

- [127] H. Gouda, H. Torigoe, A. Saito, M. Sato, Y. Arata and I. Shimada, "Three-dimensional solution structure of the B domain of staphylococcal protein A: comparisons of the solution and crystal structures," *Biochemistry*, vol. 31, pp. 9665--9672, 1992.
- [128] Y. Kudoh, K. Akami, H. Kusayanagi and Y. Matsuya, Conductive composition precursor, conductive composition, solid electrolytic capacitor, and their manufacturing method, Google Patents, 2005.
- [129] H. Xu, J. Aizpurua, M. Käll and P. Apell, "Electromagnetic contributions to single-molecule sensitivity in surface-enhanced Raman scattering," *Physical Review E*, vol. 62, p. 4318, 2000.
- [130] S. Yasin, D. Hasko and H. Ahmed, "Fabrication of < 5 nm width lines in poly (methylmethacrylate) resist using a water: isopropyl alcohol developer and ultrasonically-assisted development," *Applied Physics Letters*, vol. 78, pp. 2760--2762, 2001.
- [131] A. Kokkinis, E. Valamontes, D. Goustouridis, T. Ganetsos, K. Beltsios and I. Raptis, "Molecular weight and processing effects on the dissolution properties of thin poly (methyl methacrylate) films," *Microelectronic Engineering*, vol. 85, pp. 93--99, 2008.
- [132] Siegwark Druckfarben AG & Co., "Evaporation Rates of Solvents - Technical Sheet," Siegwark, 2008.
- [133] C. A. Schneider, W. S. Rasband and K. W. Eliceiri, "NIH Image to ImageJ: 25 years of image analysis," *Nat Methods*, vol. 9, pp. 671--675, 2012.
- [134] R. Dylewicz, S. Lis, R. De La Rue and F. Rahman, "Charge dissipation layer based on conductive polymer for electron-beam patterning of bulk zinc oxide," *Electronics letters*, vol. 46, pp. 1025--1027, 2010.
- [135] I. Antonets, L. Kotov, S. Nekipelov and E. Karpushov, "Conducting and reflecting properties of thin metal films," *Technical physics*, vol. 49, pp. 1496--1500, 2004.
- [136] M. Ohring, Materials science of thin films, Academic press, 2001.
- [137] S. Holl, R. Varasala, H. Jawanda, C. Colinge, K. Hobart, F. J. Kub and S. Song, "Fabrication Techniques for Thin-Film Silicon Layer Transfer," *ECS Transactions*, vol. 3, pp. 67--73, 2006.

- [138] A. Kroetch, S. C. Buswell, S. Evoy, C. Durak, J. R. Heflin, V. Kochergin and R. Duncan, "Fabrication of nonlinear optical devices in ionically self-assembled monolayers," *Journal of Micro/Nanolithography, MEMS, and MOEMS*, vol. 8, pp. 013011--013011, 2009.
- [139] J.-K. Chen, F.-H. Ko, K.-F. Hsieh, C.-T. Chou and F.-C. Chang, "Effect of fluoroalkyl substituents on the reactions of alkylchlorosilanes with mold surfaces for nanoimprint lithography," *Journal of Vacuum Science & Technology B: Microelectronics and Nanometer Structures*, vol. 22, pp. 3233--3241, 2004.
- [140] MicroChem Corporation, "PMMA: FAQs," MicroChem Corporation, [Online]. Available: http://microchem.com/pmma_faq.htm. [Accessed September 2013].
- [141] Institute, Ioffe Physico-Technical, "Si - Silicon Thermal Properties," [Online]. Available: <http://www.ioffe.ru/SVA/NSM/Semicond/Si/thermal.html>. [Accessed 15 02 2013].
- [142] C. Tsou, Y. Huang, H.-C. Li and T.-H. Lai, "On the Determination of Thermal Expansion Coefficient of Thermal Oxide," *Sens. Mater*, vol. 17, pp. 441--451, 2005.
- [143] A. S. Grove and A. Grove, *Physics and technology of semiconductor devices*, vol. 143, Wiley New York, 1967.
- [144] Accuratus, "Fused Silica, SiO₂ Material Properties," 2002. [Online]. Available: <http://accuratus.com/fused.html>. [Accessed 15 02 2013].
- [145] L. Björck, "Protein L. A novel bacterial cell wall protein with affinity for Ig L chains.," *The Journal of Immunology*, vol. 140, pp. 1194--1197, 1988.
- [146] U. Sjöbring, L. Björck and W. Kastern, "Streptococcal protein G. Gene structure and protein binding properties.," *Journal of biological chemistry*, vol. 266, pp. 399--405, 1991.
- [147] J. Turková, "Oriented immobilization of biologically active proteins as a tool for revealing protein interactions and function," *Journal of Chromatography B: Biomedical Sciences and Applications*, vol. 722, pp. 11--31, 1999.
- [148] M. Eliasson, R. Andersson, A. Olsson, H. Wigzell and M. Uhlén, "Differential IgG-binding characteristics of staphylococcal protein A, streptococcal protein G, and a chimeric protein AG.," *The Journal of Immunology*, vol. 142, pp. 575-581, 1989.

- [149] Z. A. Combs, S. Chang, T. Clark, S. Singamaneni, K. D. Anderson and V. V. Tsukruk, "Label-Free Raman Mapping of Surface Distribution of Protein A and IgG Biomolecules," *Langmuir*, 2011.
- [150] A. Blawas and W. Reichert, "Protein patterning," *Biomaterials*, vol. 19, pp. 595--609, 1998.
- [151] J. Carlsson, H. Drevin and R. Axen, "Protein thiolation and reversible protein-protein conjugation. N-Succinimidyl 3-(2-pyridyldithio) propionate, a new heterobifunctional reagent.," *Biochem. J.*, vol. 173, pp. 723--737, 1978.
- [152] Y. Kang, M. Si, R. Liu and S. Qiao, "Surface-enhanced Raman scattering (SERS) spectra of hemoglobin on nano silver film prepared by electrolysis method," *Journal of Raman Spectroscopy*, vol. 41, pp. 614--617, 2010.
- [153] M. R. Mahoney and R. P. Cooney, "Laser damage on silver electrode surfaces exhibiting intense Raman scattering from cyanide," *The Journal of Physical Chemistry*, vol. 87, pp. 4589--4591, 1983.
- [154] D. Kuila, J. R. Schoonover, R. B. Dyer, C. J. Batie, D. P. Ballou, J. A. Fee and W. H. Woodruff, "Resonance Raman studies of Rieske-type proteins," *Biochimica et Biophysica Acta (BBA)-Bioenergetics*, vol. 1140, pp. 175--183, 1992.
- [155] M. Kahraman, İ. Sur and M. Çulha, "Label-free detection of proteins from self-assembled protein-silver nanoparticle structures using surface-enhanced raman scattering," *Analytical chemistry*, vol. 82, pp. 7596--7602, 2010.
- [156] S. Stewart and P. Fredericks, "Surface-enhanced Raman spectroscopy of peptides and proteins adsorbed on an electrochemically prepared silver surface," *Spectrochimica Acta Part A: Molecular and Biomolecular Spectroscopy*, vol. 55, pp. 1615-1640, 1999.
- [157] J.-M. a. S. R. E. Fellous, "The Roles of Dopamine," in *The handbook of brain theory and neural networks, 5 Edition*, M. A. Arbib, Ed., Madison, Wisconsin: MIT Press, 2002, pp. 361-365.
- [158] J. Lotharius and P. Brundin, "Pathogenesis of Parkinsons disease: dopamine, vesicles and α -synuclein," *Nature Reviews Neuroscience*, vol. 3, pp. 932-942, 2002.

- [159] E. H. Cook Jr, M. A. Stein, M. D. Krasowski, N. J. Cox, D. M. Olkon, J. E. Kieffer and B. L. Leventhal, "Association of attention-deficit disorder and the dopamine transporter gene.," *American journal of human genetics*, vol. 56, p. 993, 1995.
- [160] K. L. Davis, R. S. Kahn, G. Ko and M. Davidson, "Dopamine in schizophrenia: a review and reconceptualization.," *The American journal of psychiatry*, 1991.
- [161] S. K. Jääskeläinen, J. O. Rinne, H. Forssell, O. Tenovuo, V. Kaasinen, P. Sonninen and J. Bergman, "Role of the dopaminergic system in chronic pain--a fluorodopa-PET study," *Pain*, vol. 90, pp. 257--260, 2001.
- [162] M. Paterlini, S. S. Zakharenko, W.-S. Lai, J. Qin, H. Zhang, J. Mukai, K. G. Westphal, B. Olivier, D. Sulzer and P. Pavlidis, "Transcriptional and behavioral interaction between 22q11. 2 orthologs modulates schizophrenia-related phenotypes in mice," *Nature neuroscience*, vol. 8, pp. 1586--1594, 2005.
- [163] R. Walsh and M. C. DeRosa, "Retention of function in the DNA homolog of the RNA dopamine aptamer," *Biochemical and biophysical research communications*, vol. 388, no. 4, pp. 732--735, 2009.
- [164] C. Mannironi, A. Di Nardo, P. Fruscoloni and G. Tocchini-Valentini, "In vitro selection of dopamine RNA ligands," *Biochemistry*, vol. 36, pp. 9726--9734, 1997.
- [165] C. K. OSullivan, "Aptasensors--the future of biosensing?," *Analytical and bioanalytical chemistry*, vol. 372, pp. 44--48, 2002.
- [166] J. R. Lakowicz, Y. Shen, S. DAuria, J. Malicka, J. Fang, Z. Gryczynski and I. Gryczynski, "Radiative decay engineering: 2. Effects of silver island films on fluorescence intensity, lifetimes, and resonance energy transfer," *Analytical biochemistry*, vol. 301, pp. 261--277, 2002.
- [167] J. Akitomi, S. Kato, Y. Yoshida, K. Horii, M. Furuichi and I. Waga, "ValFold: Program for the aptamer truncation process," *Bioinformation*, vol. 7, p. 38, 2011.
- [168] K. Han and Y. Byun, "PseudoViewer2: visualization of RNA pseudoknots of any type," *Nucleic Acids Research*, vol. 31, pp. 3432--3440, 2003.
- [169] S.-K. Park, N.-S. Lee and S.-H. Lee, "Vibrational Analysis of Dopamine Neutral Base based on Density Functional Force Field," *Bulletin-Korean Chemical Society*, vol. 21, pp. 959--968, 2000.